PONTIFÍCIA UNIVERSIDADE CATÓLICA
DO RIO DE JANEIRO

Luiz Pereira De Aguiar Neto

Nonlinear Dynamic Behavior of Oil-Well Drill Strings

DISSERTAÇÃO DE MESTRADO

Dissertation presented to the Programa de Pós-Graduação em Engenharia Mecânica of PUC-Rio in partial fulfillment of the requirements for the degree of Mestre em Engenharia Mecânica.

Advisor: Prof. Ivan Fabio Mota de Menezes
Co-Advisor: Dr. Ludimar Lima de Aguiar

Rio de Janeiro
October 2021

Pontifícia Universidade Católica
do Rio de Janeiro

Luiz Pereira De Aguiar Neto

Nonlinear Dynamic Behavior of Oil-Well Drill Strings

Dissertation presented to the Programa de Pós-Graduação em Engenharia Mecânica of PUC-Rio in partial fulfillment of the requirements for the degree of Mestre em Engenharia Mecânica. Approved by the Examination Committee.

Prof. Ivan Fabio Mota de Menezes
Advisor
Departamento de Engenharia Mecânica – PUC-Rio

Dr. Ludimar Lima de Aguiar
Co-Advisor
Centro de Pesquisa e Desenvolvimento – Petrobras

Prof. Anderson Pereira
Departamento de Engenharia Mecânica – PUC-Rio

Prof. João Carlos Ribeiro Plácido
Departamento de Engenharia Mecânica – PUC-Rio

Rio de Janeiro, October 07, 2021

Luiz Pereira de Aguiar Neto

Graduated in Civil Engineering from Federal University of Sergipe in 2018.

Bibliographic data

Aguiar Neto, Luiz Pereira de

Nonlinear dynamic behavior of oil-well drill strings / Luiz Pereira de Aguiar Neto ; advisor: Ivan Fabio Mota de Menezes ; co-advisor: Ludimar Lima de Aguiar. – 2021.
100 f. : il. color. ; 30 cm

Dissertação (mestrado)–Pontifícia Universidade Católica do Rio de Janeiro, Departamento de Engenharia Mecânica, 2021.

Inclui bibliografia

1. Engenharia Mecânica - Teses. 2. Coluna de perfuração. 3. Elementos finitos não linear. 4. Análise dinâmica. 5. Flambagem. 6. Solução numérica. I. Menezes, Ivan Fabio Mota de. II. Aguiar, Ludimar Lima de. III. Pontifícia Universidade Católica do Rio de Janeiro. Departamento de Engenharia Mecânica. IV. Título.

CDD: 621

To my family and friends, for the
support and trust.

Acknowledgements

To Professor Ivan Menezes and DSc. Ludimar Aguiar for encouraging, supporting, and advising me. You are the ones that became this work possible.

To my professors from UFS for building all the basis that led me to the masters.

To my professors from PUC-Rio for all the learnings, support and advices.

To all the friends that I met, and found again in Rio, that helped to become the journey easier.

To all the friends from Aracaju, that I am sure that will go along with me for all life long. You are really specials! Thank you all!

To my coworkers and friends from SEMOP - Barra dos Coqueiros/SE. You are part of my life.

To my father and siblings.

To my grandma, uncles, aunts, and cousins.

To my grandpa (*in memoriam*).

Special thanks to Ludimar Aguiar and his family, now as my uncle and family too. I am really grateful for all the support and patience.

I deeply thank to my mother, stepfather, sister, and my beloved girlfriend. I do not have words to express how much they were important in this process.

This study was financed in part by the Coordenação de Aperfeiçoamento de Pessoal de Nível Superior - Brasil (CAPES) - Finance Code 001.

Abstract

Neto, Luiz Pereira de Aguiar; Menezes, Ivan Fabio Mota de (Advisor); Aguiar, Ludimar Lima de (Co-Advisor). **Nonlinear Dynamic Behavior of Oil-Well Drill Strings**. Rio de Janeiro, 2021. 100p. Dissertação de Mestrado - Departamento de Engenharia Mecânica, Pontifícia Universidade Católica do Rio de Janeiro.

This work studies the nonlinear dynamic behavior of oil well drillstring, which is a long slender flexible structure responsible for the drilling. Its elements and functions are presented, and numerical analyses are performed later. The work develops a computational code using the software MATLAB® for the numerical simulation of the column's dynamic behavior using the finite element method. The corotational formulation is used for the implementation of geometric nonlinearity. The structure's discretization uses a beam element with six degrees of freedom per node and employs the Euler-Bernoulli's beam formulation. The Newton-Raphson method is responsible for solving the nonlinear system of equations. In addition, the solution procedure uses the Newmark's method for the time integration of the problem's movement equations. A linear setup spring model is proposed to represent the contact between the borehole wall and the column. The proposed methodology and computational code capabilities are evaluated by comparing some results to analytical or numerical results of examples available in the literature. These results give reliability to analyze drillstring problems, which present the displacements and forces time series of the whole column and the buckling modes generated. The results show that the column is very sensitive to any boundary condition changing, which corroborates the complexity of the problem. Hence, the work proposes a reasonable basis for further developments, allowing the entire coupled drillstring analysis.

Keywords

Drillstring; Nonlinear Finite Elements; Dynamic Analysis; Buckling; Numerical Solution

Resumo

Neto, Luiz Pereira de Aguiar; Menezes, Ivan Fabio Mota de (Orientador); Aguiar, Ludimar Lima de (Coorientador). **Comportamento Dinâmico Não Linear de Colunas de Perfuração de Poços de Petróleo**. Rio de Janeiro, 2021. 100p. Dissertação de Mestrado - Departamento de Engenharia Mecânica, Pontifícia Universidade Católica do Rio de Janeiro.

Esta dissertação estuda o comportamento dinâmico não linear de colunas de perfuração de poços de petróleo. A coluna de perfuração é uma estrutura longa, flexível e esbelta, responsável pela perfuração propriamente dita. Seus elementos e funções são apresentados e uma análise numérica é realizada posteriormente. Foi desenvolvido um programa utilizando o software MATLAB® para simulação numérica do comportamento dinâmico das colunas pelo método dos elementos finitos que utiliza a formulação corotacional para implementação da não linearidade geométrica. A discretização da estrutura utiliza um elemento de viga com seis graus de liberdade por nó aplicando a formulação de viga de Euler-Bernoulli. Para solução do sistema de equações não lineares resultante utiliza-se o método de Newton-Raphson. Além disso, o método de Newmark é utilizado para integração no tempo das equações de movimento do problema. Um modelo com molas lineares é proposto para representar o contato entre a parede do poço e a coluna. A metodologia proposta e as funcionalidades do programa desenvolvido são avaliadas e seus resultados são comparados com algumas soluções analíticas ou numéricas de exemplos disponíveis na literatura. Esses resultados conferem confiabilidade na análise de problemas de coluna de perfuração, que apresentam as séries temporais de deslocamentos e esforços em toda a coluna e os modos de flambagem gerados. Os resultados obtidos demonstram que a coluna é muito sensível a qualquer mudança de condição de contorno, o que corrobora com a complexidade do problema. Assim, o trabalho fornece uma base razoável para desenvolvimentos posteriores, que permitam a análise de toda a coluna de perfuração acoplada.

Palavras-chave

Coluna de Perfuração; Elementos Finitos Não Linear; Análise Dinâmica; Flambagem; Solução Numérica.

Contents

List of Figures

List of Tables

Nomenclature

i	node index; vector index; iteration
j, r, s	tensor index;
t	time;
m	index that indicates elemental matrices or vectors;
Δt	time increment;
X, Y, Z	local element reference system;
x, y, z	nodal reference system;
$\boldsymbol{\tau}$	Cauchy stress tensor;
$\boldsymbol{e}$	strain tensor;
$\boldsymbol{u}$	displacement vector;
$\dot{\boldsymbol{u}}, \ddot{\boldsymbol{u}}$	velocity and acceleration vector, respectively;
V	volume;
S_f	surface on which external tractions are applied;
δe_{ij}	strain tensor component corresponding to virtual displacements;
$\delta \eta_{ij}$	non-linear incremental strains component
τ_{ij}	Cartesian component of Cauchy stress tensor;
δu_i	component of virtual displacement vector;
f_i^B	component of externally applied forces per unit volume (body forces);
f_i^S	component of externally applied surface tractions per unit surface area (surface forces);
C_{ijrs}	material constitutive tensor component;
ρ, κ	material density and damping parameter, respectively;
$\mathbf{R}$	Rodrigues orthogonal rotation matrix;
$\boldsymbol{H}$	Interpolation matrix;
$\boldsymbol{B_L}$	linear strain-displacement matrix (compatibility matrix);
$\boldsymbol{B_{NL}}$	non-linear strain-displacement matrix (geometric compatibility matrix);
$\boldsymbol{C}$	stress-strain material property matrix;
$\boldsymbol{M}$	mass matrix;
$\boldsymbol{K_L}$	linear stiffness matrix;

It can scarcely be denied that the supreme goal of all theory is to make the irreducible basic elements as simple and as few as possible without having to surrender the adequate representation of a single datum of experience.

Albert Einstein, *"On the Method of Theoretical Physics"*, Oxford, 10 June 1933.

1.
Introduction

It is outstanding that the petroleum industry leads the energy sector, pushing contemporaneous civilization [9]. Regardless of the business type, it still depends, somehow, on that energy. It is necessary for any commercial endeavor, industrial enterprise, construction industry, and even to produce another type of energy [4]. Hossain [9] states that some scholars consider petroleum hydrocarbons to be the lifeblood of modern civilization.

The energy's origin occurs mainly in difficult access areas, confined deep below ground, under the Earth's surface, or even under ultra-deep waters. Because its significance, a well is drilled to connect the energy origin to the surface. Due to the huge pressures generated by the adjacent rocks, that well must have the strength to withstand that pressure and prevent any condition that may jeopardize the environment. So, it is equipped with modern equipment to perform its function, such as sophisticated hydraulic systems used for closing blowout preventers (BOP), and devices that show and record, simultaneously, most of the main parameters related to the drilling operation [4].

1.1.
Oil Well Drilling

Contemporary well drilling requires various specialists and, normally, many companies. The type of well to be drilled, its objective, location, depth, and complexity determine the expertise and number of professionals included in the planning and execution of the drilling operation [4].

The main wells are exploration and development wells. The first one has the function of discovering a new petroleum reservoir, and it divides into wildcat, appraisal, and extension. Wildcat wells are the earliest drilled in a determined area. Appraisal wells may start when wildcat wells show that the reservoir can be productive, to achieve more knowledge about the reservoir and its extension. The extension wells are drilled on the edge of the existing field that may extend the field's known area [4].

Development wells are drilled to produce gas and oil or inject fluids in the reservoir.

The oil well configuration is mostly vertical, but directional or horizontal configurations are feasible [10]. Directional drilling is the technic of deviating a well trajectory on purpose to achieve objectives that are not vertically below the rig location on the surface [1]. Figure 1 shows an example of a horizontal well.

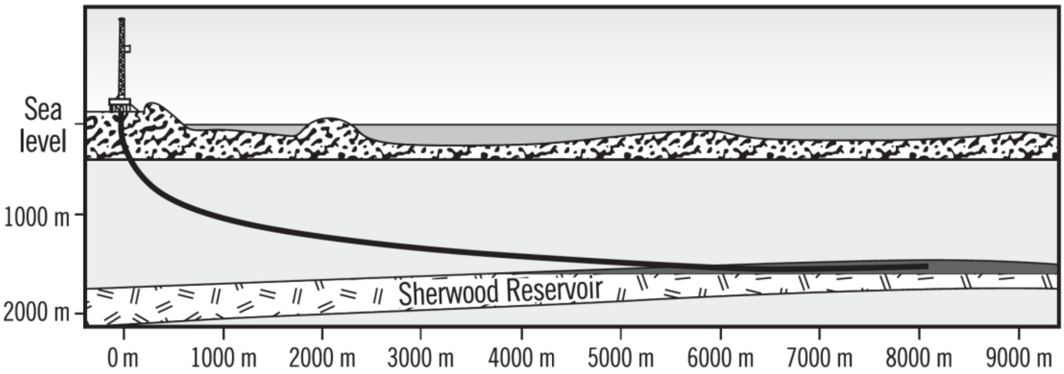

Figure 1 - Development horizontal well in Wytch Farm, England [12].

1.2.
Rotary Drilling

The rotary system consists of a combined mechanical and hydraulic system. The mechanical part is accountable for energy transport, which is the transmitted rotation and weight to a rock-cutting tool, named as bit. This system’s most important components are a swivel, kelly, a rotary drive, a drillstring, the bit, and a rig to support the system [2, 4].

The rotary swivel is a connection point between the rotary system and the circulating system. Besides, it provides a fluid seal that must absorb rotational wear while holding pressure. The top of the swivel has a bail to connect to the elevator hook, and the gooseneck has a downward-pointing connection for the mud hose, part of the hydraulic system [4]. The mud hose is a steel-reinforced, high-pressure, flexible hose that connects the standpipe (a pipe attached to the derrick’s side, responsible for conducting the drilling fluid from the mud pumps to the mud hose) to the kelly.

The kelly is a square or hexagonal pipe placed right below the swivel responsible for transmitting torque to the drillstring. Kelly bushings, which fit inside the master bushing of the rotary table, are the elements that transmit torque to the kelly [13]. Figure 2 shows a simplified model of the rotary system.

Formerly, the main driver in the rotary system was the rotary table. The equipment transmits torque to the drillstring and allows the kelly to go up and down freely inside it [1]. Modern rigs use a top drive to replace the rotary table, kelly, and kelly bushings. The hook suspends the top drive to travel up and down the derrick, allowing the drilling to be done with stands of pipes instead of single joints, saving considerable time. Electric or hydraulic motors produce the drilling rotation [4].

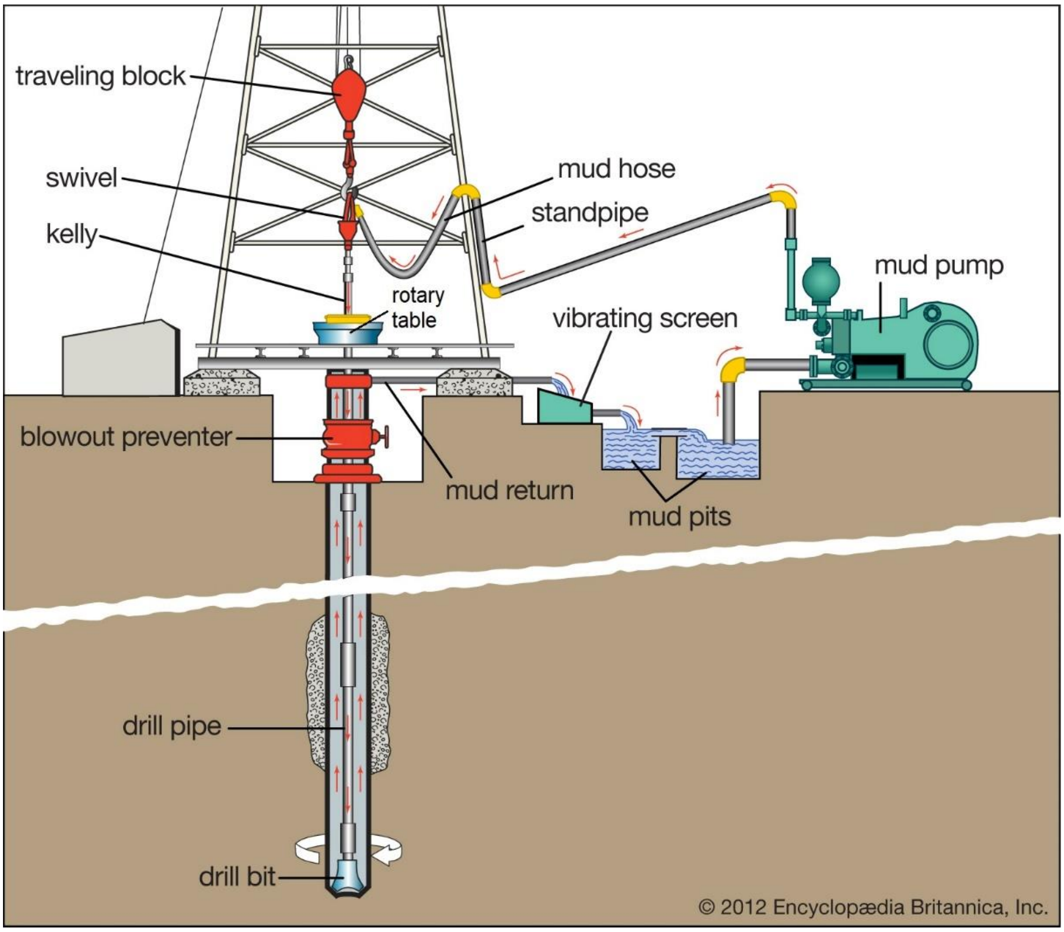

Figure 2 - Simplified model of the rotary drilling system [10].

The drillstring is the object of study of this work, and a further discussion about it and the drill bit develops ahead.

The hydraulic part consists of a drilling fluid, mud pumps, mud pits, mud-mixing, and contaminant-removal equipment [2, 13]. The drilling fluid is, commonly, a suspension of solids, viscosifiers, and weighting materials in water, oil or synthetic fluid. Usually called drilling mud. The drilling mud travels from the steel tanks to the mud pumps. Then, it goes to the mud hose, through the standpipe, to the drillstring. From the entire drillstring to the bit and employing the bit's nozzles, it goes up through the annulus between the drillstring and the borehole wall, returning to the surface. At the surface, it passes through the contaminant-removal equipment (vibrating screens, for example) and returns to the suction tanks [13, 14]. See Figure 2.

The main function of the drilling mud is to carry the cuttings from the hole bottom to the surface, besides cooling and lubricating the drill bit.

1.3.
Drilling Monitoring System

Achieving safety and efficiency requires continuous monitoring of the well to figure out and solve drilling problems as soon as possible [13]. According to Jansen (1993) [2], the main operating parameters to control the drilling process are the hook load, the rotary speed at the surface, and the flow rate.

The hook load is the axial reaction force at the top end of the drillstring, and, many times, it is almost equal to the weight of the drillstring. Lowering or raising the hook cause fluctuations in the hook load that give a gross measure of the *weight on bit* (WOB), the downward force applied on the drill bit [2].

The rotary speed at the surface is the angular velocity of the top end of the drillstring. However, this parameter may be very different from the immediate rotary speed at the bit because of the torsional flexibility of the drillstring. Nevertheless, the average values of the rotary speed at the top and bottom are equal [2].

The flow rate is the volume of mud pumped down the drillstring during a period of time. Usually, the flow rate through the pumps at the surface is the same as the flow rate through the nozzles at the bit [13]. The control of the drilling fluid hydraulics is important to achieve adequate hole cleaning below the bit. That significance is due to the dependency of the rate of penetration (ROP) of the hole cleaning below the bit. Furthermore, accumulating cuttings below the bit may damage the bit owing to overheating, besides disturbing the detection of changes in the formation properties [14].

The rate of penetration mentioned above is the main parameter to assess the effectiveness of the drilling process. It is given by observing the downward speed of the drillstring. The ROP depends on the type of rock to be drilled, the depth of the borehole, the condition of the bit, and the composition of the drilling mud [2].

Some other parameters observed by the driller are the motor current of the rotary drive, and the standpipe pressure.

In the case of a DC electric drive, the current through the motor is a measure of the torque at the top of the drill string. Howbeit, due to friction losses, mainly in directional wells, the torque on bit (TOB) may be an order of magnitude lower than the torque on the top [2].

Measuring the standpipe pressure gives an accurate measure of the total pressure drop in the drillstring and the annulus. From the safety perspective, pressure is the main factor to control during drilling. The earth layers in contact with the borehole may have great pressures difference. Thus, the density of the drilling fluid is deliberately adjusted so that the borehole pressure is slightly higher than the fluid pressure in the rock. The purpose is to avoid the fluid loss or an influx of formation fluid. To separate several pressurized earth layers, the drilling process is stopped to cover the borehole wall with a high-strength steel tube (casing) lowered into the borehole and then fixed with cement. This procedure requires a stepwise reduction in borehole size but protects it against mechanical damage, erosion, and collapse of the borehole [2]. Figure 3 demonstrates a typical casing program.

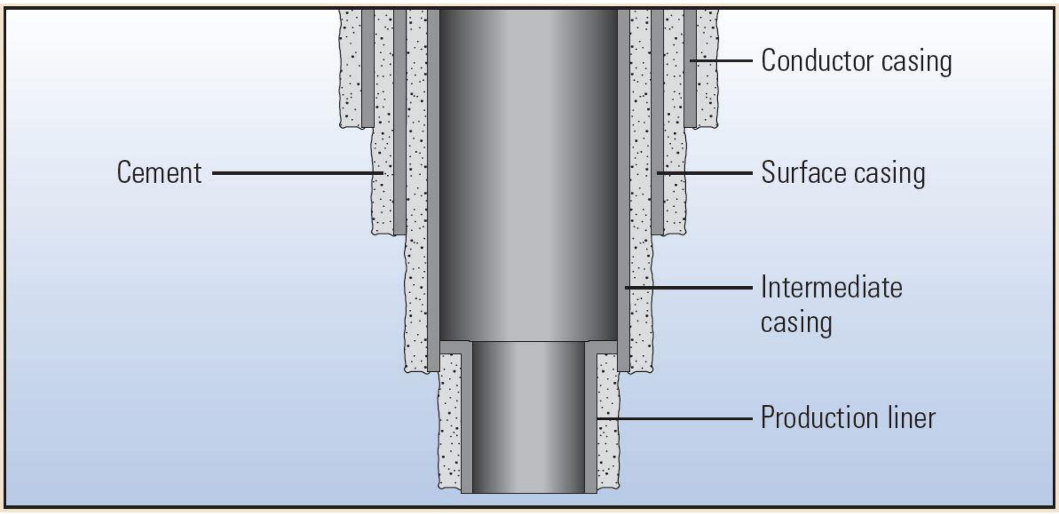

Figure 3 - Typical casing program [15].

1.4.
Objective and scope of the dissertation

The primary purpose of this dissertation is to develop a finite element program for studying the dynamic non-linear behavior of oil wells' drillstrings. The drillstring is the leading drilling tool since it's the one that performs the drilling itself. The drillstring is a long slender column that may have thousands of meters in length, and a standard comparison shows that the ratio cross-section/length is less than the human hair. Furthermore, that column works confined by the formation drilled, generating a complex drillstring/formation contact (laterally and vertically). These two facts make the analysis challenging and studying it allows the proper design and operation of the drilling elements.

The present work aims to propose an initial program for nonlinear dynamic drillstring analysis, considering linear contact between the beam elements and the wellbore wall, to further developments and research on drillstring behavior.

The finite element implementation uses the co-rotational formulation, considering Euler-Bernoulli beam theory with six degrees of freedom per node. The problem is solved using an incremental-iterative strategy, which computes the displacements and forces time series. The research analyzes these displacements and forces generated by applying a determined weight on bit and a prescribed rotation at the top of the column. In addition, the dissertation also provides some buckling analyses using examples from the literature.

The dissertation's first chapter presents an overview of oil well drilling, showing the types of well, some mechanical and hydraulic components of the rotary drilling system, and the main operating parameters to control the drilling process.

Chapter 2 presents a detailed information about the drillstring, which is the dissertation's object of study. The chapter depicts the drillstring's components types and the parameters necessary to design the column.

The main subject of Chapter 3 is the drillstring vibrations, explaining their occurrence and formations that they usually develop. In addition, the chapter also presents the influence of the vibrations in the drilling process.

Chapter 4 furnishes a detailing numerical method, showing the literature review, the fundamental hypothesis assumed in this work, and describes the steps to perform the problem's analysis. Besides, the wellbore-drillstring contact formulation is also presented.

Chapter 5 deals with the drillstring buckling, explaining its meaning and occurrence, presenting the literature review about the subject, and a method to trigger the buckling in numerical analyses.

Chapter 6 discusses the numerical results, presenting and comparing some literature’s standard examples for geometric non-linear analysis and the outcomes of drillstring performance.

Chapter 7 shows the dissertation's overview, summarizing its contribution and suggests further researches on unresolved problems about drillstring dynamic non-linear analysis.

The last chapter is the list of the references used in this work.

2.
Drillstring

The rotary drilling requires a huge amount of energy at the bit to drill several different earth layers. Sometimes called drillstem, the drillstring is directly responsible for providing that energy as torque and weight at the drill bit. Moreover, the drillstring conducts the drilling fluid to the bottom hole, so the cuttings from the drilling process are lifted through the annulus to the surface, keeping the well clean [1]. In addition, the drillstring controls the borehole direction [4], depending on its diameters, stabilizers positioning, rotation of the column, fluid flux, etc. [17].

The main components of the drillstring are *drill pipes* (DP), *heavy weight drill pipes* (HWDP), *drill collars* (DC), and *stabilizers*. Some authors also include as component the kelly and drill bit [4, 9, 16]. The part right above the bit, composed mainly of drill collars and stabilizers, is called *bottom hole assembly* (BHA). It has between 200 m and 400 m, and it is accountable for supplying weight on the bit and controlling the wellbore trajectory. It is possible that the BHA also has other tools as Rotary Steerable System (RSS), downhole motor, Measurement While Drilling (MWD), and Logging While Drilling (LWD).

Furthermore, some other types of equipment as drilling jars, reamers, shock absorbers, and junk baskets, can be added to the drillstring [4].

2.1.
Drill Pipes

The drill pipes (DP) compose a major part of the drillstring. Commonly, DP is made out of steel (SDP), but depending on the downhole temperatures, wellbore path configuration, presence of H_2S and CO_2, drag and torque issues, etc., titanium (TDP) or aluminum drill pipe (ADP) may be used. The joints are fastened together in drillstring through tool joints [4, 13]. Their attachments commonly used were hot-rolled, pierced seamless tubing, occasionally with the end threaded, but nowadays, threaded connections have been replaced by butt welds. Both DP ends are upset to reinforce the ends. The drill pipes can be classified by size, wall thickness, steel grade, and length ranges. Length ranges vary from 16 ft to 45 ft, but in regular rotary-drilling operations, the most used range is usually 27-30 ft [4].

The drill pipes may also be employed for completion, well stimulation, drillstem testing, and fishing operations [4]. Figure 4 shows a type of DP.

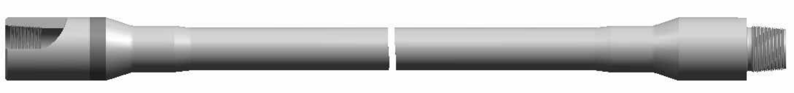

Figure 4 - Drill Pipe [55].

2.2.
Heavy-Weight Drill Pipes

The transition from drill pipes to drill collars is a common location of drillstring failures. In some conditions, high bending and stresses can be yielded in dog legs located transitions or under a buckled section. The Heavy-Weight Drill Pipes (HWDP) do this transition and relieve the problem [3]. HWDP has thicker walls than DP, usually has the same length, with hard-facing metal-coated joints, as well as the central body. Figure 5 illustrates several types of HWDP [1].

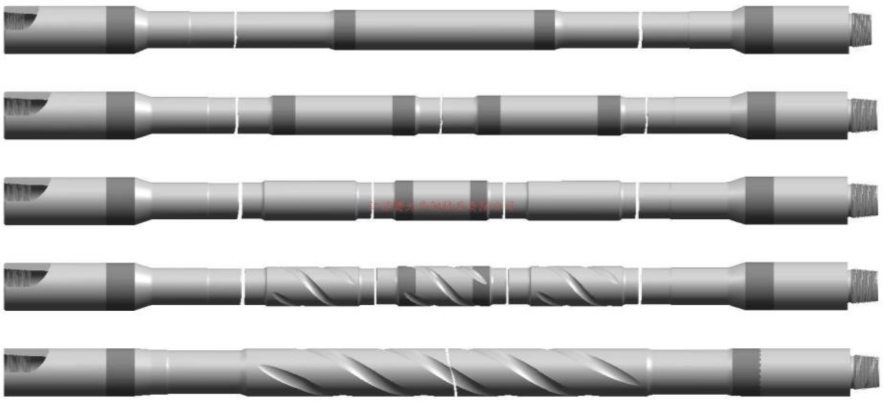

Figure 5 - Types of HWDP [55].

2.3.
Drill Collars

The drill collars are thick-walled heavy steel tubes that set a major part of the BHA. The main purposes of the DC are to provide WOB and stiffness to the drillstring, allowing better control of the well trajectory [1]. The geometrical and mechanical properties of the BHA must be carefully designed because they affect hole problems (key seats, doglegs, differential pressure sticking), bit performance (drilling rate and bit wear), drill pipe service life, and drillstring vibrations [4].

As shown in Figure 6, drill collars are manufactured in many sizes and shapes. Ordinary DC has a round section, but spiral and square cross-sections are also used in the drilling industry. The square cross-sectional outside profile is used to achieve greater stiffness of a BHA. Meanwhile, the spiral type is used to avoid differential pressure sticking problems. These DC have spiral grooves on the outside surface that minimize the contact between the drill collars and the borehole wall, decreasing the sticking force [4]. The same occurs with the HWDP.

Many factors influence the DC unit weight and shape choice, such as formation dip angle and heterogeneity, hydraulic program, maximum acceptable dogleg, required WOB, among others [4].

Figure 6 - Drill Collars (DC) types [55].

2.4.
Stabilizers

Stabilizers furnishes stiffness to the drillstring, and because their diameter is equal to the bit, they assist in keeping the wellbore diameter. In directional drilling, the stabilizers have the function of displacing the foothold of the DC at the borehole wall, supplying a better control of well trajectory [1].

In addition, stabilizers with a diameter near the hole size decrease the severity of problems as bit wear and damage, poor borehole quality, directional drilling problems, and increased frequency of drillstring-component failures. These problems may occur if the DC above the bit is not centered in the borehole, affecting adversely the bit rotation and cutting action [4].

The stabilizers were designed with open blades (See Figure 7) so the fluid can move vertically up the annular space unobstructed. Formerly, the tool was placed near the drill bit, but posterior scientific approaches could determine stabilizers positioning that keeps the bit to drill in a preferred direction [3].

Figure 7 - Type of stabilizer [4].

For example, if a drill collar is supported at each end, the middle part of the DC will sag in an inclined position due to the weight, creating a side force at the bit (Figure 8). This effect, known as the *fulcrum effect*, is used to build angle [12].

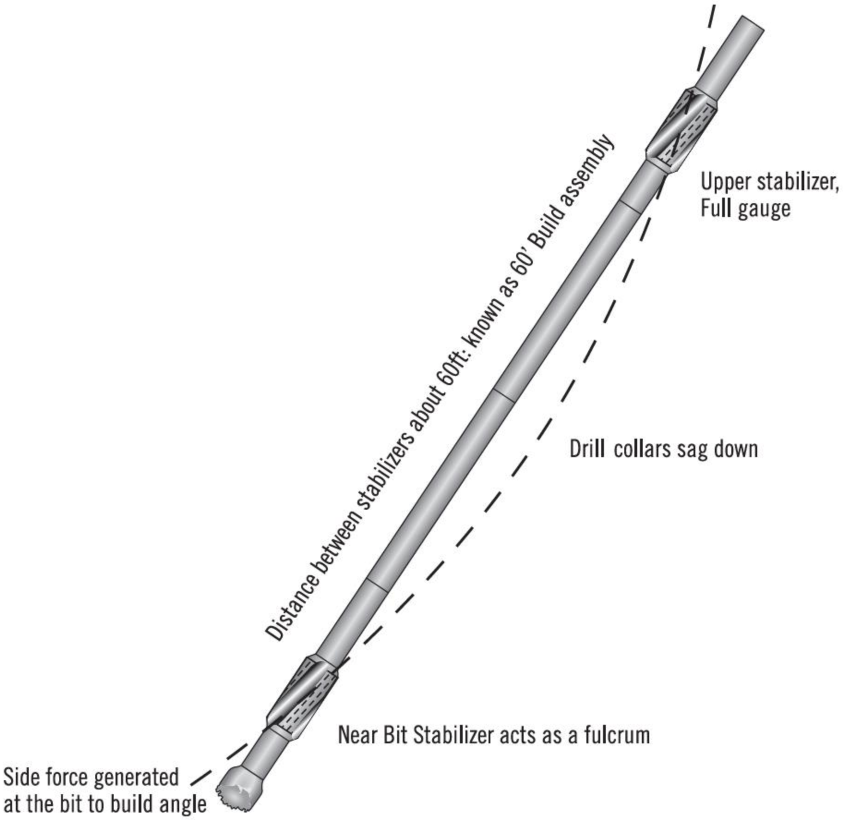

Figure 8 - Fulcrum effect drillstring assembly [12].

Nonetheless, the stabilizers may be positioned so the column can drop or maintain the angle, as illustrated in Figure 9 and Figure 10. The assemblies are known as *pendulum assembly* and *tangent* (or *packed*) assembly, respectively.

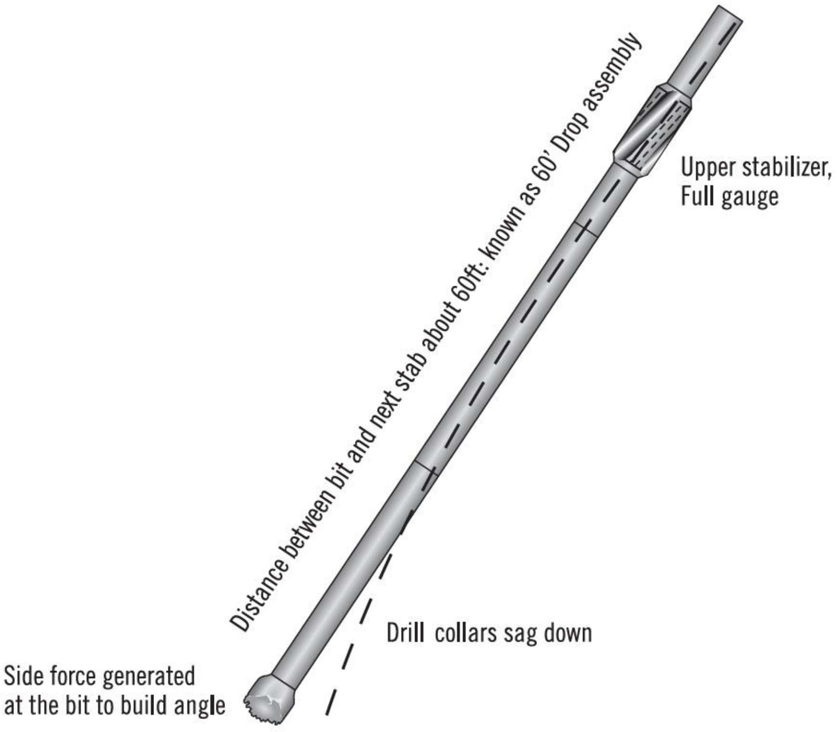

Figure 9 - Pendulum assembly [12].

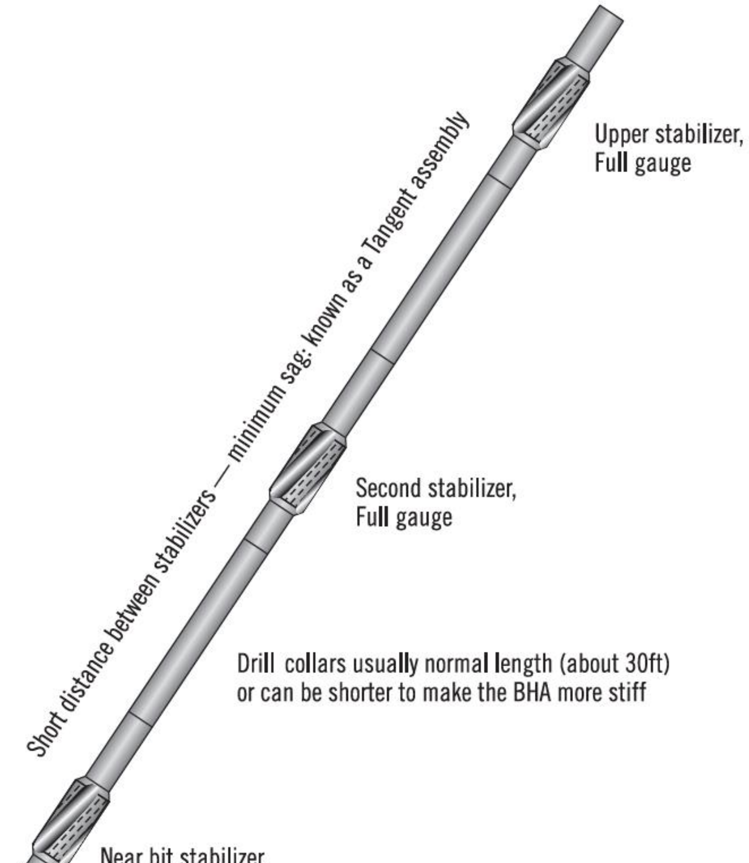

Figure 10 - Packed assembly [12].

2.5.
Measurement and Logging Tools

Other components of the BHA are the logging while drilling (LWD) tool and the measurement while drilling (MWD) device. MWD tools use magnetometers and accelerometers to measure the azimuth and the inclination of the wellbore, besides measuring the downhole temperature, Torque, and Weight on Bit (TOB and WOB), the rotational speed of the drillstring, and the mudflow volume [16].

The LWD tools are usually employed to measure geological features, such as porosity, density, resistivity, inclination at the drill bit, acoustic-caliper, formation pressure, and magnetic resonance. The information keeps in local memory then is extracted when the tool is removed from the well to the surface [16].

2.6.
Drill Bit

A bit is a cutting tool placed at the bottom part of the drillstring. Depending on its type, the drilling action is generated by chipping, gouging, scraping, or grinding the rock. Drilling fluid circulates through nozzles in the bit, cooling it and cleaning the well [4].

Drill bits are separated into fixed cutter bits and roller cone bits (Figure 11). Selecting a good bit is essential to reach greater drilling performance and reduce the cost of drilling [12]. The bit choice for a specific application depends primarily on the formation properties and expected operating conditions while drilling [4]. The bit performance is a function of some criteria such as depth drilled, rate of penetration (ROP), and costs to run per foot of the hole drilled, as well as WOB, mud properties, and hydraulic efficiency [4, 9].

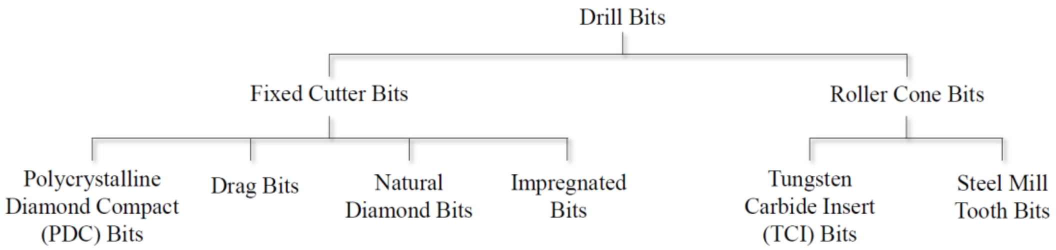

Figure 11 - Types of drill bits.

2.6.1.
Fixed Cutter Bits

Fixed cutter bits are separated into natural diamond bits, impregnated bits, polycrystalline diamond compact (PDC) bits, and drag bits. This type of bit has no moving part, becoming possible to drill longer due to the absence of bearings to wear out, just cutting surfaces [1, 4, 12].

Diamond bits (Figure 12) drill by wearing the rock under the bit, producing tiny cuttings called rock flour. These bits can drill hard rocks, but on the other hand, they are expensive and have a low ROP. Diamond bits are usually employed to drill formations with high compressive strength or very abrasive formations that could destroy other bit types quickly [12].

Figure 12 - Natural Diamond Bits [18].

The Impregnated Bit (IB) is the upgrade of the Diamond Bit, and one of the most representatives. IB bit's body involves the diamond grits dispersed in the copper-based tungsten carbide composite (Metal Matrix Composite) as shown in Figure 13. These bits are generally used to drill harder and more abrasive formations, which the roller cone bits and PDC bits fail to drill through. In addition, high rotary speed is recommended to compensate the small depth of cut of the bit [60].

Figure 13 - (a) Diamond Impregnated Bit, and (b) IB's fractured surface [60].

PDC bits utilize small disks of synthetic diamond to afford cutting/scraping surface [4]. They were introduced to drill soft formations with high ROP and service life, whereas in hard formations, the heat yielded during the drilling breaks the bond between the diamond and the cobalt.

Figure 14 - PDC bit (Wuxi Yaheng Geological Equipment Technical Co.)

PDC bits are manufactured one by one, allowing great flexibility on these bit designs, wherein each cutter can have its properties changed. Characteristics such as number, position, size, and inclination of cutters determine the ROP and bit service life [1].

Drag bits are steel blade bits, known as a *fishtail* (Figure 15). They fail the rock by shearing and were the first bits to be used to drill soft formations. However, their cutting structure service life is short, even applying hard-facing material on their blades. Because of that, these bits are rarely utilized in the industry nowadays [1, 4, 12].

Figure 15 - *Fishtail* drag bit [56].

2.6.2.
Roller Cone Bits

Roller cone bits are made out of cutters, bearings, and the bit body. The cutters are fixed to cones that rotate on bearings relative to the bit body, with the teeth pressing against the formation, applying a pressure greater than the compressive strength of the rock [3, 12]. Regarding the cutters, roller cone bits may be classified into steel milled tooth or tungsten carbide insert, as shown in Figure 16 [1].

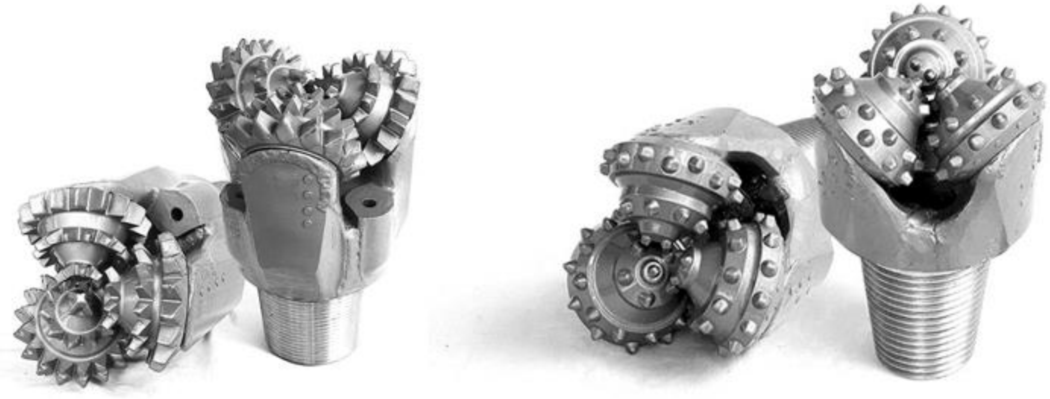

Figure 16 - Steel Milled Tooth (left); Tungsten Carbide Insert (right) [57].

The cutter's action of the roller cone bits includes a combining action of dragging, chipping, crushing, and erosion by the mud's jet action. Depending on the bit's characteristics, one mechanism stands out from the others. Cutters on milled tooth bits are longer, and the cones offset yield the dragging actions, becoming the bits aggressive in soft formations. Meanwhile, insert bits act by crushing the rock, rather than gouging and chipping. Thus, they are designed for hard formations [1, 3].

The three-cone bit commonly has the widest use in rotary drilling operations due to its huge variety of tooth design and bearing types. It can drill a large diversity of formation characteristics [13].

2.7.
Drillstring Design

Designing a drillstring means defining the grade, optimal size, and length of drillstring components to be sufficiently strong, implying minimum cost [4]. Accordingly, the designer should know the drilling fluid weight, total vertical depth expected, tensile safety factor, collapse, internal pressure, and the maximum previewed WOB [1].

The knowledge about the mentioned properties allows the specification of the types of drill pipes and drill collars to be used. There are many sizes, brands, and performance capabilities for each possible component. The designer's problem is choosing the best tool combination that fulfills the drilling specifications. The basic metrics used in this choice are performance, cost, risk, and availability [3].

At first, the drill collars are designed, usually based on the hole and casing diameters, and the following criteria: a) buckling criteria at the bottom end of the column when the WOB is applied (buckling neutral point); and b) the number of drill collars, so that the drill pipes remain always tensioned (tensile neutral point) [1]. Usually, the BHA's components are chosen based on the deviation-control requirements. Afterward, the drill pipe is selected [4].

An intermediate element (HWDP) should be used between drill pipes and drill collars to change the bending stiffness gradually, achieving a stiffness ratio (SR) of adjacent members less than 5.5. The SR is the ratio of section moduli of two adjacent members of the drillstring. Satisfying this demand also requires more than one size of drill collars [4].

The drillstring is subjected to tensile, compression, and torsion stresses while drilling. Eventually, radial stresses are possible, a consequence of extern and intern pressures difference at the pipe. Generally, collapse strength defines the required pipes at the bottom part of the column, and the tensile defines the pipe's strength at the top part [1].

Therefore, Mitchell and Miska [4] propose the following requirements that the final drillstring design must satisfy:

a) The load capacity of any drillstring member, divided by a safety factor, should be greater than or equal to the maximum permissible load;

b) SR of adjacent members must be less than approximately 5.5. The SR is the ratio of the section moduli between two adjacent members of the drillstring.

c) The drillstring geometric properties should be selected in conjunction with an optimal hydraulic and casing program;

d) In deviated wells, drillstring rotation should not produce excessive casing damage;

e) The total cost of the string should be kept to a minimum.

3.

Drillstring Mechanics

The drillstring is a long flexible column with the axial dimension orders of magnitude larger than its cross-section’s [11]. This column has a complex dynamic response because of the formation properties and heterogeneity, misalignment, friction, and BHA imbalance. These factors are generally unknown or not measurable in real-time. Besides, drillstring-wellbore contact, stochastic bit-rock interaction force, mud damping, and excitation sources raises the problem's complexity [20].

In addition, complex drillstring vibrations are generated during the drilling, containing basic forms, frequencies, modes, tool damage, and amplitudes response [5]. The main vibrations are axial, lateral, and torsional (Figure 17), or a combination of these three modes [11, 21, 23].

3.1.

Axial Vibrations

The axial or longitudinal vibrations stand for the motion of the drillstring along its axis of rotation [5]. In some cases, the bit may periodically lose contact with the hole's bottom, normally because of resonance in the axial direction or due to irregularities in the rock surface. This phenomenon is named "bit-bounce" (Figure 17) and can be identified by periodic vibrations on the weight of the column [2, 11, 20, 24].

This vibration frequently occurs when drilling vertical wells, hard rock, or using cone bits and hybrid bits [5].

If not controlled, axial vibrations may cause a decrease of ROP, oscillations on WOB, damage of the borehole, and fatigue of mechanical elements [11].

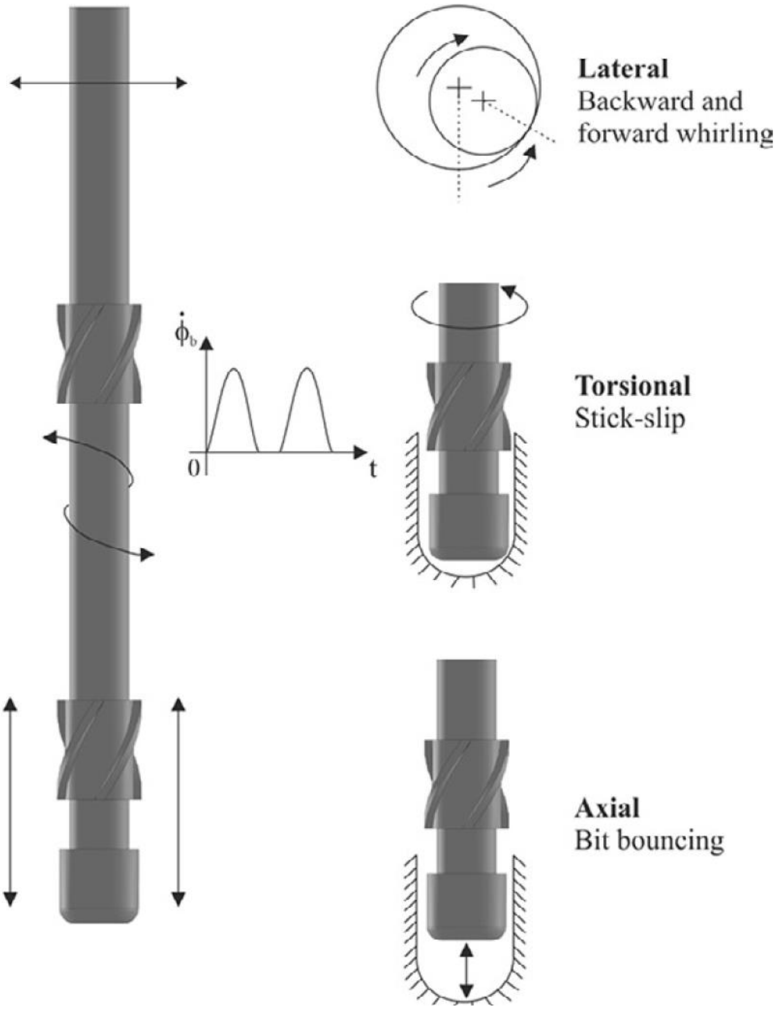

Figure 17 - Lateral, torsional and axial vibrations on a drillstring ($\dot{\phi}_b$ is the drill bit angular velocity; t is the time) [22].

3.2.

Lateral Vibrations

The lateral vibrations (also known as bending [25] or transverse [21] vibrations) are the lateral motion of the drillstring regarding the axis of rotation [5]. Since the column diameter is smaller than the borehole, it can freely vibrate laterally [2].

Kriesels et al. (1999) [26] stated that lateral vibrations are probably the main cause of drillstring and downhole failures. A type of lateral vibration named whirl (Figure 17) results from out-of-balance forces in the BHA. Besides, the friction between the borehole wall and the rotating drillstring may cause a backward whirl. In these cases, the BHA hits the borehole wall at high velocity, causing serious damage to the drill collars, MWD tools, motors, stabilizers wear, and wellbore washout. In addition, high-frequency bending moment fluctuations in the BHA, induced by lateral vibrations, are very difficult to detect due to drillstring-wellbore contact and mud damping [2, 20].

According to Dong and Chen (2016) [5], transverse vibrations usually develop at interbedded or softer formations with different lithology, horizontal or vertical wells. Furthermore, lateral vibrations may occur from drillstring bending during bit bounce and from bit whirl.

3.3.
Torsional Vibrations

Cunha (2015) [11] defined torsional vibration as a mechanism of circumferential oscillation, which may have stationary or transient modes. Variations in drilling conditions, as changes in soil properties and fluctuations in rotation frequency may cause the transient modes. The most probable cause of problems is stationary vibrations, originating from the natural resonance of the drillstring. The most common stationary torsional vibration is the stick-slip (Figure 17) phenomenon. It occurs when the bit stops rotating, even with the top of the drillstring rotating with a constant rotary speed. That happens due to friction between bit/rock, BHA/wellbore wall, and the spring-like nature of the drillstring. After a finite period of stagnation, sufficient potential energy of torsion is stored to overcome the friction. It allows the bit to turn again, achieving more than twice the rotational speed measured at the surface [21, 27].

These vibrations are most likely to develop at salt or hard formations, deep or directional wells, using drag bits, hybrid bits, or PDC bits with high WOB [5]. Moreover, torsional vibrations are accountable for high cyclic stresses on the drill pipe, besides causing irregular downhole rotation, which causes damage to the bit, fatigue failure of the drill collar connections, and slows down the drilling [20, 21].

To summarize, uncontrolled vibrations may cause pipe fatigue, shorten bit life, loss of drilling process efficiency, and sudden drilling direction changes. They may originate worst consequences as drillstring failure and borehole wall collapse. Drillstring vibrations are more drastic at BHA, and the central motifs are the contact of a drillstring with borehole, contact of the bit with the formation, and even misalignment of drillstring, and bent pipes [29].

Figure 18 shows the relationship between the rate of penetration (ROP) and the input energy of the drilling process. It shows that drillstring vibrations may cause a *founder point*, an inefficiency point where the ROP remains constant, even increasing the input energy.

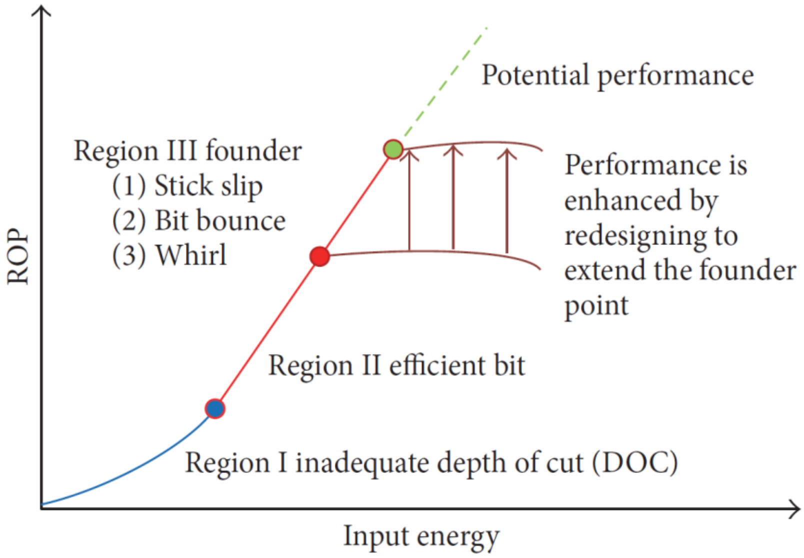

Figure 18 - Relationship between ROP and Input Energy [5].

Sun et al. (2016) [28] explained the graphic’s regions:

Region I: low WOB causes the improper depth of cut (DOC), limiting the drilling efficiency performance.

Region II: begins when the WOB increases, increasing DOC, and the bit approximates from peak efficiency. The bit efficiency stays stable as bit weight is raised to the founder point.

Region III: starts at the founder point, where the input energy is constrained to be transferred to the rock. In this region, if the energy is lost because some inefficiency (for example, the severe vibration modes), the founder point needs to be redesigned to extend the constraining limit for further increasing the ROP. It can be done by improving drilling parameters or increasing input energy if it is not limited by inefficiency (founder) factors.

A founder may occur due to bottom hole balling, bit balling, and drillstring vibrations, for example [28]. Chen et al. (2017) [46] explained bit balling and bottom hole balling as terms used to describe material build-up on the drill bit and bottom hole that inhibits the transfer of a portion of the WOB to the cutting structure.

4.
Numerical Model

Engineering problems are described as mathematical models of physical situations. These models consist of differential equations with a set boundary or/and initial conditions. These equations are obtained by the application of the fundamental laws and principles of nature to the system. They represent the balance of force, mass, or energy. The analytical solutions of these equations would give the best estimate of system's behavior at any point. In many engineering problems, it becomes unfeasible to achieve an analytical solution due to the difficulties of dealing with the initial and boundary conditions and the complex nature of some governing equations [32].

Consequently, numerical solutions are applied. Primarily, the system must be discretized. It consists of dividing the medium of interest into finite small subregions (elements) and nodes. The solution approximates exact solutions at any node. One of the numerical models that apply this kind of discretization is the Finite Element Method (FEM) which applies integral formulations to obtain a system of algebraic equations. Besides, it is assumed a continuous function to represent the approximate solution for each element. Then, a complete solution is given by assembling the individual solutions, keeping the continuity at interelement boundaries [32]. Generally, the discretized algebraic equations are written as a matrix system, relating control variables to state variables. For the displacement-based FEM, the control variables are external forces and moments, and the state variables are displacements and rotations of nodal points [8].

Feng (2017) [31] stated that using FEM to model a drillstring has notable advantages that justify its use, despite being more expensive computationally than other conventional approximation methods. As an advantage, the FEM generates accurate vibrations and dynamics data of the whole string, subjected to a broad type of boundary conditions. Thus, the method can develop a realistic drillstring operation for drilling control, design, and testing. Feng [31] presented a six degree of freedom (DOF) FEM modeling framework to describe the drillstring dynamics, considering a bit-force model, also including the influence of bottom-hole assembly

(BHA) eccentricity, mud damping, bit-rock collisions in lateral, axial, and torsional directions, as well as their coupling mechanisms.

Millheim (1978) [30] defined FEM as a numerical procedure based on piecewise approximation of a complex problem, subdividing it into desired regions, which solution is given for each subdivision. Besides, a beam finite element with six DOF per node and a gapping element to model the closing distance from the borehole centerline to the borehole wall was used to analyze four bottom-hole assemblies. Millheim [30] also cited that an utterly automated sequence of analysis operations independent of boundary considerations and adaptable to general material anisotropy and nonlinearity are available in a finite-element analysis. Spanos et al. (1997) [33] applied FEM to determine the steady-state response of a drillstring monochromatic harmonic excitation, aiming to develop a tool that captures and isolates the effect of any of the sources of potential BHA vibration. The BHA was modeled as an Euler-Bernoulli beam, including the influence of axial force on lateral vibration.

There is a large literature regarding the analysis of different characteristics of the drillstring and BHA. On the other hand, Khulief and Al-Nasser (2005) [29] noticed that modeling both drill pipes and BHA together was not considered in the context of a general finite element formulation. The drillstring analysis generally focuses on the BHA modeling. Therefore, Khulief and Al-Nasser [29] developed a finite element modeling of the entire elastic drillstring, considering the gyroscopic effect, torsional bending inertia coupling, the gravitational stiffening effect, and the tension and compression field associated with the drillstring. The purpose of the work was to provide a basis for modeling the entire drillstring for further development of a complex model with elaborate dynamic effects resulting from bit and borehole contact.

Subsequently, Zare et al. (2011) [34] employed a finite element model using ANSYS software to search the lateral vibrations in drillstrings at slightly deviated wells. Ghasemloonia et al. (2013) [35] also modeled the entire drillstring with FEM to explore the consequences of the imposed vibration of a Vibration-Assisted Rotary Drilling (VARD) force generator on the non-linear coupled axial-transverse dynamics of the vertical drillstring.

This work employs a three-dimensional finite element beam to model and study the nonlinear dynamic behavior of an entire vertical well drillstring. The element has six degrees of freedom (DOF) per node and uses the Euler-Bernoulli beam theory. The column-well contact is modeled as linear springs. At first, a non-linear static analysis is performed to deform the column and apply weight-on-bit. Next, a non-linear dynamic analysis yields the displacements and forces time series. The work may be expanded in further developments to consider friction between the borehole wall and column, bit-rock interaction, mud damping, and buoyancy effect on drillstring analysis. The model is also capable of representing buckling, and a particular study is developed forward.

4.1.
Non-Linear Finite Element Model

Bathe (1996) [36] presented the proper idealization of the real problem as the most crucial step in analyzing a structure using the displacement-based finite element method. Hence, the following hypothesis are assumed for this work:

- Two-nodes element with six DOF each;
- Large displacements and rotations, but small strains;
- Cross-sections remain plane and perpendicular to the beam longitudinal axis after deforming (Euler-Bernoulli beam theory);
- Cross-sections do not warp under torsion;
- Under deformation, there is no area or volume variation.

The fundamental problem in a general non-linear analysis is to find the state of equilibrium of a body corresponding to the applied loads, i.e., the externally applied nodal point forces in the configuration at time t $({}^{t}R)$ must be equal to the nodal point forces correspondent to the element stresses in this configuration $({}^{t}F)$ throughout the complete history of load application [36], i.e.:

$$ {}^{t}R - {}^{t}F = 0 \tag{1} $$

In a static analysis, time is only a convenient variable that denotes different intensities of load applications and correspondingly different configurations. Since the analysis includes path-dependent non-linear geometric conditions (assuming large displacements and rotations), the equilibrium relations must be solved for the complete time range of interest. Thus, a step-by-step incremental solution is employed to solve the problem effectively [36].

The basic approach assumes that the solution for discrete time t is known and that the solution for time $t + \Delta t$ is required (Δt is a chosen time increment). Thus, the objective is to evaluate the complete body's equilibrium positions at discrete time points. In this fashion, the Lagrangian (or material) formulation is used as a solution strategy [36]. Accordingly, the set of positions occupied by the particles characterizes the body's movement, which is the most appropriate formulation for solid mechanics [8].

The principle of virtual work (PVW) is the basis of the displacement-based finite element solution. It states that the equilibrium of a rigid body requires that for any compatible small virtual displacements imposed on a body in its state of equilibrium, the total internal virtual work is equal to the total external virtual work. Besides, all three fundamental mechanics requirements are fulfilled when the PVW is satisfied for all admissible virtual displacements with the stresses obtained adequately from a continuous displacement field that satisfies the displacement boundary conditions [36]. The requirements are:

- Equilibrium equations;
- Compatibility between displacements and deformations;
- Material constitutive law.

Therefore, the equilibrium equation of a body at time $t + \Delta t$, in the Lagrangian incremental analysis, using the principle of virtual displacement can be expressed as:

$$\int_{^{t+\Delta t}V} {}^{t+\Delta t}\tau_{ij}\,\delta_{t+\Delta t}e_{ij}\,d\,^{t+\Delta t}V = {}^{t+\Delta t}\Re \tag{2}$$

where ${}^{t+\Delta t}\tau_{ij}$ are Cartesian components of the Cauchy stress tensor (forces per unit areas in the deformed geometry), $\delta_{t+\Delta t}e_{ij}$ is the strain tensor corresponding to virtual displacements, δu_i are the components of virtual displacement vector imposed on the configuration at time $t + \Delta t$, ${}^{t+\Delta t}V$ is the volume at time $t + \Delta t$, and

$${}^{t+\Delta t}\Re = \int_{^{t+\Delta t}V} {}^{t+\Delta t}f_i^B\,\delta u_i\,d\,^{t+\Delta t}V + \int_{^{t+\Delta t}S_f} {}^{t+\Delta t}f_i^S\,\delta u_i^S\,d\,^{t+\Delta t}S \tag{3}$$

where ${}^{t+\Delta t}f_i^B$ are the components of externally applied forces per unit volume at $t+\Delta t$ (body forces), ${}^{t+\Delta t}f_i^S$ are the components of externally applied surface tractions per unit surface area at time $t+\Delta t$ (surface forces), ${}^{t+\Delta t}S_f$ is the surface at time $t+\Delta t$ on which external tractions are applied, and δu_i^S is the δu_i evaluated on the surface ${}^{t+\Delta t}S_f$.

The right-hand side of Equation (2) is the external virtual work, while the left-hand side is the internal virtual work.

However, body configuration at time $t+\Delta t$ is unknown, and since the body undergoes large displacements, Equation (2) cannot be solved directly. Nevertheless, an approximate solution can be obtained by referring all variables to a previously calculated known equilibrium configuration and linearizing the resulting equation. This work employs the co-rotational formulation to refer the variables.

4.2.
The Co-Rotated Beam Element

The co-rotational (CR) formulation is widespread for analysis that assumes large displacements but small strains [6, 7, 37]. It is applied as an alternative to the traditional updated Lagrangian formulation [38]. In this formulation, the displacements that generate deformations are separated from those accountable for rigid body motion. The former is measured in the corotated configuration (C_{ref}), while the latter is measured in the initial configuration (C_{ini}). The rigid body movements are null when referring to the corotated configuration since the configuration uses a local coordinate system $(X\ Y\ Z)$ that moves along with the body [8]. Figure 19 illustrates the reference configurations for the CR problem.

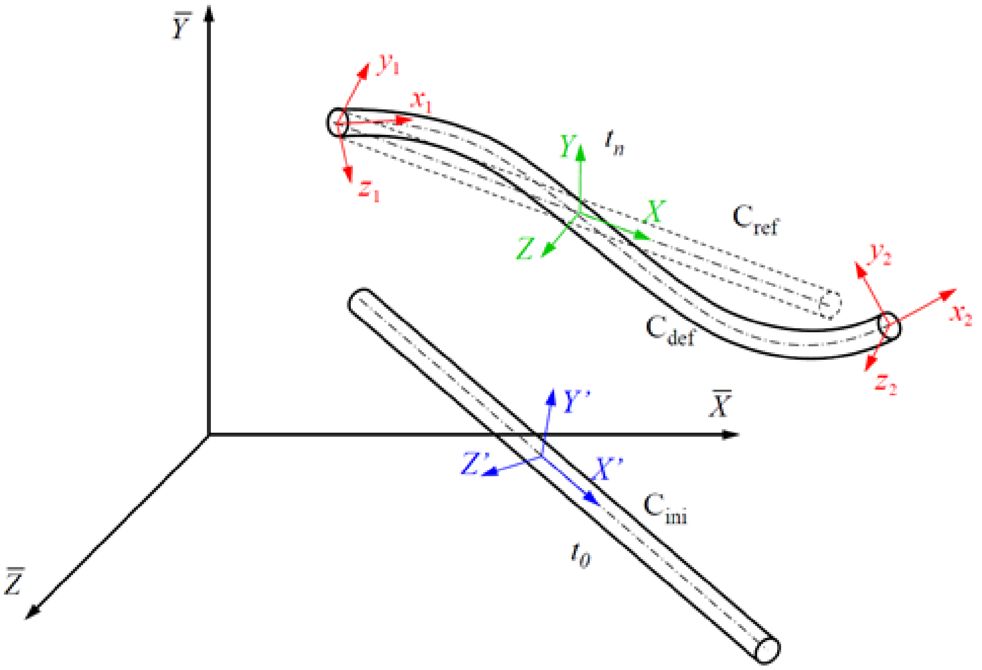

Figure 19 - Beam element reference configurations [6].

The initial configuration (C_{ini}) is the undeformed element configuration at $t = 0$, and the coordinate system related to the element in this configuration is $X'\,Y'\,Z'$. The reference configuration $\left(C_{ref}\right)$ is when the element was subjected to rigid body motions with no straining. Its coordinate system $(X\;Y\;Z)$ results from the rigid body motion of the initial configuration coordinate system. Lastly, the deformed configuration $\left(C_{def}\right)$ is the current element configuration at spatial time t, after deforming and moving with rigid body motions. Their nodes' local coordinate system is $x_i\;y_i\;z_i$. The $\bar{X}\;\bar{Y}\;\bar{Z}$ is the fixed global coordinate system to which the structure is referred to.

4.3.

Formulation for Large Rotations

The assumption of large displacements and rotations leads to the problem of the non-vectorial rotational variables’ nature. In this fashion, a large rotation formulation used by Crisfield [37] and Aguiar [6] was employed.

According to Crisfield [37], the essence of the solution rests on Rodrigues orthogonal rotation matrix **R,** which is used to rotate a vector from an initial $(\mathbf{v_0})$ into a final position $(\mathbf{v_1})$:

$$\mathbf{v_1} = \mathbf{R}(\boldsymbol{\theta})\mathbf{v_0} \tag{4}$$

Deriving the pseudo-vector $\boldsymbol{\theta} = \theta\mathbf{i}$ the matrix **R** is achieved:

$$\mathbf{R} = \mathbf{I} + \frac{\sin\theta}{\theta}\boldsymbol{S}(\boldsymbol{\theta}) + \frac{(1-\cos\theta)}{\theta^2}\boldsymbol{S}(\boldsymbol{\theta})\boldsymbol{S}(\boldsymbol{\theta}) \tag{5}$$

where

$$\boldsymbol{\theta} = [\theta_x \quad \theta_y \quad \theta_z]^T,\ \theta = \sqrt{\theta_x^2 + \theta_y^2 + \theta_z^2} \tag{6}$$

$$\boldsymbol{S}(\boldsymbol{\theta}) = \begin{bmatrix} 0 & -\theta_z & \theta_y \\ \theta_z & 0 & -\theta_x \\ -\theta_y & \theta_x & 0 \end{bmatrix} \text{is the skew-symmetric matrix} \tag{7}$$

where **i** is a unit vector, and **I** is the 3 × 3 identity matrix.

The Rodrigues matrix **R** is used in the CR formulation to update the element reference configuration and the nodal point reference systems.

4.4.
Finite Element Formulation

The linearization of Eq. (2) and referencing of the variables to the co-rotated configuration lead to Eq. (8):

$$\underbrace{\int_V C_{ijrs}\, e_{rs}\, \delta e_{ij}\, dV}_{Linear} + \underbrace{\int_V {}^{t}\tau_{ij}\, \delta\eta_{ij}\, dV}_{Non-Linear} = \underbrace{{}^{t+\Delta t}\Re}_{\substack{External\\ Forces}} - \underbrace{\int_V {}^{t}\tau_{ij}\, \delta e_{ij}\, dV}_{\substack{Internal\\ Forces}} \tag{8}$$

$${}^{t+\Delta t}\Re = \int_V {}^{t+\Delta t}f_i^B \delta u_i dV + \int_S {}^{t+\Delta t}f_i^S \delta u_i dS \tag{9}$$

where C_{ijrs} is the material constitutive tensor, δe_{ij} are the linear incremental strains, $\delta\eta_{ij}$ are the non-linear incremental strains, and ${}^{t}\tau_{ij}$ are known Cauchy stress tensor.

The dynamic response of a structural system diverges from the static response due to the inertial effects [36]. Therefore, to include the inertia forces in the equilibrium equation (Eq. (8)), it is important to consider d'Alembert's principle. Also, dynamic responses of structures dissipate energy during vibration, usually regarding velocity-dependent damping forces. Then, applying Newton's second law to the body forces' component and introducing the damping component in Equation (9) gives [7]:

$${}^{t+\Delta t}\Re = \int_V ({}^{t+\Delta t}f_i^B - \rho\ddot{u}_i - \kappa\dot{u}_i)\delta u_i dV + \int_S {}^{t+\Delta t}f_i^S \delta u_i dS \tag{10}$$

where ρ and κ are material mass density and damping parameter, respectively, and $\ddot{u}_i$ and $\dot{u}_i$ are the acceleration and velocity vector components, respectively.

The substitution of strain tensors by their relations with nodal displacements gives the discretization of the equilibrium equation. In the finite element analysis, the drillstring is approximated by an assemblage of discrete finite elements interconnected at nodal points on element boundaries, as illustrated in Figure 20.

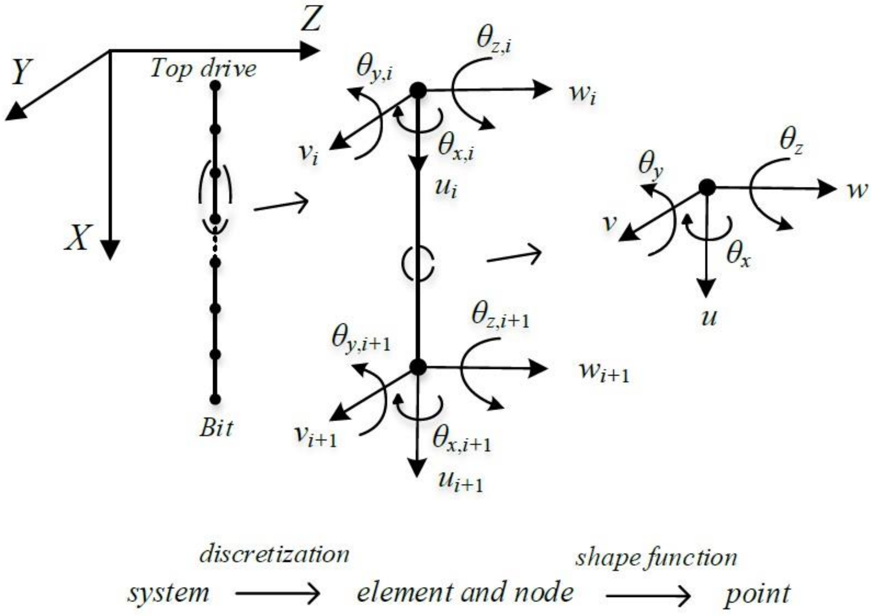

Figure 20 - Finite element discretization and beam element [31].

The displacements measured in a conveniently chosen local coordinate system within each element are accepted as a function of displacements at the N finite element nodal points. Hence, for an element m:

$$\begin{bmatrix} u \\ v \\ w \end{bmatrix} = \boldsymbol{H}^{(\boldsymbol{m})}\boldsymbol{u}^{(m)} \tag{11}$$

where $\boldsymbol{H}^{(\boldsymbol{m})}$ is the interpolation matrix of an element m [6], u, v, w are the material point displacements in X, Y and Z directions, respectively, and $\boldsymbol{u}$ is the vector of global displacement components, i.e.:

$$\boldsymbol{u} = \begin{bmatrix} u_1 & v_1 & w_1 & \theta_{x,1} & \theta_{y,1} & \theta_{z,1} & u_2 & v_2 & w_2 & \theta_{x,2} & \theta_{y,2} & \theta_{z,2} \end{bmatrix}^T \tag{12}$$

The linear and non-linear strains can be expressed as:

$$\boldsymbol{e} = \boldsymbol{B}_L^{(m)}\boldsymbol{u}^{(m)} \quad \text{and} \quad \delta\boldsymbol{e} = \boldsymbol{B}_L^{(m)}\delta\boldsymbol{u}^{(m)} \tag{13}$$

$$\tau_{ij}\delta\eta_{ij} = \delta\boldsymbol{u}^{(m)}\boldsymbol{B}_{NL}^{(m)^T}\boldsymbol{\tau}^{(m)}\boldsymbol{B}_{NL}^{(m)}\boldsymbol{u}^{(m)} \tag{14}$$

where $\boldsymbol{B}_{\mathrm{L}}^{(m)}$ is the linear strain-displacement matrix (or compatibility matrix), obtained by properly differentiating and combining rows of the matrix $\boldsymbol{H}^{(m)}$, $\mathbf{B}_{NL}^{(m)}$ is the non-linear strain-displacement matrix (or geometric compatibility matrix), obtained similarly to the $\boldsymbol{B}_L$ matrix, by taking the corresponding derivatives from the interpolation function, and $\boldsymbol{\tau}$ are the stress components, in local coordinates, obtained from the beam internal forces at the element nodes.

With the element displacements and strains defined in terms of the complete array of finite element assemblage nodal point displacements, the use of Eqs. (11) and (13) in the PVW automatically lead to an effective assemblage process of all element matrices into the structural global matrices [36].

4.4.1.
Element Stiffness Matrices

The substitution of Eq. (13) in the first term of Eq. (8) gives the linear element stiffness matrix:

$$\boldsymbol{K}_L^{(m)} = \int_{V^{(m)}} \boldsymbol{B}_L^{(m)^T} \boldsymbol{C}^{(m)} \boldsymbol{B}_L^{(m)} \, dV^{(m)} \tag{15}$$

where $\boldsymbol{C}$ is the constitutive matrix.

Analogously, substituting Eq. (14) in the second term of Eq. (8), gives the non-linear element stiffness matrix, also known as geometric stiffness matrix:

$$\boldsymbol{K}_{NL}^{(m)} = \int_{V^{(m)}} \boldsymbol{B}_{NL}^{(m)^T} \boldsymbol{\tau}^{(m)} \boldsymbol{B}_{NL}^{(m)} \, dV^{(m)} \tag{16}$$

The sum of linear and geometric stiffness matrices results in the tangent stiffness matrix.

4.4.2.
Element Mass Matrices

The consistent element mass matrix is obtained by substituting Eq. (13) into the inertia term of Eq. (10):

$$\boldsymbol{M}^{(m)} = \int_{V^{(m)}} \rho^{(m)} \boldsymbol{H}^{(m)^T} \boldsymbol{H}^{(m)} \, dV^{(m)} \tag{17}$$

However, this work uses the diagonal lumped mass matrix for all elements. The advantage of using this matrix is memory space-saving and a reduction of a considerable number of operations in the dynamic analysis.

Since the drillstrings are very slender elements and have high axial stiffness, considering rotational mass becomes the effective stiffness matrix (described later) better conditioned. The contribution relative to the rotational mass is added to the bending terms, generating the diagonal mass matrix. The rotational mass is evaluated by calculating the consistent matrix and adding the off-diagonal terms with the same unit as the diagonal term [7]. Hence, the diagonal mass matrix of the element is represented by the following vector:

$$\boldsymbol{M}^{(m)} = \frac{\rho AL}{2}\begin{bmatrix} 1 & 1 & 1 & \frac{I_x}{420A} & \frac{L^2}{210} & \frac{L^2}{210} & 1 & 1 & 1 & \frac{I_x}{420A} & \frac{L^2}{210} & \frac{L^2}{210} \end{bmatrix} \quad (18)$$

where ρ is the specific weight of the material element, A is the structural area of the element, L is the length of the element, and I_x is the torsional inertia of the element.

4.4.3.
Element Damping Matrix

The element damping matrix comes from the substitution of Eq. (13) into the damping term of Eq. (10):

$$\boldsymbol{D}^{(m)} = \int_{V^{(m)}} \kappa^{(m)} \boldsymbol{H}^{(m)^T} \boldsymbol{H}^{(m)}\, dV^{(m)} \quad (19)$$

The element damping parameter $\left(\kappa^{(m)}\right)$ is hardly determined for general finite element assemblages because damping properties are frequency-dependent. As a result, $\boldsymbol{D}$ is calculated using the stiffness and mass matrix of the complete element assemblage, pondering with experimental results on the amount of damping. Then, a linear combination of the global mass and stiffness matrices lead to the structural damping matrix, known as Rayleigh Damping [39]:

$$\boldsymbol{D} = \alpha \boldsymbol{M} + \beta \boldsymbol{K} \quad (20)$$

where α and β are determined from the given damping ratios of two natural vibration modes, with the condition that the modal matrix is orthogonal to $\boldsymbol{D}$.

4.5.
Global Equilibrium Equation

Substituting and rearranging the terms in Eq. (8) gives the semi-discrete governing equation in terms of nodal unknowns (displacements, velocities, and accelerations) for any time t:

$$\boldsymbol{M}\ddot{\boldsymbol{u}}(t) + \boldsymbol{D}\dot{\boldsymbol{u}}(t) + \boldsymbol{K}\boldsymbol{u}(t) = \boldsymbol{F}(t) - \boldsymbol{F}_{int}(t) \tag{21}$$

where $\boldsymbol{M}$ is the global mass matrix, $\boldsymbol{D}$ is the global damping matrix, $\boldsymbol{K}$ is the tangent stiffness matrix, $\boldsymbol{F}$ is the external forces vector, $\boldsymbol{F}_{int}(t)$ is the vector of internal forces, and $\ddot{\boldsymbol{u}}$, $\dot{\boldsymbol{u}}$, $\boldsymbol{u}$ are the vectors of nodal accelerations, velocities, and displacements.

The Equation (21) is a system of second-order ordinary differential equations, which initial value problem is finding a function that satisfies the equation for any time t, wherein $0 \leq t \leq t_{final}$. The initial conditions are $\boldsymbol{u}(0) = \boldsymbol{u}_0$ and $\dot{\boldsymbol{u}}(0) = \dot{\boldsymbol{u}}_0$, where $\boldsymbol{u}_0$ and $\dot{\boldsymbol{u}}_0$ are known.

With an incremental procedure for equilibrium, a numerical solution for the non-linear problem can be obtained. According to Eq. (8), rewriting Equation (21) in the function of incremental displacements, velocities, and accelerations, between time t and $t + \Delta t$, gives:

$$\boldsymbol{M}\ {}^{t+\Delta t}\boldsymbol{\Delta}\ddot{\boldsymbol{u}} + \boldsymbol{D}\ {}^{t+\Delta t}\boldsymbol{\Delta}\dot{\boldsymbol{u}} + \boldsymbol{K}\ {}^{t+\Delta t}\boldsymbol{\Delta}\boldsymbol{u} = {}^{t+\Delta t}\boldsymbol{F} - {}^{t}\boldsymbol{F}_{int} \tag{22}$$

The response of the problem in Eq. (22) requires an integration operator. Commonly, the algorithms employed in structural dynamics are of only one step, i.e., the solution for a determined time value $t + \Delta t$ is calculated as a function only of the solution in the time t, immediately preceding.

The algorithm used to solve the equilibrium equation is the Newmark implicit algorithm, in which accelerations, velocities, and displacements values for $t + \Delta t$ are calculated using the equilibrium equation referred to $t + \Delta t$ [7]:

$${}^{t+\Delta t}\dot{\boldsymbol{u}} = {}^{t}\dot{\boldsymbol{u}} + [(1-\gamma){}^{t}\ddot{\mathbf{u}} + \gamma\ {}^{t+\Delta t}\ddot{\mathbf{u}}]\Delta t \tag{23}$$

$${}^{t+\Delta t}\boldsymbol{u} = {}^{t}\boldsymbol{u} + {}^{t}\dot{\boldsymbol{u}}\Delta t + \left[\left(\frac{1}{2} - \beta\right){}^{t}\ddot{\mathbf{u}} + \beta\ {}^{t+\Delta t}\ddot{\mathbf{u}}\right]\Delta t^2 \tag{24}$$

where β and γ are parameters freely adjusted for good results obtaining in terms of accuracy and stability. For the Newmark algorithm, $\gamma = \frac{1}{2}$ and $\beta = \frac{1}{4}$ for an unconditionally stable algorithm.

Expliciting ${}^{t+\Delta t}\ddot{\boldsymbol{u}}$ in Eq. (24):

$$ {}^{t+\Delta t}\ddot{\boldsymbol{u}} = \frac{1}{\beta \Delta t^2}\underbrace{\left({}^{t+\Delta t}\boldsymbol{u} - {}^{t}\boldsymbol{u}\right)}_{\Delta \boldsymbol{u}} - \frac{1}{\beta \Delta t}\,{}^{t}\dot{\boldsymbol{u}} - \left(\frac{1}{2} - \beta\right){}^{t}\ddot{\boldsymbol{u}} \tag{25} $$

Substituting Eq. (25) into Eq. (23), and grouping the terms, leads to the equation:

$$ {}^{t+\Delta t}\dot{\boldsymbol{u}} = \frac{\gamma}{\beta \Delta t}\Delta \boldsymbol{u} + {}^{t}\dot{\boldsymbol{u}} + \left(1 - \frac{\gamma}{\beta}\right)\,{}^{t}\dot{\boldsymbol{u}} + \left(1 - \frac{\gamma}{2\beta}\right)\Delta t\,{}^{t}\ddot{\boldsymbol{u}} \tag{26} $$

Substituting Eq. (25) and Eq. (26) in Eq. (22):

$$ \boldsymbol{K}_{ef}\Delta \boldsymbol{u} = {}^{t+\Delta t}\boldsymbol{F}_{ef} \tag{27} $$

where

$$ \boldsymbol{K}_{ef} = a_0\boldsymbol{M} + a_1\boldsymbol{D} + \boldsymbol{K} \tag{28} $$

$$ {}^{t+\Delta t}\boldsymbol{F}_{ef} = {}^{t+\Delta t}\boldsymbol{R} - {}^{t}\boldsymbol{F} + \boldsymbol{M}\,{}^{t}\boldsymbol{G} + \boldsymbol{C}\,{}^{t}\boldsymbol{E} \tag{29} $$

$$ {}^{t}\boldsymbol{G} = -a_0{}^{t}\boldsymbol{u} + a_2{}^{t}\dot{\boldsymbol{u}} + a_3{}^{t}\ddot{\boldsymbol{u}} \quad \text{and} \quad {}^{t}\boldsymbol{E} = -a_1{}^{t}\boldsymbol{u} + a_4{}^{t}\dot{\boldsymbol{u}} + a_5{}^{t}\ddot{\boldsymbol{u}} \tag{30} $$

$$ \begin{aligned} a_0 &= \frac{1}{\beta\Delta t^2} & a_3 &= \frac{1}{2\beta} - 1 \\ a_1 &= \frac{\gamma}{\beta\Delta t} & a_4 &= \frac{\gamma}{\beta} - 1 \\ a_2 &= \frac{1}{\beta\Delta t} & a_5 &= \left(\frac{\gamma}{2\beta} - 1\right)\Delta t \end{aligned} \tag{31} $$

As soon as the non-linear process has converged, and with the vector $\boldsymbol{\Delta u}$ obtained, the accelerations and velocities are calculated by using Eq. (25) and Eq. (23).

$$ {}^{t+\Delta t}\ddot{\boldsymbol{u}} = a_0\boldsymbol{\Delta U} - a_2{}^{t}\dot{\boldsymbol{u}} - a_3{}^{t}\ddot{\boldsymbol{u}} \tag{32} $$

$$ {}^{t+\Delta t}\dot{\boldsymbol{u}} = {}^{t}\dot{\boldsymbol{u}} + a_6\,{}^{t}\ddot{\boldsymbol{u}} + a_7\,{}^{t+\Delta t}\ddot{\boldsymbol{u}} \tag{33} $$

where $a_6 = (1-\gamma)\Delta t$ and $a_7 = \gamma\Delta t$.

4.6.
Convergence Criteria

Incremental solutions based on iterative methods need a realistic convergence criteria to effectively terminates the iteration. The algorithm should check if the solution obtained from the iteration converged within prescribed tolerances or if the iteration is diverging. Loose tolerances generate inaccurate results, while too tight tolerances require much computational effort to achieve needless accuracy. Likewise, the iteration can terminate earlier or search for an unattainable solution if an ineffective divergence occurs [36].

The criteria used in this work measure the out-of-balance (residual) load vector and the displacements, as presented in the Eqs. (34) and (35):

$$min\left(\left| {}^{t+\Delta t}\boldsymbol{\Delta u}^{i} \right| \;,\; \frac{\left| {}^{t+\Delta t}\boldsymbol{\Delta u}^{i} \right|}{\left| {}^{t+\Delta t}\boldsymbol{\Delta U}^{i} \right|} \right) \leq \varepsilon_{disp} \tag{34}$$

$$min\left(\left| {}^{t+\Delta t}\boldsymbol{R}_{F}{}^{i} \right| \;,\; \frac{\left| {}^{t+\Delta t}\boldsymbol{R}_{F}{}^{i} \right|}{\left| {}^{t+\Delta t}\boldsymbol{R}_{F}{}^{1} \right|} \right) \leq \varepsilon_{res} \tag{35}$$

where

${}^{t+\Delta t}\boldsymbol{\Delta U}^{i}$ is the accumulated $\boldsymbol{\Delta u}$ vector:

$${}^{t+\Delta t}\boldsymbol{\Delta U}^{i} = {}^{t+\Delta t}\boldsymbol{\Delta U}^{i-1} + {}^{t+\Delta t}\boldsymbol{\Delta u}^{i} \tag{36}$$

${}^{t+\Delta t}\boldsymbol{R}_{F}{}^{i}$ is the residual force vector:

$${}^{t+\Delta t}\boldsymbol{R}_{F}{}^{i} = {}^{t+\Delta t}\boldsymbol{F}_{ef}{}^{i} - {}^{t+\Delta t}\boldsymbol{F}_{int}{}^{i} \tag{37}$$

${}^{t+\Delta t}\boldsymbol{R}_{F}{}^{1}$ is the residual force vector of the first iteration

ε_{disp} is the displacement tolerance

ε_{res} is the residual force tolerance

4.7.
Solution and Element Updating Procedures

Equation (27) may be solved by an iterative-incremental method. Therefore, the internal force vector and matrices must be updated, for each element, at each equilibrium iteration. The updating of the reference systems occurs by using the element incremental displacements and rotations, obtained from the solution process (Eq. (27)) at each iteration-i. The steps used to solve the equation and update the reference systems are described as:

1. Calculate integration constants (See Equation (31)).
2. Initialize initial displacements, velocities, and accelerations:

$$ {}^{0}\boldsymbol{u} = \boldsymbol{0} \quad {}^{0}\dot{\boldsymbol{u}} = \boldsymbol{0} \quad {}^{0}\ddot{\boldsymbol{u}} = \boldsymbol{0} \tag{38} $$

3. Looping in time:

$$ t = t + \Delta t \quad {}^{0}\boldsymbol{\Delta u} = \boldsymbol{0} \quad {}^{0}\boldsymbol{\Delta U} = \boldsymbol{0} \tag{39} $$

$\boldsymbol{\Delta U}$ is the accumulated $\boldsymbol{\Delta u}$ vector, i.e.:

$$ {}^{t+\Delta t}\boldsymbol{\Delta U}^{i} = {}^{t+\Delta t}\boldsymbol{\Delta U}^{i-1} + {}^{t+\Delta t}\boldsymbol{\Delta u}^{i} \tag{40} $$

4. Looping in iterations:

$i = i + 1 \quad , \quad i \le N_{iter}, \quad N_{iter}$ is the maximum number of iterations.

4.1. Update the nodal positions and direction cosines of the element from the incremental displacements ($\boldsymbol{\Delta u^{i}}$) generated from the previous iteration. For the first iteration $\boldsymbol{\Delta u^{i}} = 0$ (from step 3).

4.2. Update element and nodal transformation matrices:

4.2.1. The updating of the nodal rotation matrices ($\mathbf{R}^{i}_{n_1}$ and $\mathbf{R}^{i}_{n_2}$) is performed by applying the nodal incremental rotation matrices ($\mathbf{R}^{i}_{\mathrm{inc}_1}$ and $\mathbf{R}^{i}_{\mathrm{inc}_2}$). These matrices are calculated from the rotation increments using Eq. (5), i. e.:

$$ \boldsymbol{R}^{i}_{n_1} = \boldsymbol{R}^{i}_{inc_1}\,\boldsymbol{R}^{i-1}_{n_1} \qquad \boldsymbol{R}^{i}_{n_2} = \boldsymbol{R}^{i}_{inc_2}\,\boldsymbol{R}^{i-1}_{n_2} \tag{41} $$

4.2.2. The element transformation matrix ($\mathbf{R}^{i}_{e}$) is obtained by combining the updated direction cosines of the element (vector **X**) with the nodal rotation matrices as follows: the first row of R^{i}_{e} is the vector **X**; the second row is the average of the nodal matrices' second rows, i.e., $\mathbf{Y} = \frac{\boldsymbol{R}^{i}_{n_1}(\text{2nd row}) + \boldsymbol{R}^{i}_{n_2}(\text{2nd row})}{2}$; the third row is the cross product of vectors **X** and **Y** ($\mathbf{Z} = \mathbf{X} \times \mathbf{Y}$). Aiming to correct the vector **Y**, the cross product between **Z** and **X** is performed ($\mathbf{Y} = \mathbf{Z} \times \mathbf{X}$). Then:

$$ \boldsymbol{R}^{i}_{e} = [\boldsymbol{X} \quad \boldsymbol{Y} \quad \boldsymbol{Z}]^{T} \tag{42} $$

4.3. Calculate the relative displacement vector $\left(\mathbf{u}_r^i\right)$, in the local element and nodal reference systems.

4.3.1. Calculate relative axial displacement $\Delta\ell^i = \ell^i - \ell^0$, where ℓ^i is the updated deformed length, and ℓ^0 is the initial, undeformed length.

4.3.2. Calculate the nodal relative rotation. Following Crisfield [37] formulation, these rotation angles are generated from the following expressions:

$$\begin{aligned} 2\sin\left(\Delta\theta_{1_x}\right) &= -\mathbf{z}_1\mathbf{Y} + \mathbf{y}_1\mathbf{Z} & 2\sin\left(\Delta\theta_{2_x}\right) &= -\mathbf{z}_2\mathbf{Y} + \mathbf{y}_2\mathbf{Z} \\ 2\sin\left(\Delta\theta_{1_y}\right) &= -\mathbf{x}_1\mathbf{Z} + \mathbf{z}_1\mathbf{X} & 2\sin\left(\Delta\theta_{2_y}\right) &= -\mathbf{x}_2\mathbf{Z} + \mathbf{z}_2\mathbf{X} \\ 2\sin\left(\Delta\theta_{1_z}\right) &= -\mathbf{y}_1\mathbf{X} + \mathbf{x}_1\mathbf{Y} & 2\sin\left(\Delta\theta_{2_z}\right) &= -\mathbf{y}_2\mathbf{X} + \mathbf{x}_2\mathbf{Y} \end{aligned} \tag{43}$$

4.3.3. Assemble relative displacement vector:

$${}^{i}\mathbf{u}_r = \left[\,0\ \ 0\ \ 0\ \ \Delta\theta_{1_x}\ \ \Delta\theta_{1_y}\ \ \Delta\theta_{1_z}\ \ \Delta\ell^i\ \ 0\ \ 0\ \ \Delta\theta_{2_x}\ \ \Delta\theta_{2_y}\ \ \Delta\theta_{2_z}\,\right]^T \tag{44}$$

4.4. Calculate internal force vector in their corresponding reference system (local system):

$$\boldsymbol{f}_{int}^i = \boldsymbol{K}_L^{(m)}\ {}^{i}\boldsymbol{u}_r \tag{45}$$

4.4.1. Transform $\boldsymbol{f}_{int}^i$ to global coordinates:

$$\boldsymbol{f}_G^i = \boldsymbol{R}_e^{G^i}\,\boldsymbol{f}_{int}^i \tag{46}$$

where $\boldsymbol{f}_G^i$ is the element internal force vector in global coordinates, $\boldsymbol{f}_{int}^i$ is the element internal force vector in local coordinates, and $\boldsymbol{R}_e^{G^i}$ is the transformation matrix with the same dimension as the element total number of DOF, i.e.:

$$\boldsymbol{R}_e^{G^i} = \begin{bmatrix} \boldsymbol{R}_e^i & 0 & 0 & 0 \\ 0 & \boldsymbol{R}_e^i & 0 & 0 \\ 0 & 0 & \ddots & 0 \\ 0 & 0 & 0 & \boldsymbol{R}_e^i \end{bmatrix} \tag{47}$$

4.4.2. Assembling each element internal force vector generates the total global internal force vector $\left(\boldsymbol{F}_{int}^i\right)$.

4.5. Calculate the effective stiffness matrix $\left(\mathbf{K}_{ef}\right)$:

$${}^{t+\Delta t}\boldsymbol{K}_{ef}{}^{i} = a_0\ {}^{t+\Delta t}\boldsymbol{M}^i + a_1\ {}^{t+\Delta t}\boldsymbol{D}^i + {}^{t+\Delta t}\boldsymbol{K}^i \tag{48}$$

4.6. Calculate the effective force vector $\left(\boldsymbol{F}_{ef}\right)$:

$$ {}^{t+\Delta t}\boldsymbol{F}_{ef}^{i} = {}^{t+\Delta t}\boldsymbol{R} - {}^{t+\Delta t}\boldsymbol{F}^{i-1} + \boldsymbol{M}\,\boldsymbol{G} + \boldsymbol{D}\,\boldsymbol{E} \tag{49} $$

where

$$ \mathbf{G} = -a_0\,{}^{t+\Delta t}\boldsymbol{\Delta U}^{i-1} + a_2\,{}^{t}\dot{\mathbf{u}} + a_3\,{}^{t}\ddot{\mathbf{u}} $$

and (50)

$$ \mathbf{E} = -a_1\,{}^{t+\Delta t}\boldsymbol{\Delta U}^{i-1} + a_4\,{}^{t}\dot{\mathbf{u}} + a_5\,{}^{t}\ddot{\mathbf{u}} $$

$\boldsymbol{M}$ is the mass matrix, and $\boldsymbol{D}$ is the damping matrix.

4.7. Calculate displacement increments variation (Eq. (27)):

$$ {}^{t+\Delta t}\Delta\boldsymbol{u}^{i} = \left({}^{t+\Delta t}\boldsymbol{K}_{ef}{}^{i}\right)^{-1}\ {}^{t+\Delta t}\boldsymbol{F}_{ef}{}^{i} \tag{51} $$

4.8. Calculate the displacements:

$$ {}^{t+\Delta t}\boldsymbol{u}^{i} = {}^{t+\Delta t}\boldsymbol{u}^{i-1} + {}^{t+\Delta t}\Delta\boldsymbol{u}^{i} \tag{52} $$

4.9. Convergence test: if convergence has not been achieved, return to step 4.

5. Calculate velocities and accelerations using Eqs. (32), (33), and the accumulated vector of incremental displacements $\boldsymbol{\Delta U}$.
6. If final time has not been achieved, return to step 3.

Appendix A presents a simple numerical example describing the entire process (above steps 1 to 6), displaying the vectors and matrices for a cantilever beam under point load.

4.8.
Well-Bore Contact

The drillstring's lateral displacement causes contact with the borehole wall, and the reactive forces keep the drillstring inside the wellbore [31]. Before exceeding the clearance, the BHA lateral displacement remains unconstrained. Afterward, for the nodes whose lateral displacement tends to be larger than the gap, a spring is activated to model the contact with the wall [33]. The contact model considers the well's cross-section as circular as illustrated in Figure 21. The wellbore's coordinate system is the XY's global coordinates, while the contact spring element's is expressed in a local coordinate system $x'y'$.

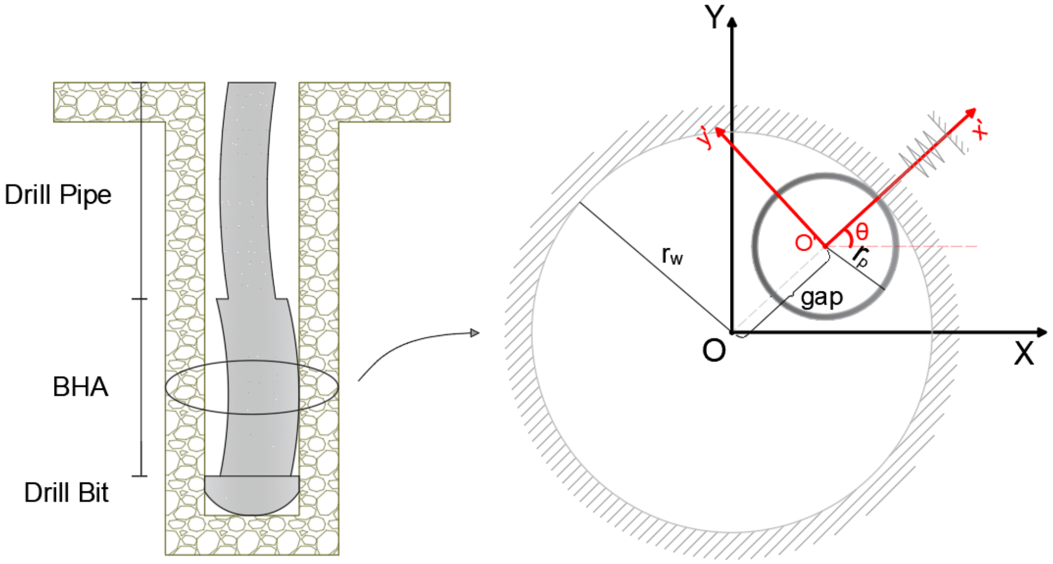

Figure 21 - Drillstring and Wellbore Contact Model.

The direction θ may vary during the solution procedure, leading to convergency issues. Thus, the proposed method fixes the contact direction, leading to a square contact region, as explained next.

The gap is calculated as the subtraction of the well's radius (r_w) by the pipe's radius $\left(r_p\right)$:

$$gap = r_w - r_p \tag{53}$$

The procedure of activation of the spring is described as:

1. Initiate the angle between coordinate systems as $\theta = 0$;
2. Reference the global lateral displacement of the node (U_x and U_y) to the local radial displacement ($\boldsymbol{u}_r$):

$$\boldsymbol{u}_r = \boldsymbol{T}^T \boldsymbol{U}_G \tag{54}$$

where

$\boldsymbol{T}$ is the transformation matrix

$$\boldsymbol{T} = \begin{bmatrix} \cos\theta & -\sin\theta \\ \sin\theta & \cos\theta \end{bmatrix} \tag{55}$$

$\boldsymbol{U}_G$ is the vector with global displacements U_x and U_y of the node.

$$\boldsymbol{U}_G = \begin{bmatrix} U_x \\ U_y \end{bmatrix} \tag{56}$$

3. If the gap is surpassed ($|\boldsymbol{U}_G| > gap$), a force $\boldsymbol{f}_r$ is applied to the node:

$$f_{r_j} = k_s\left(1 - \frac{gap}{|u_{r_j}|}\right)u_{r_j}, \quad j = x, y. \tag{57}$$

$$\boldsymbol{K}_r = \begin{bmatrix} k_s & 0 \\ 0 & k_s \end{bmatrix} \tag{58}$$

where k_s is the borehole contact stiffness, and $\boldsymbol{K}_r$ is the local stiffness matrix of the spring.

4. Transform the force and stiffness matrix to the global coordinate system:

$$\boldsymbol{F}_{r_G} = \boldsymbol{T}\boldsymbol{f}_r \quad \text{and} \quad \boldsymbol{K}_{r_G} = \boldsymbol{T}\boldsymbol{K}_r\boldsymbol{T}^T \tag{59}$$

5. Add the global contact forces vector and stiffness matrix to the global internal forces vector ($\boldsymbol{F}_{int}$) and global stiffness matrix ($\boldsymbol{K}_t$) in their corresponding positions.
6. Hence, this procedure only constrains the global X and Y directions, forming a square contact, still exceeding the wellbore in some points, as shown in Figure 22.

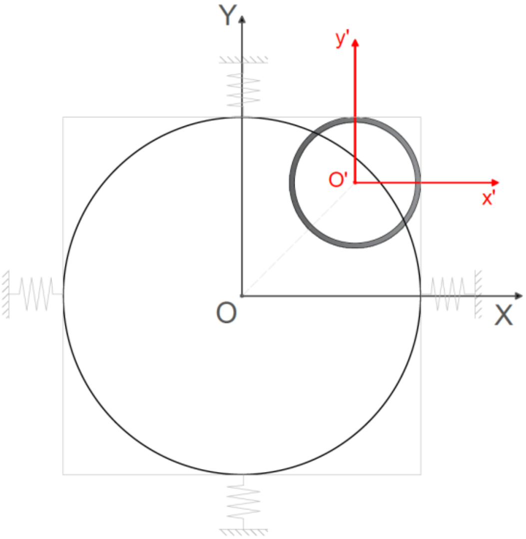

Figure 22 - First procedure application result.

7. The idea for generating a circular contact is to repeat the procedure but rotating the local coordinate system n_r times, with the angle θ within the interval: $0 < \theta < \frac{\pi}{2}$. For example, for a number of radial directions $n_r = 4$, the corresponding constraining region is shown in Figure 23.

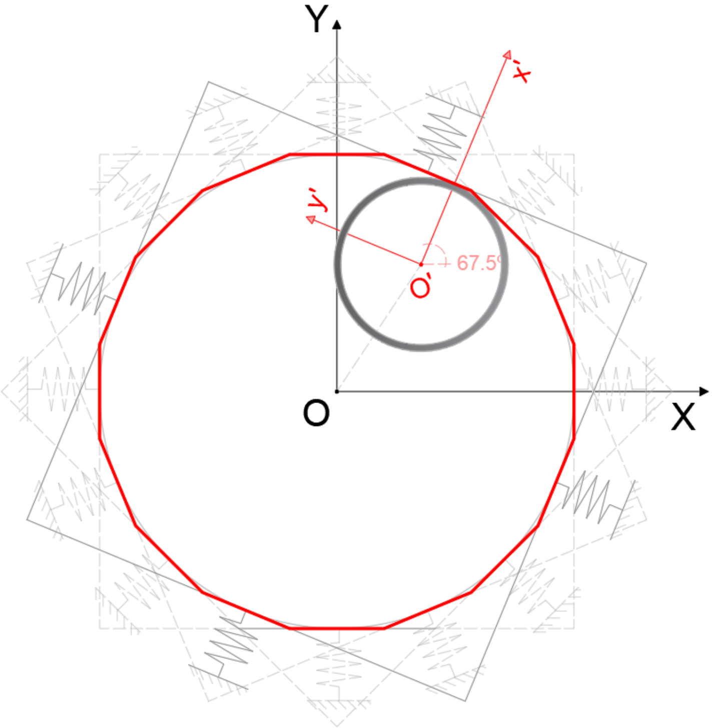

Figure 23 - Constraining region for $n_r = 4$.

At the final step, the solution for $n_r = 4$ produces a polygonal contact, which becomes very similar to a circumference (See Figures Figure 23 and Figure 24). Since the well is not a perfect circumference, the algorithm described is well suited for this analysis. In addition, increasing n_r improves the solution, but it becomes more expensive computationally.

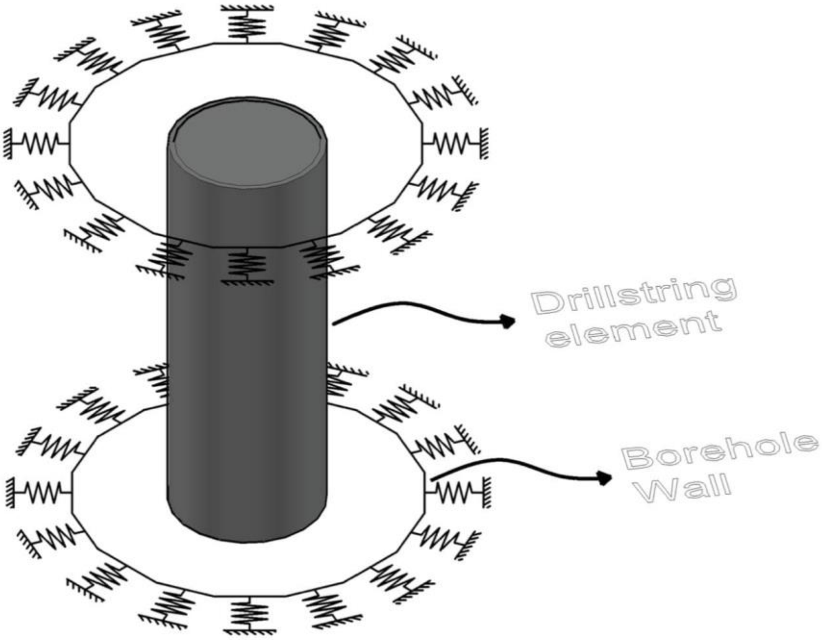

Figure 24 - Final result of the setup spring for contact model in two consecutive constrained nodes.

The contact between the bottom of the drillstring and the rock uses the same procedure, but only one spring in the vertical direction is necessary. Thus, if the vertical displacement U_z of the last node exceeds the gap, a spring is activated to keep the column inside the well:

$$F(z) = F(z) - k_r\left(U_z - z_{gap}\right) \quad \text{and} \quad K(z,z) = K(z,z) + k_r \tag{60}$$

where $F(z)$ is the z component of the global internal forces vector, $K(z,z)$ is the z diagonal component of the global stiffness matrix, k_r is the rock stiffness, and z is the vertical displacement DOF of the column's last node.

5.
Drillstring Buckling

The buckling phenomenon is a mathematical instability that can lead to a failure mode. A column under compressive load buckles when a critical force value is exceeded, and the structure is no longer stable, deforming into a sinusoidal or helical shape. The drillstring in vertical wells may buckle by increasing the WoB over the critical buckling load. When the stability breaks, the string gets in contact with the wellbore. As a result, the frictional interactions could cause buckling lock-up, preventing the drillstring from progressing [41, 45]. In addition, buckling causes tubular string failure, well deviation, casing wear, among others [44].

The earliest work of tubulars buckling was presented by Lubinski (1950) [43]. He analyzed the two-dimensional buckling of pipes in vertical wells and its effects on the shape of the string, bending moments, bit inclination, and wall contact force. Lubinski solved the governing instability problem's differential equation using power series and achieved the critical force for 2D lateral buckling (Table 1). Wu, J. (1992) [50] also developed a critical buckling force for sinusoidal and helical buckling modes.

Lubinski and Althouse (1962) [51] stated later that increasing the WOB leads the tubular string buckle into a three-dimensional (3D) buckling configuration instead of a high-order 2D lateral buckling configuration. They assumed the tubular string is continuously contacting the wellbore and the shape of the deflected string is a helix, which force-pitch relationship was deduced using energy methods:

$$F = \frac{8\pi^2 EI}{p^2} \tag{61}$$

where F is the axial compressive force, EI is the bending stiffness of the string, and p is the pitch of helix.

Table 1 - Critical buckling loads for vertical wellbores.

Buckling Mode	2D Lateral Buckling	Sinusoidal Buckling	Helical Buckling
Dimensionless force $\left(F/\sqrt[3]{EIq^2}\right)$	1.94 and 3.75 (Lubinski [43])	2.55 (Wu [50])	5.55 (Wu [50])

q is the weight in mud per unit of length of the string.

Posteriorly, several works were dedicated to studying buckling and post-buckling behavior. Salies et al. (1994) [40] performed an experimental study of tubulars in vertical wells, discussing some analytical solutions presented in the literature. Menand et al. (2006) [41] showed the influence of friction and tortuosity on the buckling phenomenon for some practical and critical cases met in the drilling industry. In addition, Menand et al. stated that experimental studies show that the critical loads shown in Table 1 may produce good buckling prediction only for a specific and idealized case. Since there are different operational situations, unique buckling criteria valid for all of them cannot exist. Hajianmaleki et al. (2013) [42] used the explicit finite element analysis (FEA) method to model buckling behavior of drillstrings and demonstrated its efficiency, comparing its simulations with analytical solutions and experimental data. Huang et al. (2016) [44] proposed a sophisticated model depicting the complete phase of tubular string buckling in vertical wellbores. The critical buckling loads for 2D and 3D lateral buckling, continuous contact buckling, and helical buckling were calculated. Machado, L. R. (2016) [61] developed a numerical procedure using finite element analysis (FEA) from Abaqus [59] commercial software to analyze the effects of axial loadings on the free portion of the surface casing and evaluate the outcomes of the buckling phenomenon. Xie (2018) [45] also utilized Abaqus [59] finite element analysis, but considering material plasticity and pipe-in-pipe contact, to determine the tubing deformation resulted from buckling.

5.1.
Geometric Imperfections

According to Novoselac et al. (2012) [52], actual structures always have imperfections. These may occur in load application, such as inclination concerning the bar axis or eccentricity regarding the centroid of the cross-sections, and due to geometry imperfections of the bar, such as non-constant cross-section, and residual curvature.

In a numerical buckling analysis, the imperfections are necessary to trigger the buckling occurrence and generate a result next to the real problem. Souza, D. A. (2005) presented some ways to impose imperfections:

- Applying little displacements

- Applying little forces perpendicular to the structure's axis plane
- Initial deformed configuration from buckling modes obtained by linear analysis

This work imposes the imperfection by applying little displacements, as a warping in the initial geometry, following the equation below:

$$x(z) = \frac{d}{kL} sin\left(\frac{n\pi z}{L}\right) \tag{62}$$

where x is the x-coordinate of the column, z is the z-coordinate of the column, d is the outer diameter of the column, L is the length of the column, n is the number of sinusoidal waves, and k is a constant parameter.

6.
Numerical Tests

The incremental-iterative formulation presented, considering contact and buckling analysis, was implemented in a computer program using the Mathworks' MATLAB [58] software. Some examples were developed to compare to results from the literature and verify formulation's performance.

According to Mourelle (1993) [7], the comparison with academic examples is essential for debugging code's or formulation's errors. When the latter happens, it is needed to return to theory or implementation and test again later. This exercise is crucial for generating scientific programs and characterizes the development process cycle.

6.1.
Straight Cantilever Beam under Constant Bending

Figure 25 illustrates a cantilever beam, initially straight pipe cross-section, subjected to an end moment. Several authors [6, 7, 37, 38] suggested the problem for checking the three-dimension beam elements' numerical behavior under intense geometric nonlinearities due to large displacements and rotations. The example performs a classical solid mechanics problem, discretized into 10 elements, and compares the numerical results to the analytical ones.

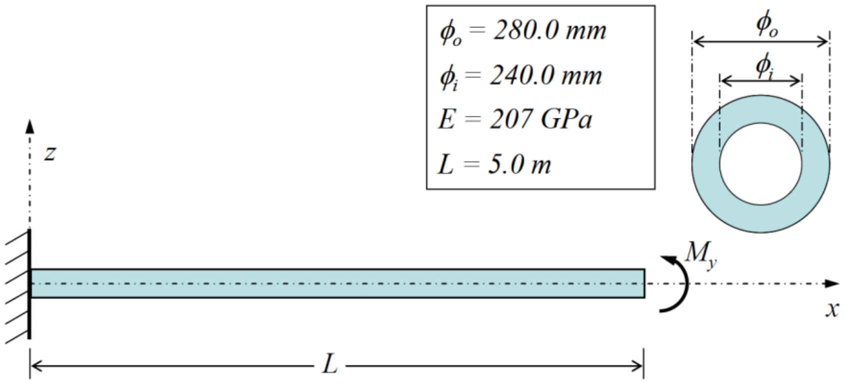

Figure 25 - Cantilever beam under pure bending [6].

The moment applied at the end has the exact magnitude that causes a 2π rotation. Since the tip's rotation of a cantilever beam subjected to a moment at the end is:

$$\theta = \frac{M_y L}{EI} \tag{63}$$

the moment required for $\theta = 2\pi$ is:

$$M_y = 2\pi \frac{EI}{L} \tag{64}$$

After the applied moment, the final deformed configuration must show both beam ends at the same position, as illustrated in Figure 26. The Equations (65) and (66) give the exact result of the horizontal (U_x) and vertical (U_z) displacement of the tip:

$$U_x = L\left(1 - \frac{\sin\theta}{\theta}\right) \tag{65}$$

$$U_z = L\left(\frac{1-\cos\theta}{\theta}\right) \tag{66}$$

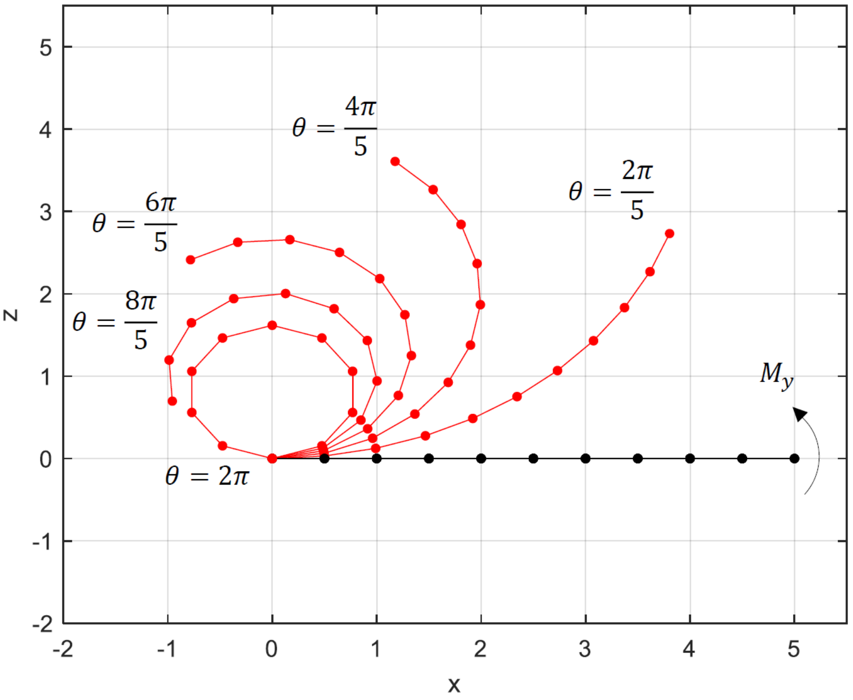

Figure 26 - Deformed configurations.

The comparisons of numerical results for the application of the moment in 20 equally spaced incremental steps to analytical results are illustrated in the Figure 27 and Figure 28:

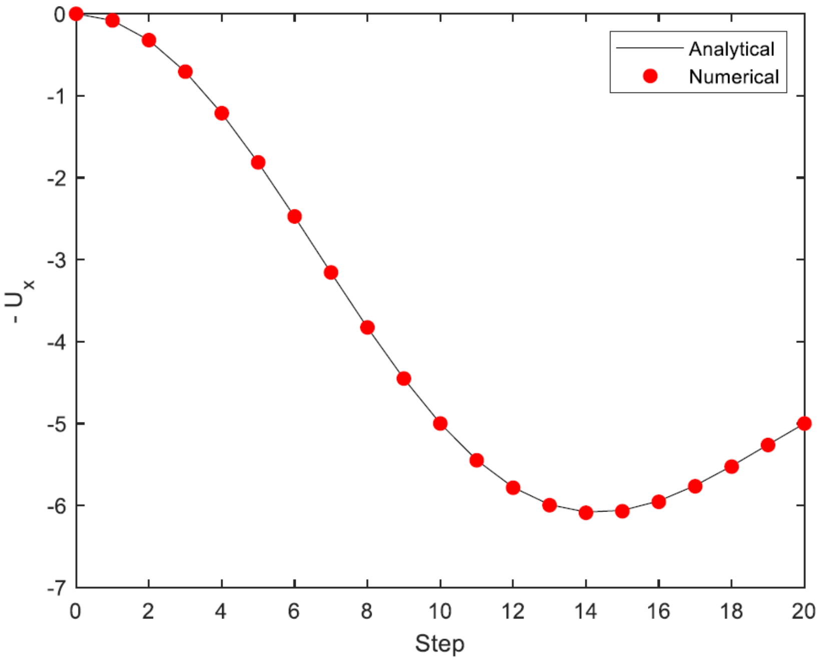

Figure 27 - Horizontal displacement of beam's tip.

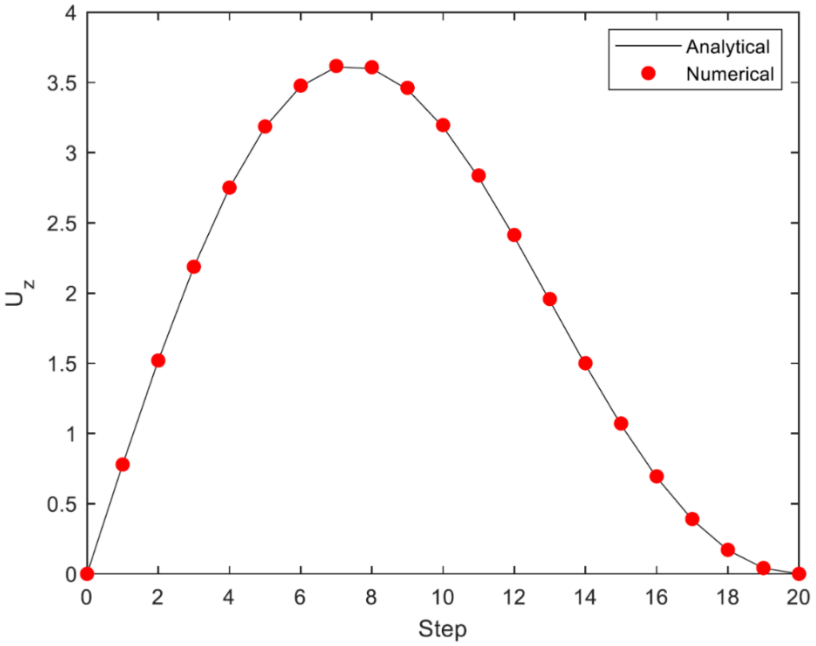

Figure 28 - Vertical displacement of the beam's tip.

The relative error between solutions is calculated as follows:

$$err = \frac{\left| |U_{analytic}| - |U_{numeric}| \right|}{|U_{analytic}|} \tag{67}$$

Increasing the number of elements in the discretization of the structure lowers the relative error, as presented in Table 2.

Table 2 - Displacements' relative errors regarding the number of elements.

Number of elements	Relative error (%)	
	U_x	U_z
5	0.3209	1.1902
10	0.0802	0.2945
15	0.0362	0.1307
20	0.0210	0.0735

The comparisons presented in Figure 27 and Figure 28 and Table 2 shows a good agreement between the displacements results.

6.2.

Slender Column Subjected to Compressive Load

The example represents a slender column with all degrees of freedom fixed at the basis and free at the top end, subjected to a compressive load that causes a lateral buckling (Figure 29). The problem focuses on analyzing the column's behavior in a condition of post-buckling, comparing with results from the literature.

The column is discretized into ten elements equally spaced, and the critical load that yields a first mode buckling $P_{crit} = \pi^2 EI/4L^2$ [48] is applied in 400 steps. Besides, the analysis uses a lateral force (Q) at the free end to stimulate buckling. This force is 0.1% of the critical load P_{crit}, and occurs as shown in Figure 29.

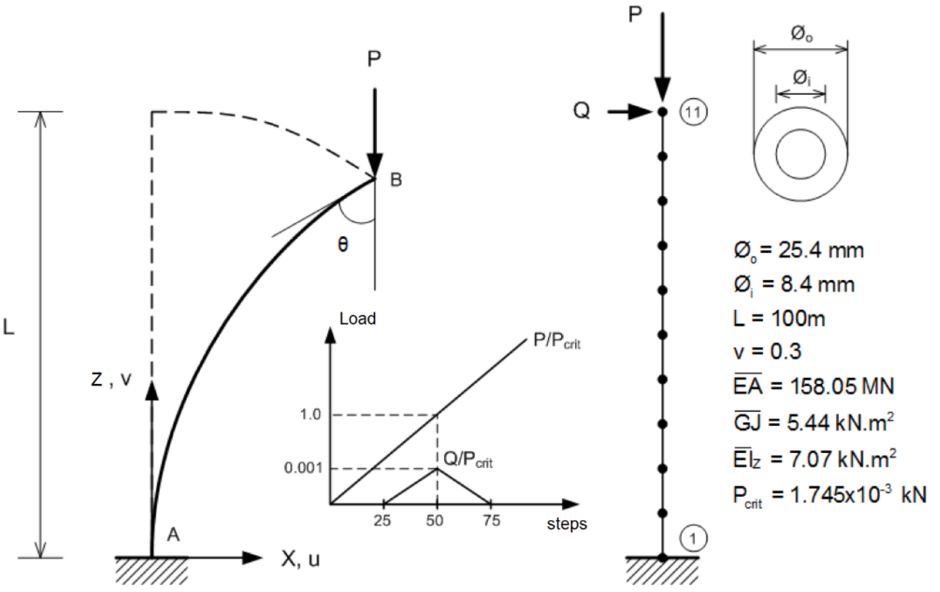

Figure 29 - Slender column subjected to compressive load (Adapted from ref. [47]).

Figure 30 shows solutions for several normalized displacement values at the free end. In addition, Figure 31 illustrates deformed configurations for different compressive load (P) values. The parameter λ indicates the load ratio (P/P_{crit}).

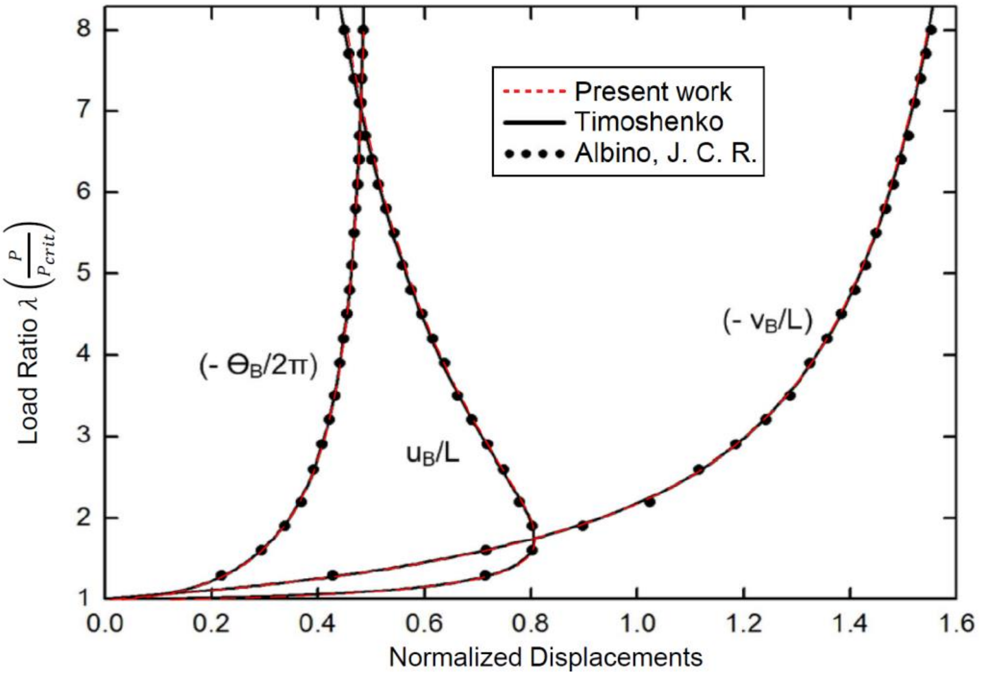

Figure 30 - Displacements and rotations at the free end of the column.

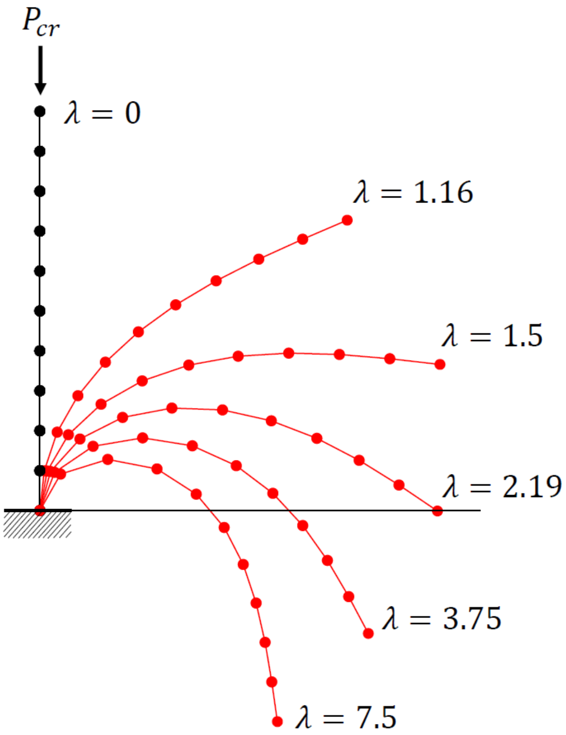

Figure 31 - Column deformed configurations.

The results shown in Figure 30 and Figure 31 demonstrate a good agreement of the compared parameters, validating the present work analysis.

6.3.
Composite Column Subjected to Eccentric Load

Nunes et al. (2003) [49] proposed this example for analyzing the tubular cross-section composite column subjected to eccentric loading. The purpose is to verify and compare the vertical and lateral displacements results and rotation of the column's tip with the available results from the literature. The structure was discretized into 22 elements, two for the connections at the middle and top of the column and ten identical beam elements for each segment. One hundred steps were used for incrementally applying the compression load, generating the numerical solutions. Figure 32 introduces the column's properties, shape, and loading.

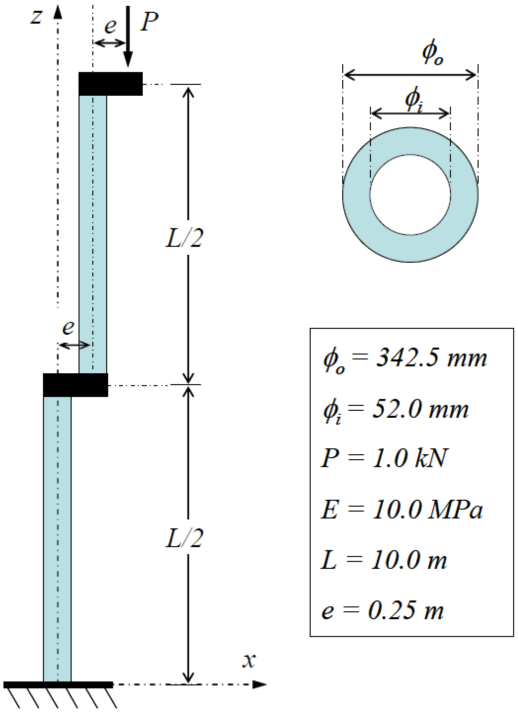

Figure 32 - Composite column subjected to eccentric axial load [6]

Figures Figure 33 and Figure 34 show some deformed shapes of the column under different load steps and the comparison between the numerical and analytical solution of the bending moment distribution along the column for $P = 0.2P$. Besides, Figure 35 shows that the solutions of normalized displacements and rotation at the column's tip of the present work display excellent agreement with others authors' results.

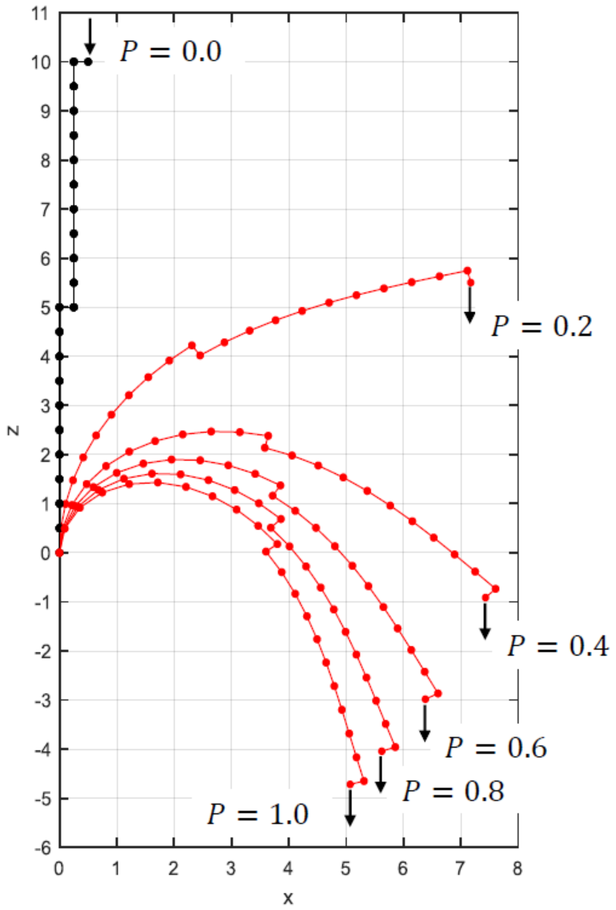

Figure 33 - Deformed configurations

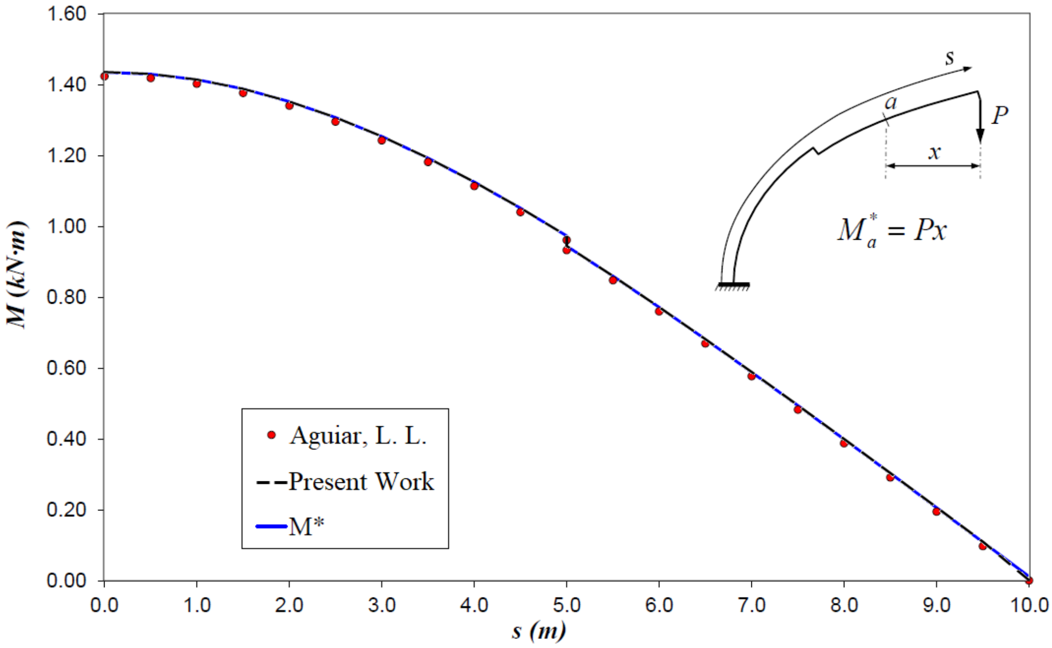

Figure 34 - Bending moment through the column, for $P = 0.2P$.

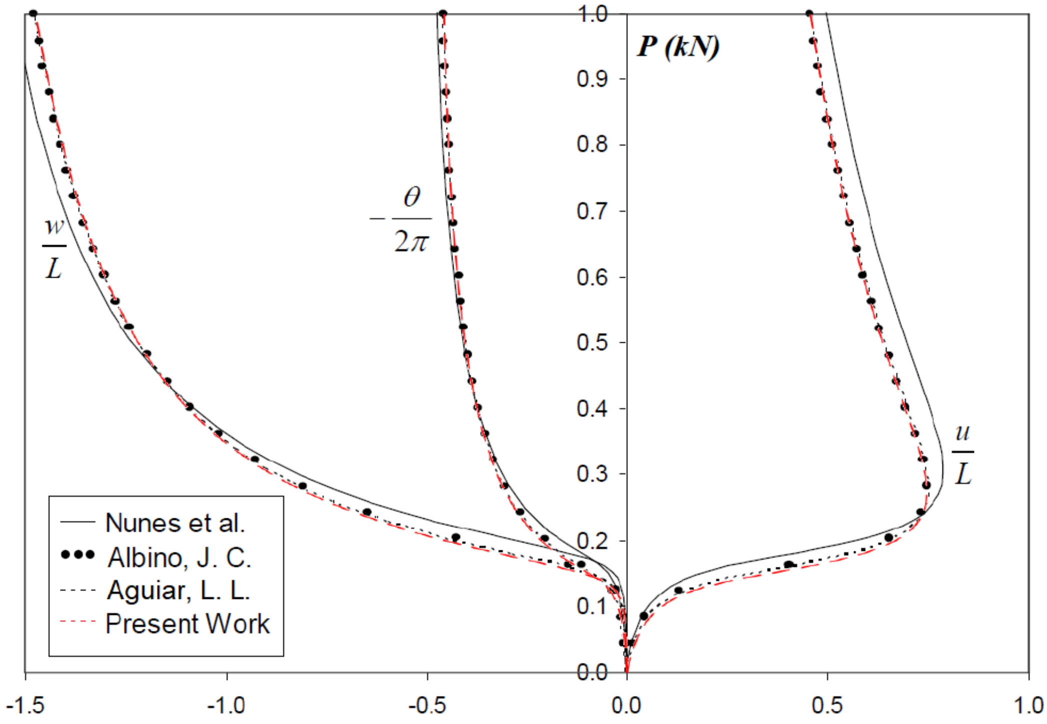

Figure 35 - Normalized displacements solutions at the top of the column comparison.

6.4.
Tubing under Compression Inside Well

This example studies the buckling behavior of a 100 m tubing under compression, applying this compression in two distinct ways. The tubing, as the drillstring, is a long column with a tubular cross-section working confined by the wellbore. The analysis proceeds in four different cases described in Table 3 and Figure 36. In all analyses, the top node (A) is fixed, and the bottom node (B) is constrained only laterally, except for the case 1, where the bottom node (B) is also constrained vertically. One case differs from the other by the column’s compression method and geometric imperfection considered to stimulate buckling. Case 1 considers the well’s length longer than the tubing length, so the string can deform in the static analysis, due to its self-weight, until it touches the bottom and activates the contact method of Equation (59). The extended well length is equal to the value z_{gap} presented in the same equation. Cases 2-4 do not consider contact in the bottom. The column is free to deform statically in these cases, and the force application begins in the dynamic phase. Moreover, Case 4 applies a moment M_z on the bottom node to simulate a constant friction between rock and column.

The objective of the example is to represent the buckling of the tubing and analyze the effect of distinct compression methods and geometric imperfection applied. Besides, the contact methods are verified.

Table 3 - Analysis specifications.

Specifications	Case 1	Case 2	Case 3	Case 4
Geometric/Load Imperfection	Sinusoidal Warping	Sinusoidal Warping	Lateral Force	Lateral Force
Compression Method	Displacement	Force	Force	Force
Additional	Extended Well	-	-	M_z

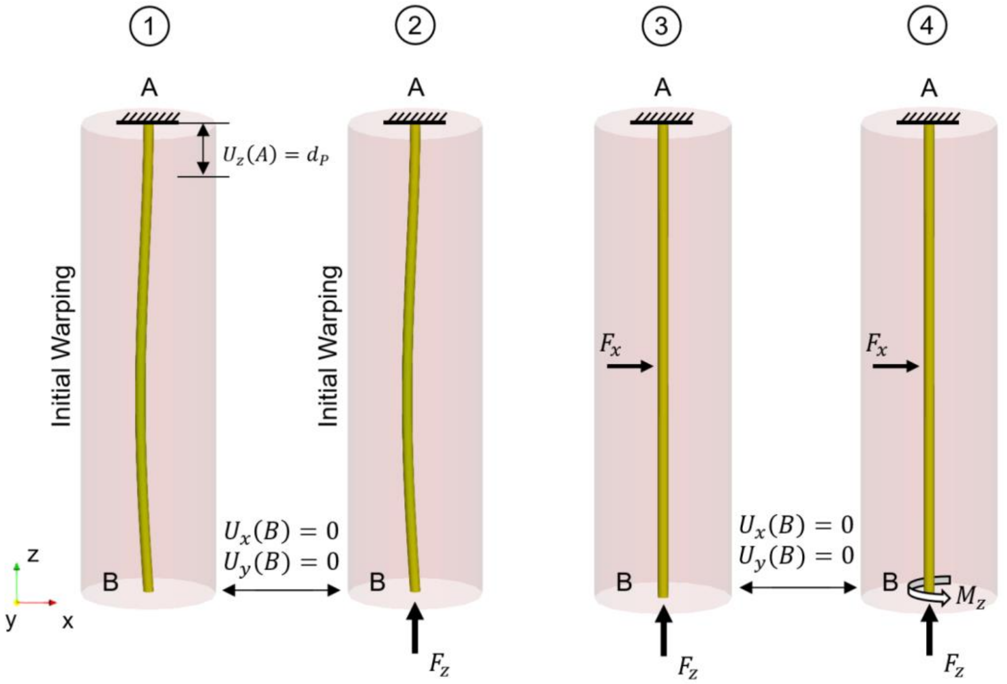

Figure 36 - Schematic representation of analysis' models.

The Table 4 presents all the parameters considered for the analysis.

Table 4 - Analysis parameters.

Outer Diameter (mm)	88.9	Rock Stiffness (k_r)	10^{11}
Inner Diameter (mm)	75.9968	Mz (kN.m)	7.14
Length (m)	100.0	F_z (kN/s)	5.00
Density (kg/m³)	9095.87	F_x (N)	10^{-2}
Gap (mm)	13.3	d_P (mm/s)	5.00
Elements	200	Static Analysis Steps	10
Young's Modulus (GPa)	206.84	Δt (s)	0.01

z_{gap} (m)	0.002	Displacements Scale	250
Soil Stiffness (k_s)	10^4	Well Length	100.0 + z_{gap}

Figure 37 shows the deformed shape of the column for some values of top displacement (Case 1). The program first performed a static analysis to let the column deform and accommodate at the well's bottom in order to make the dynamic process smoother. In this case, the dynamic analysis was used as a way to obtain the post-buckling behavior of the column, since the static analysis diverges when an instability problem occurs.

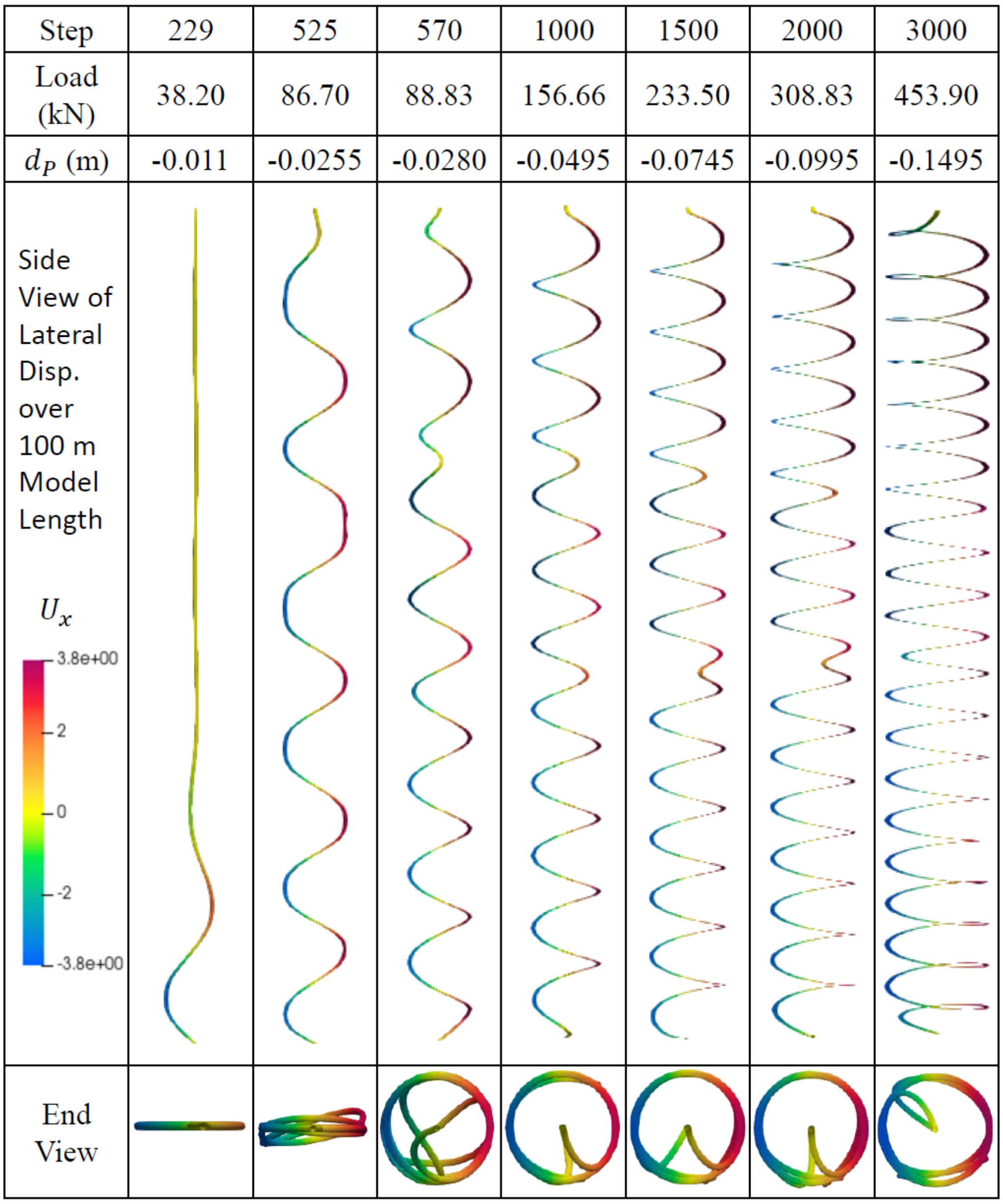

Step	229	525	570	1000	1500	2000	3000
Load (kN)	38.20	86.70	88.83	156.66	233.50	308.83	453.90
d_P (m)	-0.011	-0.0255	-0.0280	-0.0495	-0.0745	-0.0995	-0.1495

Figure 37 - Tubing lateral displacements for some values of top vertical displacement (d_P).

In step 3000, the soil stiffness was insufficient to keep the column inside the well, and the displacement was higher. It can be corrected by raising the soil stiffness, but the analysis convergence may be compromised.

The tubing behavior was as expected; as the compression increases through steps, it first buckles into a 2D lateral mode, then into a sinusoidal way with more waves than the first mode, then into a 3D shape, and finally into a helical mode. For better visualization, the critical load for sinusoidal and helicoidal buckling were considered the loads that generate the shapes in steps 229 and 525, respectively, presented in Figure 37. The value is acceptable since it is close to the value which the buckles considered begin.

Figure 38 represents the bottom node force through the steps. In a drillstring, it would be considered the WOB variation. Around step 520 ($F_x = 86.7\ kN$), instability occurs, and it is related to the beginning of the helical buckling mode. The vibrations observed is due to the inertia effects.

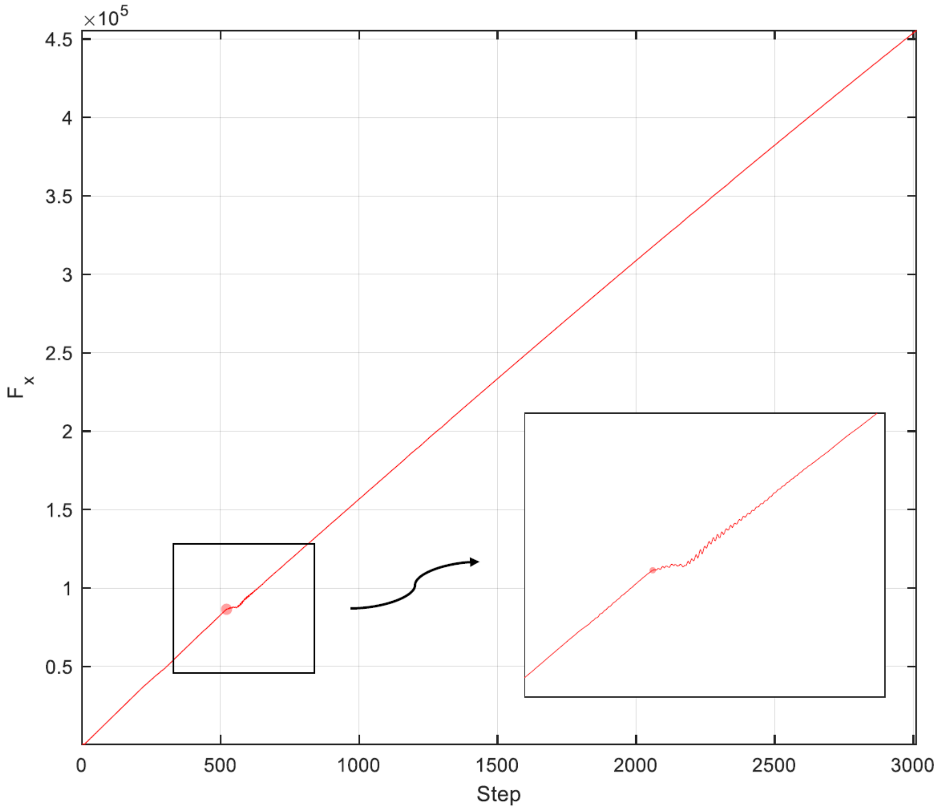

Figure 38 - Bottom node force series.

The buckling modes are also coherent with the model presented by Huang et al. (2016) [44], shown in Figure 39. In Figure 39a, the string is in an initial straight configuration, and as the WOB increases, the column becomes unstable and curves in a 2D plane (Figure 39b). When the WOB exceeds another critical value, the tubular string buckles into a 3D curved configuration (Figure 39d). Still increasing WOB, the column converts into continuous contact with the wellbore (Figure 39e) and finally into a helical shape (Figure 39f).

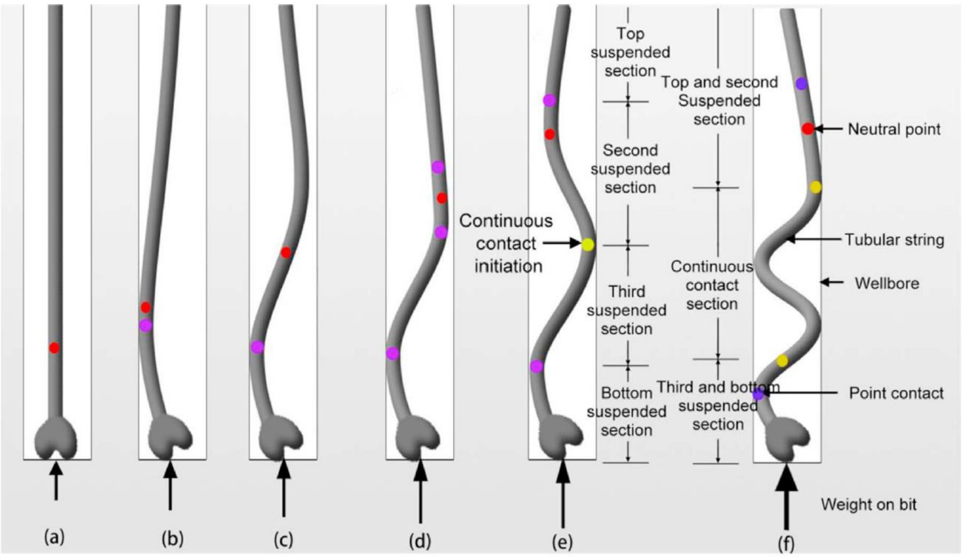

Figure 39 - Buckling mode transitions: (a) initial configurations, (b) First-order 2D lateral buckling, (c) second-order 2D lateral buckling (sinusoidal), (d) 3D lateral buckling, (e) continuous contact buckling and (f) helical buckling..

In addition, a parametric analysis on the parameters of Equation (62) was performed for Case 1. The test varies the parameters k and n to verify their effect on the buckling behavior.

Table 5 - Variation of parameter n with $k = 10$.

	d_P (m)	Step	F_{cr}(sin)	d_P (m)	Step	F_{cr}(hel.)
$n = 1$	-0.01095	229	38.2E+3	-0.02575	525	86.7E+3
$n = 2$	-0.01095	229	38.0E+3	-0.02720	524	87.9E+3
$n = 3$	-0.01010	212	35.1E+3	-0.02910	592	97.1E+3
$n = 4$	-0.00985	207	34.3E+3	-0.02680	546	88.9E+3
$n = 5$	-0.00920	194	32.1E+3	-0.02860	582	95.2E+3
Mean	-0.01021	214	35.56E+3	-0.02749	554	91.2E+3
Deviation	0.00075	15	2.6E+3	0.00136	32	4.7E+3

Table 6 - Variation of parameter k with $n = 1$.

	d_P (m)	Step	F_{cr}(sin)	d_P (m)	Step	F_{cr}(hel.)
$k = 0.01$	-0.00595	129	21.0E+3	-0.02235	457	75.6E+3
$k = 2.50$	-0.01060	222	36.8E+3	-0.02780	566	93.4E+3
$k = 5.00$	-0.01095	229	38.0E+3	-0.02595	529	86.6E+3
$k = 7.50$	-0.01125	235	39.1E+3	-0.02595	529	87.3E+3
$k = 10$	-0.01095	229	38.2E+3	-0.02575	525	86.7E+3
Mean	-0.00994	209	34.6E+3	-0.02556	521	85.9E+3

Deviation	0.00224	45	7.7E+3	0.00198	40	6.4E+3

These results show that the change in the number of sinusoidal waves (n) does not affect significantly the critical loads. The same occurs for the parameter k, for $k > 2.5$. The value $k = 0.01$ leads to a high amplitude of initial warp that would not represent an imperfection, but an initial deformation, which affects the buckling behavior. Therefore, the values chosen for the analysis were $n = 1$ and $k = 10$.

Table 7 compares the values of critical loads of Cases 1-3. After deforming in the static phase, the force application begins in the dynamic with the tubing tensioned, due to its self-weight. The load increment was 5 kN/s, and the deformed shapes were similar to Figure 37. Because the column is short (100 m), there was no significant difference between the force and displacement applications in the buckling behavior. However, as shown in Table 7, there is a difference in the critical forces, which also varies depending on the geometric imperfection considered. Since the analytical solutions are deduced on different assumptions, each buckling load may represent a particular situation, generating conservative values for critical loads. Xie, J. (2018) [45] stated that the critical loads predicted using these analytical solutions could provide overly conservative values for design purposes. Cebeci et al. (2019) [62] concluded from their analysis that analytical solutions give only a fixed critical buckling force for a specific pipe independent from the length, and it may underestimate the critical buckling force.

Table 7 - Critical Loads comparison.

Cases	F_{cr} (sin.) kN	F_{cr} (hel.) kN
Case 1	38.20	86.70
Case 2	20.96	97.71
Case 3	23.96	104.96
Analytical	3.68 [43] 4.78 [50]	10.30 [50]

The drill bit resistance, represented by imposing a moment Mz at the tubing's bottom node (Case 4) makes the column to previously buckle into a 3D shape. Moreover, buckling occurs with smaller load than the case without friction.

The moment applied was the one that generates a rotation of π rad, i.e.:

$$M_z = \pi \frac{GJ}{L} \tag{68}$$

where GJ/L is the torsion elastic stiffness. The analysis applies the moment incrementally at the static analysis and keeps it constant during the dynamic analysis.

Figure 40 presents the deformed shapes for different forces of Case 4.

Step	480	520	560	811	1500	2000	3000
Load (kN)	23.46	25.46	27.46	40.01	74.46	99.46	149.46

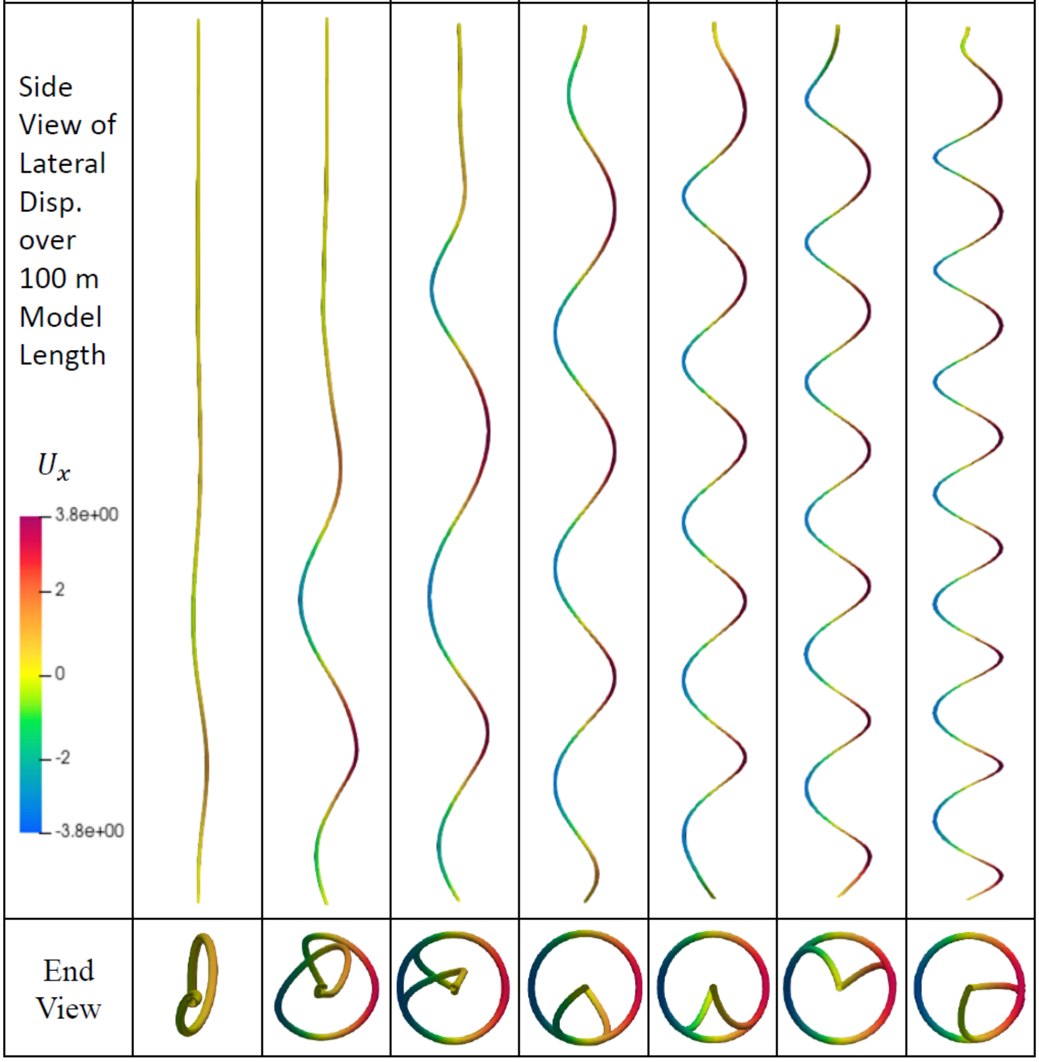

Figure 40 - Tubing lateral displacements for some force values, with friction between rock and column.

6.5.
Long Rotating Drillstring

The objective of this example is to analyze the behavior of a long and complete drillstring. The model consists of a 4.000 m column, with drill pipes, heavyweight drill pipes, drill collars, and drill bit, with properties as shown in Table

8. Initially, the study performs a static analysis, applying the column's weight and deforming the structure axially. The compression process starts at the dynamic analysis when a compressive force is applied incrementally. When the WOB reaches the desired value, the drillstring begins to rotate. Table 8 also presents the pipes properties and analysis parameters.

Table 8 - Pipes Properties and Analysis Parameters

	DP	HWDP	DC	DB
Outer Diameter (mm)	139.7	139.7	165.0	215.9
Inner Diameter (mm)	121.0	82.0	82.0	-
Length (m)	3812.04	169.06	18.56	0.34
Properties				
Total Pipe Length (m)	4000			
Density (kg/m³)	7860			
Well ID (mm)	222.4			
Young's Modulus (GPa)	210			
Analysis Parameters				
Contact Stiffness (k_s – N/m)	10^7			
Drillstring Rotary Speed (RPM)	80.0			
WOB (kN)	80.0			
Force ratio (kN/s)	5.00			
Static Steps	150			
Δt (s)	0.01			
Displacements Scale	250			

The complexity of the analysis grows with the increase of the column's length. A long drillstring is more vulnerable to inertial forces, which may affect the behavior of the structure. For example, applying a large displacement, rotation or force in a short time would be like giving a huge blow on the column. This blow takes time to propagate through the entire column and may oscillate until it dissipates, and simulating it numerically leads to an expensive computational analysis. The mentioned behavior is not that relevant in short columns since the impact dissipates quickly. Therefore, in this example, the torsional portion of the mass matrix is removed so that the drillstring rotation can be applied quickly, without undesired inertia effects. The strategy is valid since friction is not considered. It means that the dynamic behavior of the rotating column without torsional inertia will be very similar to the actual column when the rotation imposed propagates through the entire drillstring and then stabilize. In addition, for the same reason, the compressive force is slowly applied incrementally, with the ratio presented in the Table 8 and illustrated in Figure 41.

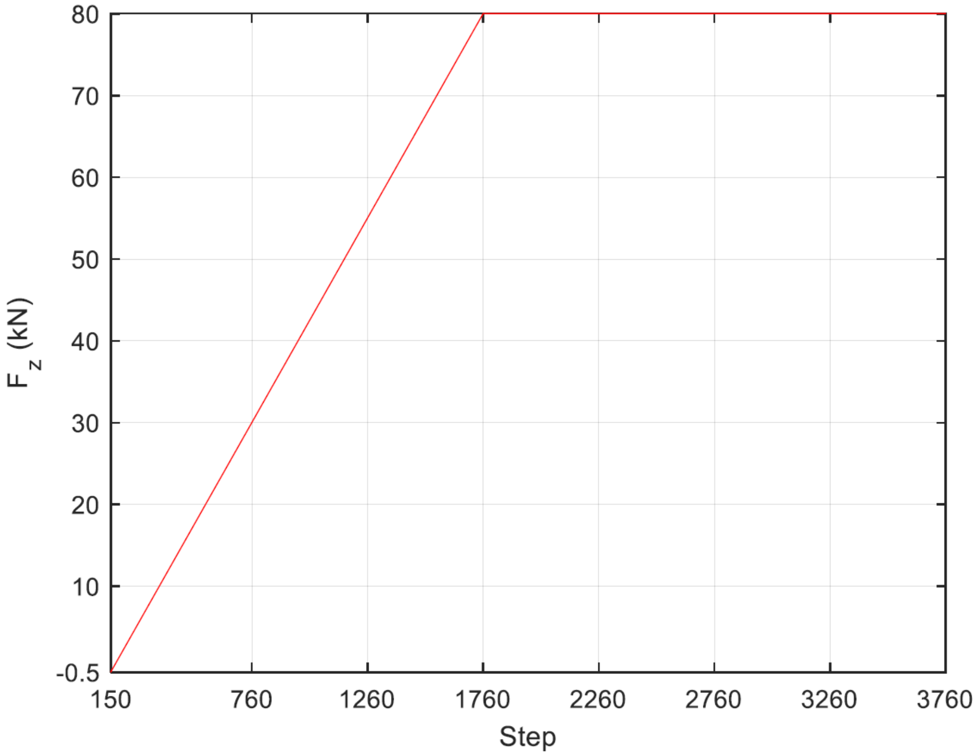

Figure 41 - Weight on Bit through time.

The difference of the column’s response to the cases with and without torsional inertia is presented in Figure 42. The graphic shows the rotation (θ_z) through 20s of analysis for the top and bottom nodes of the drillstring. The inclination of the “Bottom Node (N.I.)” line is close to the Top Node curve, which means that the rotational velocity at top and bottom is almost the same for the case without torsional inertia considered. The “Bottom Node (I)” curve is the response of the drillstring to the torsional inertia. It shows that it is necessary more steps to achieve the same inclination of the Top Node line, i.e., more steps to propagate the rotation imposed at the top.

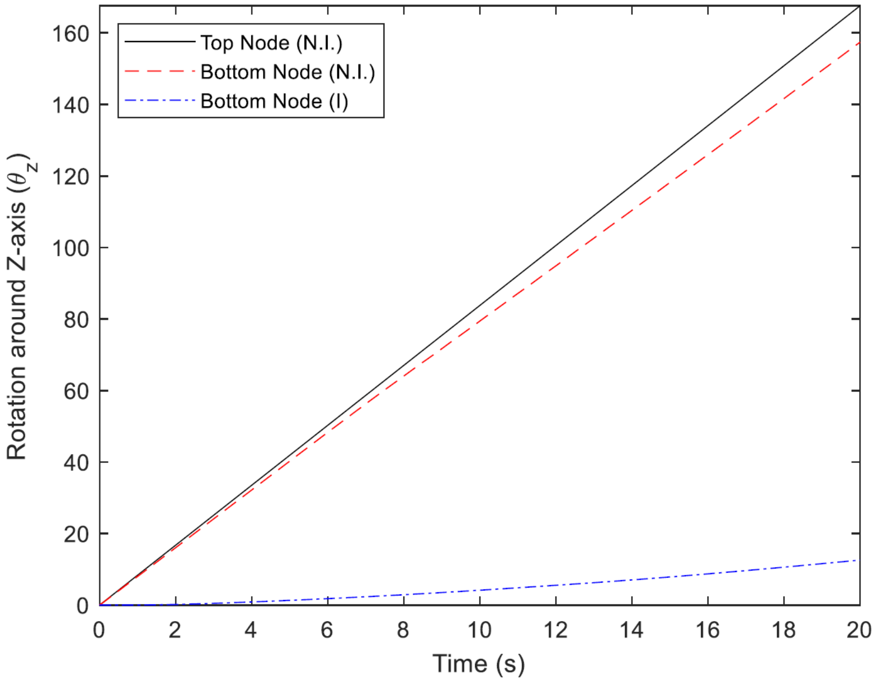

Figure 42 - Rotation of top and bottom nodes. N.I. = No Inertia; I = With Inertia (θ_z in rad).

Figure 43 and Figure 44 illustrate the radial displacement of a point on the drill collar (7,4 m above the bit) for different WOB, with and without torsional inertia, respectively. For all loading cases, the drillstring starts the rotation buckled into a 2D or sinusoidal shape. The displacements presented in the Figure 43 and Figure 44 represent the beginning of the 3D shape mode. This change of shape happens faster as the rotary speed increases. Figure 44 also shows that the imposed rotary speed arrives at the end of the column, which causes the vibrations.

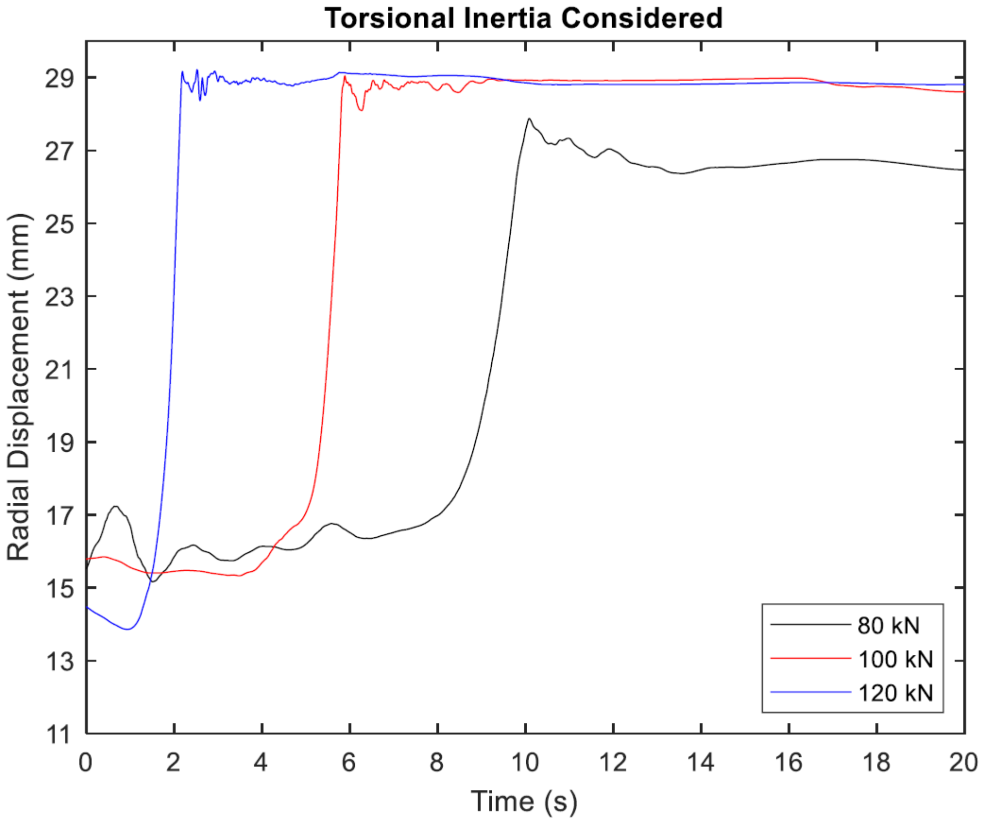

Figure 43 - Radial displacement of DC node 7,4m above bit, considering torsional inertia.

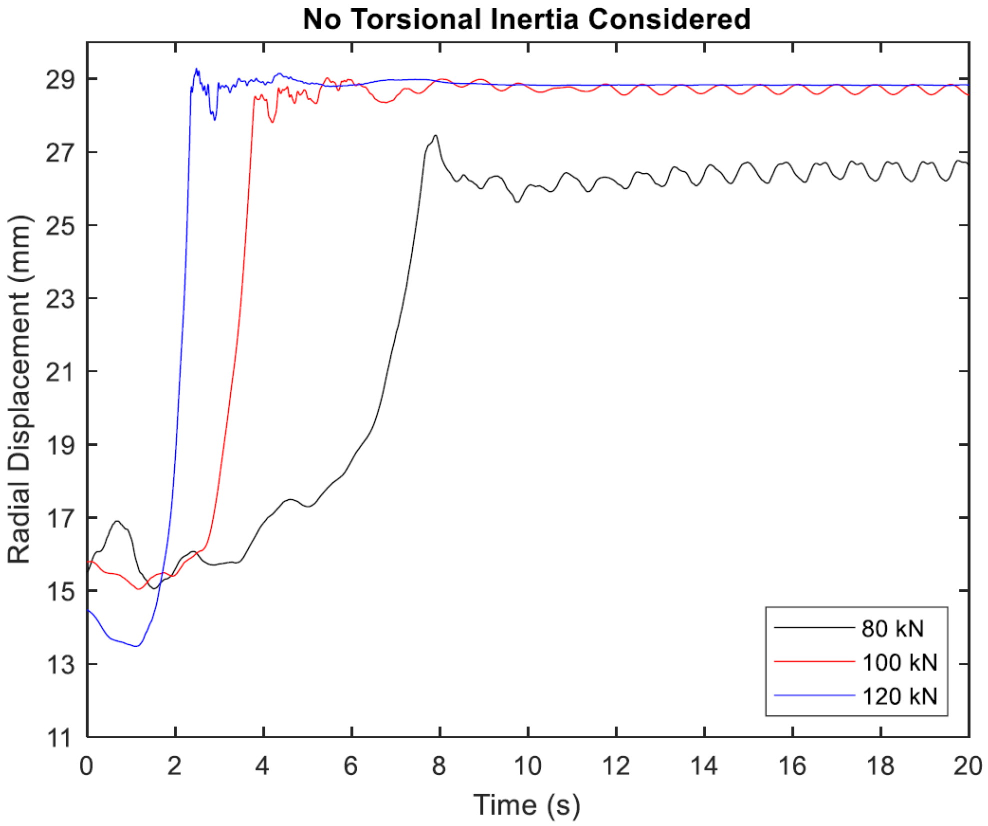

Figure 44 - Radial displacement of DC node 7,4m above bit, without torsional inertia.

Figure 45 depicts the axial force of the drillstring at the end of the static analysis (step 150) and when the force achieves the desired value of 80 kN (step 1760) and the column starts rotating. Since there is no imposed vibration between the rock and the bit, the weight on the bit does not fluctuate, as demonstrated in the figure. Figure 45 also shows the neutral point, which is 92.0 m far from the bit.

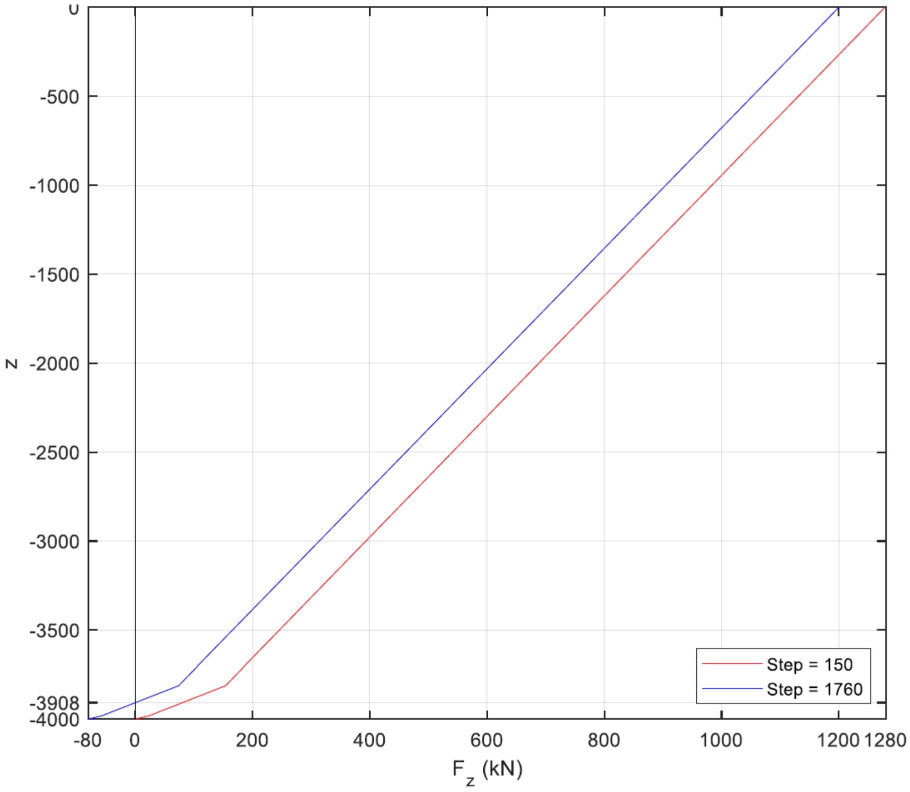

Figure 45 - Axial force through the column.

Figure 46 illustrates the radial displacement of the column in 5 seconds, and the lateral displacement of some points of the drillstring in the entire process (static + dynamic). For a load equal to 80 kN, the HWDP and DC suffer significant lateral displacement, presenting a 3D buckling shape.

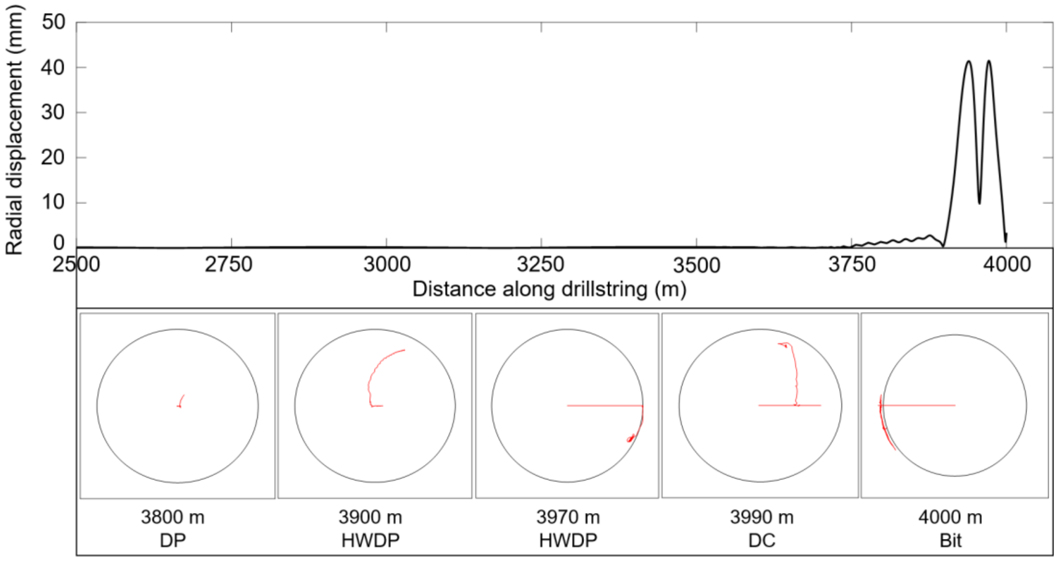

Figure 46 - Lateral displacement of the drillstring.

6.5.1.
Effect of WOB

Figure 47 shows the buckling modes for different loads in 5 seconds of rotation.

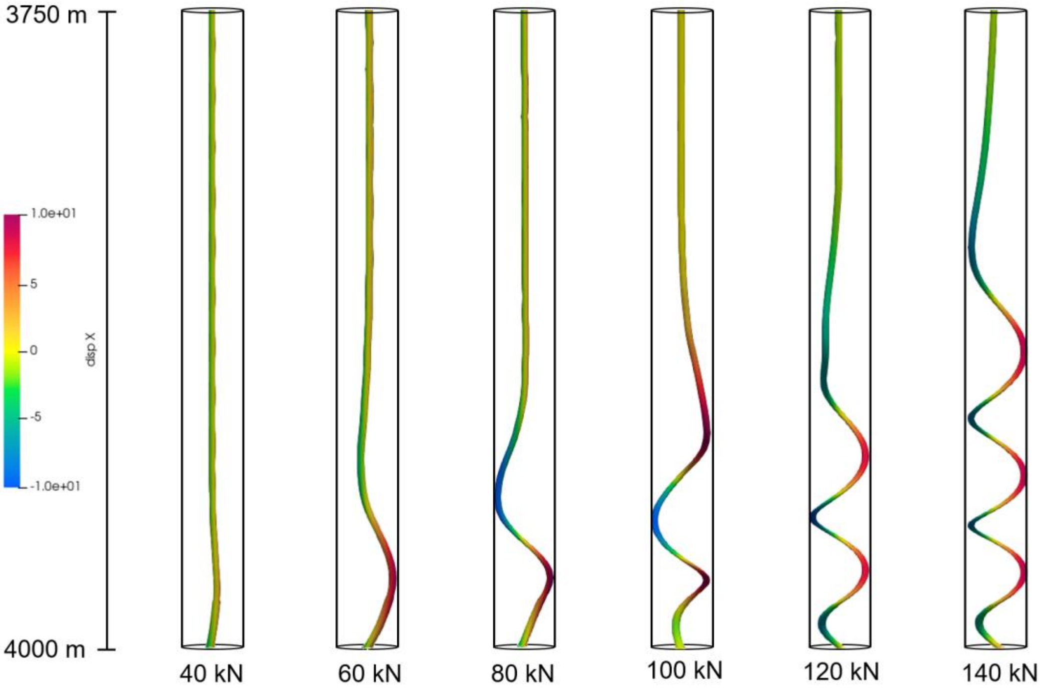

Figure 47 - Drillstring radial shapes for different WOB (3750-4000m).

Figure 48 presents the top view of the drillstring for different instantaneous time for $WOB = 80\ kN$. At the beginning of rotation, the column is buckled laterally. With the advance of time, it buckles in a 3D shape and continuously contact the borehole wall.

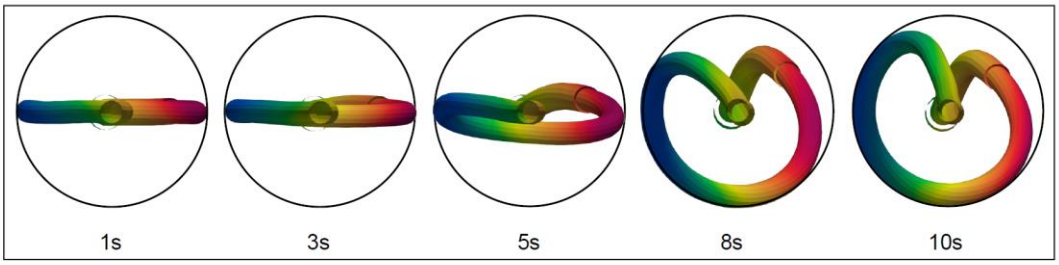

Figure 48 - Top view of the drillstring shape for different instantaneous time.

6.5.2.

Effect of Stabilizers

This work also studied the effect of stabilizers on the drillstring behavior. Figure 49 depicts the displacement of the lower 350 m drill column, using one stabilizer singly at different positions (15 m, 30 m, and 45 m above the bit), in 5s of analysis from the beginning of the rotation. The results show different points of buckling, which may not be the best use of the stabilizers. On the other hand, Figure 50 illustrates the drillstring displacement using stabilizers in all three positions. As expected, the column remains centralized, generating small displacements.

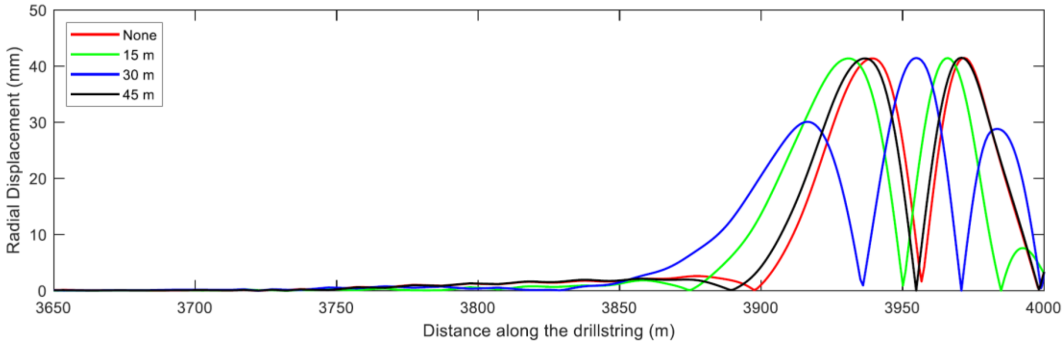

Figure 49 - Drillstring displacement for different stabilizer positions.

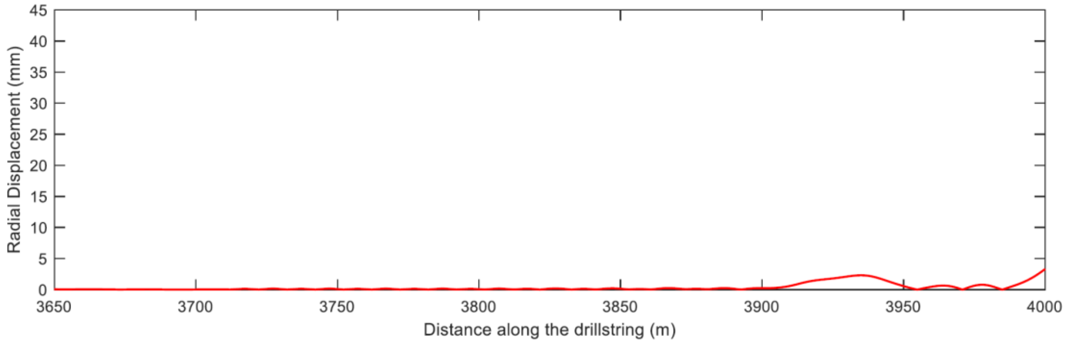

Figure 50 - Drillstring displacement considering all the three stabilizers.

6.5.3.
Effect of rotary speed

The comparison of the bending moment of the drill collar element 7,4 m above the bit for different rotary speeds (Figure 51) shows that the moment oscillates with the same frequency of the rotary speed. Besides, raising the rotary speed does not affect the bending moment amplitude, and consequently, the stress amplitude in the element. However, the higher the speed, the higher the frequencies, which impacts the number of stress cycles occurring in the structure, resulting in less lifetime.

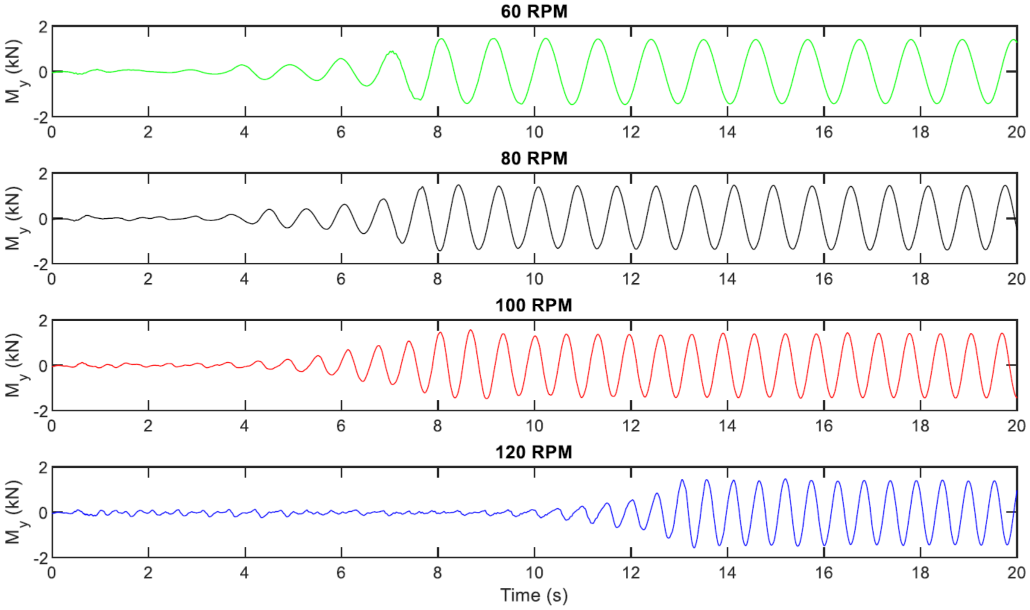

Figure 51 - Moment around y-axis for different RPM.

7.
Concluding Remarks

The present work focused on developing a finite element program capable of analyzing the nonlinear dynamic behavior of a drillstring, taking into account the contact borehole wall/drillstring. The main developments of this work can be summarized as:

- Presentation of an overview about the rotary drilling and its components, deepening into the drillstring elements and functions;
- Development of the finite element formulation, using the corotational formulation for considering large displacements and rotations;
- Discretization of the drillstring into the beam element with six degrees of freedom per node, employing the Euler-Bernoulli's beam formulation;
- Development of an algorithm using the MATLAB [58] software, utilizing the Newton-Raphson method for solving the nonlinear systems of equations. Use of Newmark's method for the time integration of the problem's movement equations;
- Development of linear setup spring model for representing the contact between the borehole wall and the column;
- Test of the formulation by comparing results to the ones in literature;
- Development of examples of drillstring under compression, analyzing the buckling behavior.

Examples 6.1 to 6.3 correspond to standard problems used in the literature to validate the large displacements and rotations formulation. These examples' results showed good agreement with the ones in the literature and with analytical solutions.

Example 6.4 emphasized the relevance of the boundary condition's application and the geometric imperfection applied to the structure. Since the column is a very complex and slender structure, any variation on initial parameters may result in different buckling behavior and critical buckling loads. Also, the example presented the expected behavior of a compressed drillstring, confined in a wellbore, with these specific boundary conditions. The column first displaced laterally, then into a 2D buckling mode, and as the compressing force increased, it continuously contacted the wellbore until it became a 3D helicoidal buckling mode. As the example demonstrated, some of these buckling steps may be different depending on the initial conditions.

Example 6.5 presented the complexity of a much longer drillstring. As the length increases, the slenderness increases, and so does the difficulty of the analysis. Besides, removing the torsional inertia made the analysis faster, and it was feasible for this case since there was no friction and imposed vibration applied. Increasing the WOB affected the performance of the column due to the raising of buckling, as shown in 6.5.1. With the advance of time, a column initially buckled into a 2D shape will achieve a 3D shape for a fixed WOB. A solution to prevent buckling and keep the column straight in the center of the well was to employ stabilizers. However, the positioning of the stabilizer should be further studied for achieving better performance. Furthermore, increasing the rotary speed leads to higher frequencies and number of stress cycles in the structure, decreasing the lifetime.

7.1.

Conclusion and Suggestions for Future Works

The drillstring is the main element of the rotary system, and a bad performance could cause damage to its components and to the wellbore, which leads to huge costs.

Since the analysis of the entire elastic drillstring, considering drill pipes and drill collars, is not a common study in the literature, this work contributes furnishing a starting point for further development of a more complex model of the integrated system, including:

- The treatment of large rotations: in this work, the incremental rotations are summed algebraically, what accumulates error if used high values of time increments, and leads to premature divergence;
- Nonlinear wellbore/drillstring contact;
- Drillstring/mudflow interaction;
- Rock/bit interaction;
- Study of vibrations;
- Study of drillstring fatigue and lifetime.

8.
References

[1] Thomas, J. E. (2001). Fundamentos de engenharia de petróleo. Interciência.

[2] Jansen, J. D (1993). Nonlinear dynamics of oilwell drillstrings. Ph.D Thesis, TU Delft, Amsterdam.

[3] Dareing, D. W. (2012). Mechanics of Drillstrings and Marine Risers. ASME Press.

[4] Mitchell, R. F.; Miska, Z. S. (2011). Fundamentals of drilling engineering. Society of Petroleum Engineers

[5] Dong, G., & Chen, P. (2016). A Review of the Evaluation, Control, and Application Technologies for Drill String Vibrations and Shocks in Oil and Gas Well. Shock and Vibration, 2016, 7418635. https://doi.org/10.1155/2016/7418635

[6] Aguiar, L. L. (2013). A Three-Dimensional Pipe Beam Finite Element for Nonlinear Analysis of Multilayered Risers and Pipelines. Rio de Janeiro. 124p. D.Sc. Thesis – Departamento de Engenharia Mecânica, Pontifícia Universidade Católica do Rio de Janeiro.

[7] Mourelle, M. M. (1993). Análise Dinâmica de Sistemas Estruturais Constituídos por Linhas Marítimas. Rio de Janeiro. 305 p. D.Sc. Thesis – COPPE, Universidade Federal do Rio de Janeiro.

[8] Rangel, R. L. (2019). Educational Tool for Structural Analysis of Frame Models with Geometric Nonlinearity. Rio de Janeiro. 201 p. M.Sc. Dissertation – Departamento de Engenharia Civil, Pontifícia Universidade Católica do Rio de Janeiro.

[9] Hossain, M. E. (2017). Fundamentals of Drilling Engineering: Multiple Choice Questions and Workout Examples for Beginners and Engineers. John Wiley & Sons, Incorporated.

[10] Britannica, E. (2017). Drilling mud. https://www.britannica.com/technology/drilling-mud

[11] Cunha, A. B. (2015). Modeling and uncertainty quantification in the nonlinear stochastic dynamics of a horizontal drillstrings. D.Sc. Thesis, Pontifícia Universidade Católica do Rio de Janeiro/Université Paris-Est

[12] Devereux, S. (2012). Drilling Technology in Nontechnical Language.

PennWell Corporation.

[13] Bourgoyne, A. T. (1986). Applied Drilling Engineering (J. F. Evers & D. S. Pye (eds.); Second). Society of Petroleum Engineers.

[14] Guo, B. and Liu, G. (2011). Applied Drilling Circulation Systems: Hydraulics, Calculations and Models. Elsevier Science.

[15] Slumberger. (2012). The Defining Series: Well Cementing Fundamentals. Oilfield Review. https://www.slb.com/resource-library/oilfield-review/defining-series/defining-cementing

[16] Márquez, M. B. S., Boussaada, I., Mounier, H., & Niculescu, S. I. (2016). Analysis and Control of Oilwell Drilling Vibrations: A Time-Delay Systems Approach. Springer International Publishing.

[17] Rocha, L. A. S., Azuaga, D., Andrade, R., Vieira, J. L. B., & Santos, O. L. A. (2008). Perfuração direcional. Interciência.

[18] Drilling Course (2016). Naturel Diamonds Drilling Bits. https://www.drillingcourse.com/2016/01/naturel-diamonds-drilling-bits.html

[19] Drilling Course (2015). Introduction to Drilling Bits. https://www.drillingcourse.com/2015/12/introduction-to-drilling-bits.html

[20] Ghasemloonia, A., Geoff Rideout, D., & Butt, S. D. (2015). A review of drillstring vibration modeling and suppression methods. Journal of Petroleum Science and Engineering, 131, 150–164. https://doi.org/10.1016/j.petrol.2015.04.030

[21] Jardine, S., Malone, D., & Sheppard, M. (1994). Putting a damper on drilling’s bad vibrations. Oilfield Review; (Netherlands), 6(1).

[22] Liu, Y., Lin, W., Páez Chávez, J., & De Sa, R. (2019). Torsional stick-slip vibrations and multistability in drill-strings. Applied Mathematical Modelling, 76, 545–557. https://doi.org/10.1016/j.apm.2019.06.012

[23] Dunayevsky, V. A., Abbassian, F., & Judzis, A. (1993). Dynamic Stability of Drillstrings Under Fluctuating Weight on Bit. SPE Drilling & Completion, 8(02), 84–92. https://doi.org/10.2118/14329-PA

[24] Ritto, T. G. (2010). Numerical Analysis of the Nonlinear Dynamics of a Drill-string with Uncertainty Modeling. D.Sc. Thesis, Pontifícia Universidade Católica do Rio de Janeiro.

[25] Aguiar, R. R. (2010). Experimental investigation and numerical analysis of the vibro-impact phenomenon. D.Sc. Thesis, Pontifícia Universidade

Católica do Rio de Janeiro.

[26] Kriesels, P. C., Keultjes, W. J. G., Dumont, P., Huneidi, I., Owoeye, O. O., & Hartmann, R. A. (1999). Cost Savings through an Integrated Approach to Drillstring Vibration Control. 1–12. https://doi.org/10.2118/57555-ms

[27] Chen, S. L., Blackwood, K., & Lamine, E. (2002). Field Investigation of the Effects of Stick-Slip, Lateral, and Whirl Vibrations on Roller-Cone Bit Performance. SPE Drilling & Completion, 17(01), 15–20. https://doi.org/10.2118/76811-PA

[28] Sun, Y.-X., Qiao, L.-H., Sun, H.-F., Han, L.-X., & Zhang, G. (2016). Real-time Surveillance System of Mechanical Specific Energy Applied in Drilling Parameters Optimization. Proceedings of the 2nd Annual International Conference on Advanced Material Engineering (AME 2016), 771–777. https://doi.org/10.2991/ame-16.2016.128

[29] Khulief, Y. A., & Al-Naser, H. (2005). Finite element dynamic analysis of drillstrings. Finite Elements in Analysis and Design, 41(13), 1270–1288. https://doi.org/10.1016/j.finel.2005.02.003

[30] Millheim, K., Jordan, S., & Ritter, C. J. (1978). Bottom-Hole Assembly Analysis Using the Finite-Element Method. *Journal of Petroleum Technology*, 30(02), 265–274. doi: https://doi.org/10.2118/6057-PA

[31] Feng, T., Vadali, M., Ma, Z., Chen, D., & Dykstra, J. (2017). A Finite Element Method With Full Bit-Force Modeling to Analyze Drillstring Vibration. *Journal of Dynamic Systems, Measurement, and Control*, *139*(9). https://doi.org/10.1115/1.4036083

[32] Moaveni, S. (2015). Finite Element Analysis: Theory and Application with ANSYS (4th ed.). Pearson Education.

[33] Spanos, P. D., Payne, M. L., & Secora, C. K. (1997). Bottom-Hole Assembly Modeling and Dynamic Response Determination. *Journal of Energy Resources Technology*, *119*(3), 153–158. https://doi.org/10.1115/1.2794983

[34] Zare, J., Hashemi, S. J., & Rashed, G. (2011). Finite Element Analysis of Drillstring Lateral Vibration. *Journal of Engineering and Applied Sciences*, 6:64–70. https://doi.org/10.3923/jeasci.2011.64.70

[35] Ghasemloonia, A., Geoff Rideout, D., & Butt, S. D. (2013). Vibration Analysis of a Drillstring in Vibration-Assisted Rotary Drilling: Finite Element Modeling With Analytical Validation. *Journal of Energy Resources*

Technology, *135*(3). https://doi.org/10.1115/1.4023333

[36] Bathe, K. J., Finite Element Procedures, New Jersey, Prentice-Hall, 1996.

[37] Crisfield, M. A. (1990). A consistent co-rotational formulation for non-linear, three-dimensional, beam-elements. *Computer Methods in Applied Mechanics and Engineering*, *81*(2), 131–150. https://doi.org/10.1016/0045-7825(90)90106-V

[38] Bathe, K.-J., & Bolourchi, S. (1979). Large displacement analysis of three-dimensional beam structures. *International Journal for Numerical Methods in Engineering*, 14(7), 961–986. https://doi.org/10.1002/nme.1620140703

[39] Soriano, H. L. (2014). *Introdução À Dinâmica Das Estruturas*. ELSEVIER EDITORA.

[40] Salies, J. B., Cunha, J. C. S., Azar, J. J., & Soren J.R., J. (1994). Experimental and Analytical Study of Sinusoidal Buckling in Vertical Wells. All Days. https://doi.org/10.2118/29164-MS

[41] Menand, S., Sellami, H., Tijani, M., & Akowanou, J. (2006). Buckling of Tubulars in Actual Field Conditions. All Days. https://doi.org/10.2118/102850-MS

[42] Hajianmaleki, M., Daily, J. S., Ring, L., & Gandikota, R. (2013). Critical Buckling Load Assessment of Drill Strings In Different Wellbores Using The Explicit Finite Element Method. *All Days*. https://doi.org/10.2118/166592-MS

[43] Lubinski, A. (1950). A Study on the Buckling of Rotary Strings. API Drilling Production Practice, pp. 178-214.

[44] Huang, W., Gao, D., & Liu, Y. (2016). A study of tubular string buckling in vertical wells. International Journal of Mechanical Sciences, 118, 231–253. https://doi.org/10.1016/j.ijmecsci.2016.09.035

[45] Xie, J. (2018). Finite Element Analysis of Tubing Buckling in Oil Wells. Science in the Age of Experience. Boston, USA.

[46] Chen, X., Yang, J., & Gao, D. (2018). Drilling Performance Optimization Based on Mechanical Specific Energy Technologies. In A. Samsuri (Ed.), Drilling. IntechOpen. https://doi.org/10.5772/intechopen.75827

[47] Albino, J. C. R. (2011). Materiais com Gradação Funcional no Comportamento Dinâmico de Linhas Flexíveis. Rio de Janeiro. D.Sc. Thesis – Departamento de Engenharia Mecânica, Pontifícia Universidade Católica

do Rio de Janeiro. https://doi.org/10.17771/PUCRio.acad.19447

[48] Timoshenko, S. P., Gere, J. (1964). *Theory of Elastic Stability* (2nd ed.). McGraw-Hill.

[49] Nunes, C. C., Soriano, H. L., & filho, F. V. (2003). Geometric non-linear analysis of space frame with rotation greater than 90°, with Euler angles and quasi-fixed local axes system. International Journal of Non-Linear Mechanics, 38(8), 1195–1204. https://doi.org/10.1016/S0020-7462(02)00064-1

[50] Wu, J. (1992). Buckling Behavior of Pipes in Directional and Horizontal Wells. Ph.D. Dissertation, Texas A & M University. pp 439-440.

[51] Lubinski, A., Althouse, W. S. (1962). Helical Buckling of Tubing Sealed in Packers. J Pet Technol;14(6):655–70.

[52] Novoselac, S., Ergic, T., & Balicevic, P. (2012). Linear and nonlinear buckling and post buckling analysis of a bar with the influence of imperfection. *Tehnicki Vjesnik*, *19*, 695–701.

[53] Souza, D. A. (2005). Análise Numérica de Colunas com Seções Enrijecidas e Não-Enrijecidas em Perfis Formados a Frio. Ouro Preto. 97f. M.Sc. Dissertation – Departamento de Engenharia Civil, Universidade Federal de Ouro Preto.

[54] Zhu, X., & Li, B. (2019). Numerical simulation of dynamic buckling response considering lateral vibration behaviors in drillstring. Journal of Petroleum Science and Engineering, 173, 770–780. https://doi.org/10.1016/j.petrol.2018.09.090

[55] Shuguang Huayang Drilling Tool Co. (2020), accessed 08 December 2020, <http://en.shuguanggroup.com>

[56] Alibaba (2020), accessed 08 December 2020, <https://www.alibaba.com/product-detail/Water-well-drilling-tool-three-blade_62018851904.html?spm=a2700.galleryofferlist.normal_offer.d_image.1b81687aMqzNHN>

[57] Linkers India (2020), accessed 08 December 2020, <http://linkersindia.net/milled-tooth-drill-bits.html>

[58] The MathWorks Inc. (2020). MATLAB version 9.8.0 (R2020a) [Computer Software]. Natick, Massachusetts. https://www.mathworks.com/products/matlab.html

[59] Dassault Systèmes Simulia Corp. (2021). Abaqus [Computer Software]. Providence, Rhode Island. https://www.ska.com.br/produtos/simulia-abaqus

[60] Liu, W., & Gao, D. (2021). Study on the anti-wear performance of diamond impregnated drill bits. *International Journal of Refractory Metals and Hard Materials*, *99*, 105577. https://doi.org/10.1016/j.ijrmhm.2021.105577

[61] Machado, L. R. (2016). Flambagem de Tubos de Revestimento de Superfície. Rio de Janeiro. 109p. Dissertação de Mestrado - Departamento de Engenharia Mecânica, Pontifícia Universidade Católica do Rio de Janeiro.

[62] Cebeci, M., Gücüyener, ismail H., & Kök, M. V. (2019). *Analysis of Sinusoidal Buckling of Drill String in Vertical Wells Using Finite Element Method*. *Day 3 Wed*, *March 20, 2019*. https://doi.org/10.2118/194974-MS

Appendix A:
Cantilever Beam Under Point Load

In this section, the steps from the numerical formulation described in item 4.7 are exemplified for a single-element cantilever beam under static point load at its end. The analysis was performed with one step, and requires three iterations to converge. The example presents the element update and transformation matrices, relative displacements, forces, and the displacements for all iterations.

A.1.
Problem Description

Figure A.1 illustrates the geometry of the problem and presents the parameters used in the analysis.

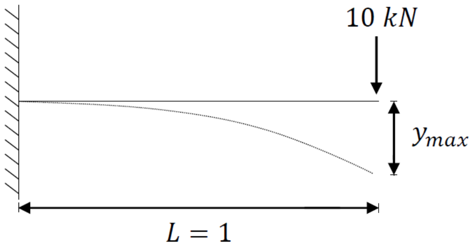

$E = 4\pi \times 10^7\ Pa$

$v = 0.3$

$A = 0.25\ m^2$

$I = 0.004974\ m^4$

$\rho = 100\ kg/m^3$

$\varepsilon_{disp} = 10^{-4}$

$\varepsilon_{res} = 10^{-2}$

Figure A.1 - Cantilever beam under point load example.

The variables ε_{disp} and ε_{res} are the displacements and residual tolerances for the convergence analysis.

A.2.

Iteration 1

The first iteration corresponds to the results of linear analysis. Therefore, the displacement and slope of the tip (u_9^1 and u_{11}^1) is evaluated by the following equations:

$$u_9^1 = -\frac{PL^3}{3EI} = \frac{10^4 \times 1^3}{3 \times 1.25 \times 10^8 \times 0.005} = -0.0053 = y_{max} \tag{A.1}$$

$$u_{11}^1 = \frac{PL^2}{2EI} = \frac{10^4 \times 1^2}{2 \times 1.25 \times 10^8 \times 0.005} = 0.0080 \tag{A.2}$$

Since the initial displacements are null in the first iteration, there is no increment to nodal coordinates. Consequently, the rotation matrices are the identity matrix, and the relative displacements and rotations are null, resulting in no internal forces. Therefore, these matrices and vectors are presented for the next iteration. Since there are no internal forces, the geometric stiffness matrix is null, and only the linear stiffness matrix is calculated. For the same reason, the residual force vector is equal to the prescribed force vector. Because the structure has only one element, the local system's stiffness matrices and forces vector are the same as the global system.

The residual force vector and stiffness matrix are:

$$\boldsymbol{R}_F = [0 \quad 0 \quad 0 \quad 0 \quad 0 \quad 0 \quad 0 \quad 0 \quad -10000 \quad 0 \quad 0 \quad 0]^T$$

$$K_L = 10^7 \begin{bmatrix} 3.1416 & 0 & 0 & 0 & 0 & 0 & -3.1415 & 0 & 0 & 0 & 0 & 0 \\ 0 & 0.750 & 0 & 0 & 0 & 0.375 & 0 & -0.750 & 0 & -0 & 0 & 0.375 \\ 0 & 0 & 0.750 & 0 & -0.375 & 0 & 0 & 0 & -0.750 & 0 & -0.375 & 0 \\ 0 & 0 & 0 & 0.0481 & 0 & 0 & 0 & 0 & 0 & -0.0481 & 0 & 0 \\ 0 & 0 & -0.375 & 0 & 0.250 & 0 & 0 & 0 & 0.375 & 0 & 0.125 & 0 \\ 0 & 0.375 & 0 & 0 & 0 & 0.250 & 0 & -0.375 & 0 & 0 & 0 & 0.125 \\ -3.1416 & 0 & 0 & 0 & 0 & 0 & 3.1416 & 0 & 0 & 0 & 0 & 0 \\ 0 & -0.750 & 0 & 0 & 0 & -0.375 & 0 & 0.750 & 0 & 0 & 0 & -0.375 \\ 0 & 0 & -0.750 & 0 & 0.375 & 0 & 0 & 0 & 0.750 & 0 & 0.375 & 0 \\ 0 & 0 & 0 & -0.0481 & 0 & 0 & 0 & 0 & 0 & 0.0481 & 0 & 0 \\ 0 & 0 & -0.375 & 0 & 0.125 & 0 & 0 & 0 & 0.375 & 0 & 0.250 & 0 \\ 0 & 0.375 & 0 & 0 & 0 & 0.125 & 0 & -0.375 & 0 & 0 & 0 & 0.250 \end{bmatrix}$$

The result of the linear system $\boldsymbol{K}_t^1 \Delta \boldsymbol{u}^1 = \boldsymbol{R}_F^1$ $(\boldsymbol{K}_t^1 = \boldsymbol{K}_L)$ gives:

$$\Delta \boldsymbol{u}^1 = [0 \quad 0 \quad 0 \quad 0 \quad 0 \quad 0 \quad 0 \quad 0 \quad -0.0053 \quad 0 \quad 0.0080 \quad 0]^T$$

Convergence criteria:

$$min\left(\; \|{}^{1}\boldsymbol{\Delta u}^{1}\| \quad , \; \frac{\|{}^{1}\boldsymbol{\Delta u}^{1}\|}{\|{}^{1}\boldsymbol{\Delta U}^{1}\|} \right) \leq \varepsilon_{disp}, \text{ where } \Delta\boldsymbol{U}^{1} = \Delta\boldsymbol{u}^{1} + \Delta\boldsymbol{u}^{0}$$

$$min(\quad 0.0096 \quad , \quad 1 \quad) > 10^{-4}$$

$$min\left(\; \left\|{}^{1}\boldsymbol{R}_{F}{}^{1}\right\| \quad , \; \frac{\left\|{}^{1}\boldsymbol{R}_{F}{}^{1}\right\|}{\left\|{}^{1}\boldsymbol{R}_{F}{}^{1}\right\|} \right) \leq \varepsilon_{res}$$

$$min(\quad 10000 \quad , \quad 1 \quad) > 10^{-2}$$

A.3.
Iteration 2

A.3.1.
Element Update Procedure

The initial step is to increment the nodal displacements, calculate the direction cosine, and the deformed length using the incremental displacements from the last iteration. Because the last iteration generated displacement just in the third degree of freedom (DOF) of the second node, only this DOF must be updated:

$$n_{2_z} = n_{2_z} + \Delta u_9 = 0 - 0.0053 = -0.0053$$

$$L_{def} = \left\| n_{2_x} - n_{1_x}, n_{2_y} - n_{1_y}, n_{2_z} - n_{1_z} \right\| \approx 1$$

$$CosDir = \left\| n_{2_x} - n_{1_x}, n_{2_y} - n_{1_y}, n_{2_z} - n_{1_z} \right\| / L_{def}$$

$$CosDir = [1.00 \quad 0.00 \quad -0.0053]$$

where n_{2_z} is the degree of freedom z of the second node.

A.3.2.
Calculate internal forces

A.3.2.1.
Calculate Transformation Matrices

- **Nodal incremental rotation matrices ($\boldsymbol{R}_{inc}$)**

The matrices are calculated using the Rodrigues'rotation formula, with the angles from the incremental displacements. Since there is rotation only about y-axis in the second node, the $\boldsymbol{R}^2_{inc_1}$ is the identity matrix, and the $\boldsymbol{R}^2_{inc_2}$ is given by:

$$\boldsymbol{R}^2_{inc_2} = \begin{bmatrix} 1 & 0 & 0.0080 \\ 0 & 1 & 0 \\ -0.0080 & 0 & 1 \end{bmatrix}$$

- **Nodal rotation matrices ($\boldsymbol{R}_n$)**

These matrices are calculated from the rotation increments. Because the nodal incremental rotation matrix from node 1 is the identity, $\boldsymbol{R}_{n_1}$ is also the identity, and matrix $\boldsymbol{R}_{n_2}$ is calculated as:

$$\boldsymbol{R}^2_{n_2} = \begin{bmatrix} 1 & 0 & 0.0080 \\ 0 & 1 & 0 \\ -0.0080 & 0 & 1 \end{bmatrix}$$

- **Element rotation matrix**

The element rotation matrix in the second iteration is expressed as:

$$\boldsymbol{R}^2_e = [\boldsymbol{X} \quad \boldsymbol{Y} \quad \boldsymbol{Z}]^T$$

where:

$\boldsymbol{X} = [1.00 \quad 0.00 \quad -0.0053]$ (vector holding the direction cosines)

$$\mathbf{Y} \ = \ \frac{\boldsymbol{R}^2_{n_1}(\text{2nd row}) + \boldsymbol{R}^2_{n_2}(\text{2nd row})}{2} = [0 \quad 1 \quad 0]$$

$$\mathbf{Z} = \mathbf{X} \times \mathbf{Y} = [0.0053 \quad 0.00 \quad 1.00]$$

Correcting $\boldsymbol{Y}$:

$$\mathbf{Y} = \mathbf{Z} \times \mathbf{X} = [0 \quad 1 \quad 0]$$

$$\boldsymbol{R}^2_e = \begin{bmatrix} 1.00 & 0.00 & -0.0053 \\ 0 & 1 & 0 \\ 0.0053 & 0.00 & 1.00 \end{bmatrix}$$

A.3.2.2.

Calculate nodal relative rotations

The relative nodal rotations are calculated employing the Crisfield formulation, using the nodal and element rotation matrices. Therefore, the relative rotations are:

$$\Delta\theta_1 = [0.00 \quad -0.0053 \quad 0]$$

$$\Delta\theta_2 = [0.00 \quad 0.0027 \quad 0]$$

A.3.2.3.

Calculate vector of relative displacements $(\boldsymbol{d_r})$

The vector of relative displacements is composed of the relative rotations and the total increment length, calculated as:

$$L_{inc} = L_{def} - L = 1.422 \times 10^{-5} \approx 0$$

$$\boldsymbol{u}_r^2 = [0 \quad 0 \quad 0 \quad 0 \quad -0.0053 \quad 0 \quad 1.422 \times 10^{-5} \quad 0 \quad 0 \quad 0 \quad 0.0027 \quad 0]^T$$

A.3.2.4.

Calculate internal forces

The internal force vector in the natural system is calculated as:

$$\boldsymbol{f}_{int}^2 = \boldsymbol{K}_L^{(m)}\, \boldsymbol{u}_r^2$$

$$\boldsymbol{f}_{int}^2 = [-446.80 \quad 0 \quad 9999.6 \quad 0 \quad -9999.8 \quad 0 \quad 446.80 \quad 0 \quad -9999.6 \quad 0 \quad 0.1896 \quad 0]^T$$

Transforming from natural to global system:

$$\boldsymbol{f}_G^2 = [-393.46 \quad 0 \quad 10002 \quad 0 \quad -9999.8 \quad 0 \quad 393.46 \quad 0 \quad -10002 \quad 0 \quad 0.1896 \quad 0]^T$$

Because there is only one element, the global internal force vector is equal to the local internal force vector referred to the global system:

$$\boldsymbol{F}_{int}^2 = \boldsymbol{f}_G^2$$

A.3.3.

Calculate tangent stiffness matrix

The tangent stiffness matrix is the sum of the linear and geometric stiffness matrices. The geometric matrix is given by:

$$K_G^2 = \begin{bmatrix} 446.80 & 0 & 0 & 0 & 9999.81 & 0 & -446.80 & 0 & 0 & 0 & -9999.81 & 0 \\ & 642.83 & 0 & -9999.81 & 0 & 98.01 & 0 & -642.83 & 0 & 9999.81 & 0 & 98.01 \\ & & 642.83 & 0 & -98.01 & 0 & 0 & 0 & -642.83 & 0 & -98.01 & 0 \\ & & & 17.78 & 0 & 1666.60 & 0 & 9999.81 & 0 & -17.78 & 0 & -1666.60 \\ & & & & 95.13 & 0 & -9999.81 & 0 & 98.01 & 0 & 2.88 & 0 \\ & & & & & 95.13 & 0 & -98.01 & 0 & -1666.60 & 0 & 2.88 \\ & & & & & & 446.80 & 0 & 0 & 0 & 9999.81 & 0 \\ & & & & & & & 642.83 & 0 & -9999.81 & 0 & -98.01 \\ & & & & & & & & 642.83 & 0 & 98.01 & 0 \\ & & & & & & & & & 17.77 & 0 & 1666.60 \\ & & & & & & & & & & 95.13 & 0 \\ & & & & & & & & & & & 95.13 \end{bmatrix}$$

$$K_t^2(1:6) = \begin{bmatrix} 3.1416 & 0 & 0 & 0 & 9.9998 \times 10^{-4} & 0 \\ & 0.75006 & 0 & -9.9998 \times 10^{-4} & 0 & 0.37501 \\ & & 0.75006 & 0 & -0.37501 & 0 \\ & & & 4.8102 \times 10^{-2} & 0 & 1.6666 \times 10^{-4} \\ & & & & 0.25001 & 0 \\ & & & & & 0.25001 \\ & & & & & \\ & & & & & \\ & & & & & \\ & & & & & \\ & & & & & \\ & & & & & \end{bmatrix}$$

$$K_t^2(7:12) = \begin{bmatrix} -3.1415 & 0 & 0 & 0 & -9.9998 \times 10^{-4} & 0 \\ 0 & -0.75006 & 0 & 9.9998 \times 10^{-4} & 0 & 0.37501 \\ 0 & 0 & -0.75006 & 0 & -0.37501 & 0 \\ 0 & 9.9998 \times 10^{-4} & 0 & -4.8102 \times 10^{-2} & 0 & -1.6666 \times 10^{-4} \\ -9.9998 \times 10^{-4} & 0 & 0.37501 & 0 & 0.125 & 0 \\ 0 & -0.37501 & 0 & -1.6666 \times 10^{-4} & 0 & 0.125 \\ 3.1416 & 0 & 0 & 0 & 9.9998 \times 10^{-4} & 0 \\ & 0.75006 & 0 & -9.9998 \times 10^{-4} & 0 & -0.37501 \\ & & 0.75006 & 0 & 0.37501 & 0 \\ & & & 4.8102 \times 10^{-2} & 0 & 1.6666 \times 10^{-4} \\ & & & & 0.25001 & 0 \\ & & & & & 0.25001 \end{bmatrix}$$

A.3.4.

Calculate vector of residual forces and solve linear system

$$\boldsymbol{R}_F^2 = [393.46 \quad 0 \quad -10002 \quad 0 \quad 9999.8 \quad 0 \quad -393.46 \quad 0 \quad 1.86 \quad 0 \quad -0.1896 \quad 0]^T$$

$$\boldsymbol{K}_t^2 \Delta \boldsymbol{u}^2 = \boldsymbol{R}_F^2$$

$$\Delta \boldsymbol{u}^2 = [0 \quad 0 \quad 0 \quad 0 \quad 0 \quad 0 \quad -1.25 \times 10^{-5} \quad 0 \quad -8.09 \times 10^{-9} \quad 0 \quad 8.66 \times 10^{-8} \quad 0]^T$$

A.3.5.

Calculate convergence criterions

$$min\left(\quad \|{}^1\boldsymbol{\Delta u}^2\| \quad , \quad \frac{\|{}^1\boldsymbol{\Delta u}^2\|}{\|{}^1\boldsymbol{\Delta U}^2\|} \quad \right) \leq \varepsilon_{disp}$$

$$min(\quad 1.25 \times 10^{-5} \quad , \quad 0.0013 \quad) < 10^{-4}$$

$$min\left(\quad \left\|{}^1\boldsymbol{R}_F{}^2\right\| \quad , \quad \frac{\left\|{}^1\boldsymbol{R}_F{}^2\right\|}{\left\|{}^1\boldsymbol{R}_F{}^1\right\|} \quad \right) \leq \varepsilon_{res}$$

$$min(\quad 393.47 \quad , \quad 0.040 \quad) > 10^{-2}$$

A.4.

Iteration 3

A.4.1.

Element update procedure

$$n_{2_x} = n_{2_x} + \Delta u_7 = 1 - 1.25 \times 10^{-5} = 1$$

$$n_{2_z} = n_{2_z} + \Delta u_9 = -0.0053 - 8.09 \times 10^{-9} = -0.0053$$

$$L_{def} = 1.00$$

$$CosDir = [1.00 \quad 0.00 \quad -0.0053]$$

A.4.2.
Calculate internal forces

A.4.2.1.
Calculate transformation matrices

- **Nodal incremental rotation matrices ($\boldsymbol{R}_{inc}$)**

$$\boldsymbol{R}^3_{inc_1} = \boldsymbol{I}_{3x3}$$

$$\boldsymbol{R}^3_{inc_2} = \begin{bmatrix} 1 & 0 & 8.66 \times 10^{-8} \\ 0 & 1 & 0 \\ -8.66 \times 10^{-8} & 0 & 1 \end{bmatrix} = \boldsymbol{I}_{3x3}$$

- **Nodal rotation matrices ($\boldsymbol{R}_n$)**

$$\boldsymbol{R}^3_{n_1} = \boldsymbol{I}_{3x3}$$

$$\boldsymbol{R}^3_{n_2} = \begin{bmatrix} 1 & 0 & 0.0080 \\ 0 & 1 & 0 \\ -0.0080 & 0 & 1 \end{bmatrix}$$

- **Element rotation matrix**

$$\boldsymbol{R}^3_e = \begin{bmatrix} 1.00 & 0.00 & -0.0053 \\ 0 & 1 & 0 \\ 0.0053 & 0.00 & 1.00 \end{bmatrix}$$

A.4.2.2.
Calculate nodal relative rotations

$$\Delta\theta_1 = [0.00 \quad -0.0053 \quad 0]$$

$$\Delta\theta_2 = [0.00 \quad 0.0027 \quad 0]$$

A.4.2.3.
Calculate vector of relative displacements ($\boldsymbol{d}_r$)

$$L_{inc} = L_{def} - L = 1.70 \times 10^{-6} \approx 0$$

$$\boldsymbol{u}^3_r = [0 \quad 0 \quad 0 \quad 0 \quad -0.0053 \quad 0 \quad 0 \quad 0 \quad 0 \quad 0 \quad 0.0027 \quad 0]^T$$

A.4.2.4.

Calculate internal forces

$$\boldsymbol{f}_{int}^{3} = \boldsymbol{K}_{L}^{(m)}\,\boldsymbol{u}_{r}^{3}$$

$$\boldsymbol{f}_{int}^{3} = [-53.3373 \quad 0 \quad 9999.9 \quad 0 \quad -10000 \quad 0 \quad 53.337 \quad 0 \quad -9999.9 \quad 0 \quad 0.1252 \quad 0]^{T}$$

$$\boldsymbol{f}_{G}^{3} = [-0.0040 \quad 0 \quad 10000 \quad 0 \quad -10000 \quad 0 \quad 0.0040 \quad 0 \quad -10000 \quad 0 \quad 0.1252 \quad 0]^{T}$$

$$\boldsymbol{F}_{int}^{3} = \boldsymbol{f}_{G}^{3}$$

A.4.3.

Calculate tangent stiffness matrix

$$K_{t}^{3}(1:6) = \begin{bmatrix} 3.1416\times10^{7} & 0 & 0 & 0 & 10000.0 & 0 \\ & 7.5001\times10^{6} & 0 & -10000.0 & 0 & 3.75\times10^{6} \\ & & 7.5001\times10^{6} & 0 & -3.75\times10^{6} & 0 \\ & & & 4.81\times10^{5} & 0 & 1666.6 \\ & & & & 2.5\times10^{6} & 0 \\ & & & & & 2.5\times10^{6} \end{bmatrix}$$

$$K_t^3(7:12) = \begin{bmatrix} -3.1415\times10^{7} & 0 & 0 & 0 & -10000.0 & 0 \\ 0 & -7.5001\times10^{6} & 0 & 10000.0 & 0 & 3.75\times10^{6} \\ 0 & 0 & -7.5001\times10^{6} & 0 & -3.75\times10^{6} & 0 \\ 0 & 10000.0 & 0 & -4.81\times10^{5} & 0 & -1666.6 \\ -10000.0 & 0 & 3.75\times10^{6} & 0 & 1.25\times10^{6} & 0 \\ 0 & -3.75\times10^{6} & 0 & -1666.6 & 0 & 1.25\times10^{6} \\ 3.1416\times10^{7} & 0 & 0 & 0 & 10000.0 & 0 \\ & 7.5001\times10^{6} & 0 & -10000.0 & 0 & -3.75\times10^{6} \\ & & 7.5001\times10^{6} & 0 & 3.75\times10^{6} & 0 \\ & & & 4.81\times10^{5} & 0 & 1666.6 \\ & & & & 2.5\times10^{6} & 0 \\ & & & & & 2.5\times10^{6} \end{bmatrix}$$

A.4.4.

Calculate vector of residual forces and solve linear system

$$\boldsymbol{R}_F^3 = [0.0040 \quad 0 \quad -10000 \quad 0 \quad 10000 \quad 0 \quad -0.0040 \quad 0 \quad -1.54\times10^{-5} \quad 0 \quad -0.1252 \quad 0]$$

$$\boldsymbol{K}_t^3 \Delta\boldsymbol{u}^3 = \boldsymbol{R}_F^3$$

$$\boldsymbol{\Delta u}^3 = [0 \quad 0 \quad 0 \quad 0 \quad 0 \quad 0 \quad 0 \quad 0 \quad 0 \quad 0 \quad 0 \quad 0]^T$$

A.4.5.

Calculate convergence criterions

$$min\left(\quad \|{}^1\boldsymbol{\Delta u}^1\| \quad , \quad \frac{\|{}^1\boldsymbol{\Delta u}^1\|}{\|{}^1\boldsymbol{\Delta U}^1\|} \quad \right) \leq \varepsilon_{disp}$$

$$min(\quad 2.24\times10^{-7} \quad , \quad 2.33\times10^{-5} \quad) < 10^{-4}$$

$$min\left(\quad \left\|{}^1\boldsymbol{R}_F{}^3\right\| \quad , \quad \frac{\left\|{}^1\boldsymbol{R}_F{}^3\right\|}{\left\|{}^1\boldsymbol{R}_F{}^1\right\|} \quad \right) \leq \varepsilon_{res}$$

$$min(\quad 0.125 \quad , \quad 1.25\times10^{-5} \quad) < 10^{-2}$$